

*Adsorbate and thermally induced spin
reorientation transition in thin Fe films on
Cu(100)*

*A dissertation submitted to the
SWISS FEDERAL INSTITUTE OF TECHNOLOGY
LAUSANNE*

*for the degree of
Docteur ès Sciences*

*presented by
Dietrich Peterka
Diplom-Physiker, Universität Hannover, Germany*

*examining board:
Prof. K. Kern, directeur de thèse
Prof. W. Benoit, rapporteur
Prof. B. Hillebrands, rapporteur
Prof. D. Pescia, rapporteur*

*Lausanne, EPFL
2002*

Version abrégée

Dans ce travail de thèse la transition magnétique de réorientation du spin est étudiée pour des couches minces épitaxiales de fer d'épaisseurs croissantes déposées sur Cu(100), à 120 K et température ambiante. L'objectif principal de ce travail est de discuter l'origine de l'anisotropie magnétique perpendiculaire de film de fer d'une épaisseur de moins de 4 MC, qui est controversée depuis longtemps. La sensibilité de la magnétisation et l'influence dominante de l'interface film-vide pour le magnétisme ont été déterminés. Pour la première fois la réorientation de l'axe de magnétisation pendant le processus d'absorption de différents gaz sur Fe/Cu(100) a pu être observée. De même la dépendance en température de la transition de spin a été analysée entre 120 et 300 K pour un film déposé à basse température. Les résultats de ce travail soulignent un équilibre subtil entre la structure et les propriétés magnétiques du film ainsi que l'importance de l'anisotropie de la surface.

La mesure de l'effet magneto-optic Kerr a été faite grâce aux techniques MOKE et le microscope Kerr pour caractériser les propriétés magnétiques des couches minces. Les changements structuraux de la morphologie du film ont été étudiés avec le microscope à effet tunnel. Les modifications effectuées sur ce microscope permettent de l'utiliser comme un microscope à force magnétique (MFM) en remplaçant in-situ la pointe du STM par un cantilever piezorésistif recouvert de cobalt. De cette manière on peut obtenir des informations supplémentaires sur les propriétés magnétiques du film.

La première partie de cette thèse met l'accent sur une description détaillée d'un nouveau système qui a été construit pour des analyses structurales et magnétiques des films minces ferromagnétiques. Ces films ont été déposés in-situ dans une nouvelle chambre de type MBE à des températures variables. Pour les études structurales ou magnétiques un nouveau mécanisme de changement de pointe a été inventé. Celui ci permet de fixer les pointes STM ou MFM à la tête du microscope de type "beetle". Le dispositif MOKE et le microscope Kerr, qui a été adapté spécialement aux mesures in-situ, sont décrits en détail.

Les capacités du microscope Kerr et du microscope à force magnétique ont été testées sur un whisker de fer. Les informations complémentaires sur la structure des domaines sont obtenues en comparant les images Kerr et MFM. De plus, la migration des parois de domaines magnétiques sous l'influence du champ produit par la pointe MFM est observée avec les deux techniques. On a montré dans ce travail que la combinaison de ces deux techniques (Kerr et MFM) est très performante de par la complémentarité de l'information obtenue.

On a trouvé, pour les couches minces de fer déposées à basse température, une magnétisation perpendiculaire au-dessous de 4.3 MC. L'adsorption de seulement 1.4 L d'oxygène cause une réorientation complète de l'axe facile dans le plan du film. Les mesures obtenues par MOKE ont montrées que l'oxyde de fer ne se forme pas. Au contraire le changement, induit par l'adsorbat pendant l'adsorption du monoxyde de carbone, dépend de l'épaisseur de fer. L'exposition du fer au CO cause un décalage d'épaisseur critique de 0.7 MC à 3.6 MC, à laquelle la transition de réorientation a lieu. Les films avec une épaisseur inférieure à 3.6 MC restent magnétisés perpendiculairement. Ces changements induits par les adsorbats sont interprétés grâce à un modèle phénoménologique sous l'hypothèse d'une anisotropie magnétique de surface modifiée. La constante d'anisotropie de surface a pu être déterminée quantitativement à $K_{f-s} = 0.63 \text{ mJ/m}^2$ pour le système CO/Fe/Cu(100).

Le recuit du film de fer à une température de 300 K produit aussi un changement de l'épaisseur critique (t_{crit}). Alors que le chauffage au-dessous de 240 K augmente t_{crit} , le chauffage au-dessus de 240 K diminue t_{crit} . Les expériences ont permis de séparer les changements réversibles et irréversibles de l'épaisseur critique. Les changements réversibles sont attribués à la dépendance de la constante d'anisotropie avec la température. Tandis que les changements irréversibles sont probablement dus aux changements structuraux du film thermiquement induit.

Les changements des propriétés magnétiques dus aux processus thermiquement activés, ont été étudiés ultérieurement sur des films de fer avec une magnétisation perpendiculaire à différentes températures. Le volume de Barkhausen, déduit des mesures de viscosité magnétique, augmente linéairement avec les températures. On a trouvé que le retournement de la magnétisation est dominé par le mouvement des parois de domaines pour les champs de pré-magnétisation, lesquels sont plus grands que le champ coercitif mais plus petit que le champ de saturation.

Abstract

In this thesis the spin reorientation transition in wedge-shaped epitaxial Fe films on Cu(100) substrates grown at 120 K and/or room temperature is investigated. The major objective of the work is to contribute to the long-standing controversy about the origin of the perpendicular anisotropy of Fe films thinner than four monolayers. The dominating influence of the film-vacuum interface on the magnetism was deduced from the sensitivity of the magnetization to adsorbate coverage. For the first time the reorientation of the easy axis of magnetization during the adsorption process of different gases on Fe/Cu(100) could be imaged. Also the temperature dependence of the spin reorientation transition of low temperature (LT) grown Fe was investigated in a temperature range between 120 K and 300 K. The results of the work underline the delicate balance between film structure and the magnetic properties of the film as well as the importance of the surface anisotropy contribution.

Integral and laterally resolved magneto-optical Kerr effect measurements – MOKE and Kerr microscopy have been used to characterize the magnetism of the films. Structural changes of the film morphology have been studied with scanning tunneling microscopy (STM). The design of the microscope used also allowed the operation as a magnetic force microscope (MFM) by replacing the STM tip in-situ by a piezoresistive cantilever coated with cobalt. Thus, additional information about the film magnetism could be obtained.

The first part of the thesis gives a detailed description of the newly developed system designed for structural and magnetic analysis of MBE-grown ferromagnetic thin films in-situ and at variable temperatures. A new in-situ tip exchange mechanism has been developed to attach STM tips or MFM tips to the beetle type microscope head, for structural or magnetic investigations, respectively. The MOKE setup and the Kerr microscope, which was particularly adapted for in-situ investigations, are described in detail.

The capacity of the Kerr microscope and the magnetic force microscope is tested on an iron whisker. Complementary information about the domain structure are obtained comparing Kerr and MFM images. Further, the migration of a magnetic domain wall under the influence of the MFM tip stray field is observed with both techniques. It is shown that this combination of the two in-situ imaging techniques is very powerful due to the complementary information they provide.

For low temperature grown iron films out-of-plane magnetization was found for thicknesses below 4.3 ML. The adsorption of only 1.4 L oxygen causes a complete reorientation of the easy axis into the film plane. The formation of Fe oxides could be excluded by MOKE data. In contrast the adsorbate induced changes during carbon monoxide adsorption are dependent on the Fe thickness. The exposure of the Fe to CO causes a shift of the critical thickness, at which the reorientation transition occurs, by 0.7 ML down to 3.6 ML. Films thinner than 3.6 ML remain magnetized perpendicularly. These adsorbate induced changes are interpreted in a phenomenological model assuming a modified magnetic surface anisotropy. The surface anisotropy constant can be quantitatively determined to $K_{f-s} = 0.63 \text{ mJ/m}^2$ for the system CO/Fe/Cu(100).

Annealing of the Fe film up to 300 K also causes a change of the critical thickness (t_{crit}). While annealing below 240 K increases t_{crit} , further annealing above 240 K decreases t_{crit} . The experiment allowed to separate reversible and irreversible changes of the critical thickness. Reversible changes are attributed to the temperature dependence of the anisotropy constants. Irreversible changes are most likely due to thermally induced structural changes of the film.

The change of the magnetic properties due to thermally activated processes has further been studied in Fe films with perpendicular anisotropy at different temperatures. The Barkhausen volume is derived from measurements of the magnetic after-effect and is found to increase linearly with temperature. The magnetization reversal was found to be governed by domain-wall motion for pre-magnetization fields larger than coercivity but smaller than the saturation fields.

Contents

Version abrégée	i
Abstract	iii
1 Introduction	1
2 Experimental	5
2.1 UHV system	5
2.2 The variable temperature MFM/STM	9
2.3 Magneto-optical measurement methods	21
3 Complementary magnetic imaging with Kerr/MFM	35
3.1 Domain imaging on an iron whisker	35
3.2 Domain wall displacement in epitaxial Fe films	37
4 Magnetic reorientation transition in ultrathin films	41
4.1 Energy contributions to the magnetic anisotropy	41
4.2 Structural and magnetic properties of Fe/Cu(100)	46
4.3 Adsorbate influences on the magnetic properties	54
5 Adsorbate induced spin reorientation	59
5.1 Oxygen induced spin reorientation in Fe/Cu(100)	59
5.2 Fe thickness selective reorientation during CO adsorption	67
5.3 Adsorption experiments with NO	68
6 Temperature-dependent magnetic properties of Fe/Cu(100)	75
6.1 Thermally induced spin reorientation	75
6.2 Magnetic after-effect and the Barkhausen volume	81
Conclusions and outlook	89

Bibliography	93
Abbreviations and common symbols	103
Acknowledgements	105
Curriculum vitae	107
Publications	109

Chapter 1

Introduction

Epitaxial thin ferromagnetic films show striking deviations from their respective bulk behavior in their structural as well as magnetic properties. Many experiments show that ultrathin films have a modified magnetic anisotropy [1, 2], enhanced magnetic moments [3, 4], a reduced Curie temperature [5], altered magneto-elastic coupling [6, 7] or critical exponents [5]. Also the dominating influence of the interfaces with decreasing film thickness determines the magnetic [8] and the magneto-electric transport properties [9, 10]. In many examples the sensitive correlation between the magnetic properties and the film structure as well as surface [11] or interface roughness [12, 13] was demonstrated. Patterned micro- and nanostructures show a dependence of their magnetism, in particular their domain configuration, on their size and shape [14, 15]. Novel magnetic properties arise from further reducing the dimensionality of the structures, as was shown on monoatomic cobalt chains [16].

Often the magnetism of epitaxial thin films is investigated in-situ by measuring the magnetization dependent magneto-optical Kerr effect (MOKE) [17]. This technique yields an integral information about the film magnetism over a small volume and hides details of the domain state of the sample. In the past, conclusions about the domain configuration have been drawn from interpreting the MOKE signal. For a detailed understanding of the magnetic state of the sample and the magnetization process though, domain imaging is indispensable [18]. Among several imaging techniques for thin film magnetism, the scanning electron microscopy with spin analysis (SEMPA) [19, 20], Kerr microscopy [21], and magnetic force microscopy (MFM) [22, 23] are of particular interest due to their high performance. SEMPA offers the advantage of a wide imaging range of a scanning electron microscope for magnetic domain imaging, from millimeters down to several nanometers. This advantage is opposed by the enormous technical effort required

for SEMPA experiments. In contrast, Kerr microscopy and magnetic force microscopy can routinely and cheaply be used for magnetic studies. Though, the scan range of these techniques is limited. Furthermore, the quantitative interpretation of the MFM signal is a non-trivial matter and also the influence of the tip stray field may lead to a perturbation of the sample or to different contrast images [24]. Therefore, in order to expand the imaging range for magnetic investigations and to obtain complementary information about the magnetic structure, the parallel application of magneto-optical Kerr microscopy and magnetic force microscopy in one single UHV chamber is desired. Only a few approaches have been made in the past to apply one or the other technique in UHV systems. For instance, a combined scanning tunneling microscope (STM) and a MFM have been used for in-situ investigation of epitaxial Co films on Au(111) [25]. On the other hand, an in-situ Kerr microscope has been employed to image epitaxial Fe on W(110) [26, 27].

In-situ domain imaging in ultrathin films is of basic interest for the study of their unique magnetic properties. Furthermore, the correlation of the magnetism and the film structure is the key for tailoring particular magnetic properties in thin films or nanostructures. Therefore, in this work a new UHV system combining Kerr microscopy, magnetic force microscopy and scanning tunneling microscopy for in-situ analysis of epitaxial films at variable temperatures was set up. A beetle type microscope head [28] was equipped with a novel in-situ tip exchange mechanism which allows to attach STM or AFM tips as well as MFM tips to the scan piezo, for structural or magnetic analysis of the films, respectively. This unique combination allowed structural and magnetic imaging on the same film in-situ. The design of the system allowed to investigate the same area on the sample surface by both magnetic imaging techniques. Thus, further investigation of some features in the magnetic structure seen by the Kerr microscope can be done with the enhanced resolution of the MFM. The scan range of the MFM of several micrometer overlaps with the imaging range of the Kerr microscope, thus allowing to compare both magnetic imaging methods directly and to combine the complementary information of both techniques. Also, an extended imaging range from millimeter down to submicrometer range was thus achieved.

The capability of this system of in-situ domain imaging at variable temperatures is exploited to study the spin reorientation transition in Fe films on Cu(100). Epitaxial Fe on Cu(100) substrates is of particular interest due to the appearance of different structural and magnetic phases depending on the film thickness. Below a critical film

thickness perpendicular magnetization is found experimentally [29,30]. The presence of perpendicular magnetization was firstly ascribed to magneto-volume effects due to the tetragonally expanded lattice of the Fe film [31]. Later, ab-initio calculations showed the importance of the modified electronic structure at the film-substrate interface for the anisotropy [32]. Recent experiments point out the sensitivity of the magnetism to cover layers and suggest the film-vacuum interface to be the driving force for the perpendicular anisotropy [33,34]. Despite the amount of work done on this system open questions concerning the origin of the magnetic transitions still remain.

The goal of this thesis is to clarify the origin of the spin reorientation transition in Fe/Cu(100) grown at low temperatures. For this purpose the response of the film anisotropy to gas adsorption and annealing was studied by in-situ Kerr microscopy and by the magneto-optical Kerr effect. Experiments performed on Fe films of varying thickness by Kerr microscopy allowed to image the adsorbate or thermally induced shift of the critical thickness for the reorientation transition directly during the experiment. Thus, the particular importance of the film-vacuum interface for the magnetism in the films is recognized. The results are discussed within a phenomenological model proposing the surface anisotropy as the origin of the perpendicular magnetization.

Chapter 2 of the thesis describes the experimental setup. Both magnetic imaging techniques, the MFM and the Kerr microscope and their operation modes are described. The design of the a novel in-situ tip exchange mechanism is depicted, which allows to operate the microscope alternatively as STM or MFM.

In Chap. 3 the imaging of specific magnetic structures by Kerr microscope and MFM is demonstrated. The imaging of the same sample area in the flux closure domain pattern of a Fe whisker, and the as-grown domain state of in-situ grown Fe films with both techniques yielding complementary magnetic information is shown.

In Chap. 4 the main contributions to the magnetic anisotropy energy are summarized. The spin reorientation in thin films at a critical thickness is discussed as a result of competing anisotropy energies. This model will be used later in this work to describe adsorbate and thermally induced changes of the spin reorientation transition in low temperature grown Fe films, as observed in the experiments. Also, recent experiments and results on Fe/Cu(100) and adsorbate induced effects are reviewed in this chapter.

In Chap. 5 the experiments on adsorbate induced changes of the magnetic properties of LT and RT grown Fe films on Cu(100) are explained. The influence of the adsorbates

O₂, CO, NO and H₂ on the spin reorientation transition is studied by Kerr microscopy on wedge-shaped Fe films. Adsorbate induced changes are monitored directly during the experiment for the first time on this system.

Also thermally induced shifts of the reorientation transition are observed during the annealing of the films. These experiments are discussed in Chap. 6. Temperature dependent reversible and thermally activated irreversible contributions to the magnetic anisotropy are determined experimentally. The results are compared with structural information obtained by variable temperature STM during annealing. From the time dependent magnetization reversal process in a constant magnetic field the Barkhausen volume is derived.

Chapter 2

Experimental

The advantage of in-situ investigations of the magnetic properties of molecular beam epitaxy (MBE) grown, ultrathin films is that no capping layer is required to protect the film. Such a capping layer, as needed for ex-situ investigations (to protect the film), usually alters the magnetic properties considerably. The correlation between film structure and magnetic properties of uncovered MBE grown film is crucial for a detailed understanding of the ferromagnetic behavior. To ensure well defined conditions for the investigation of atomically thin films on single crystal substrates, the interfering influence of adsorbate atoms or molecules have to be reduced to a minimum. This can be done by performing the experiments under ultra-high vacuum (UHV) conditions at pressures $< 10^{-10}$ mbar. Only a few approaches have been done to combine structural and magnetic imaging techniques in a single UHV system and to apply them to in-situ grown ultrathin films [27,35–38]. To get a deeper understanding about the correlation of the structure and the magnetic properties of ultrathin films, a UHV system combining Kerr microscopy, magnetic force microscopy and scanning tunneling microscopy was constructed in this work. The system allows working at variable temperature in the range between 80 K and 500 K. This setup will be described in the following chapter.

2.1 UHV system

The purpose of the designed chamber is to combine Kerr microscopy and magnetic force microscopy. Both techniques supply complementary information about the film magnetism in overlapping lateral imaging ranges, in which magnetic structures can be observed.

For structural investigations the apparatus designed is equipped with a STM. The specially new designed tip exchange mechanism allows to operate this microscope alter-

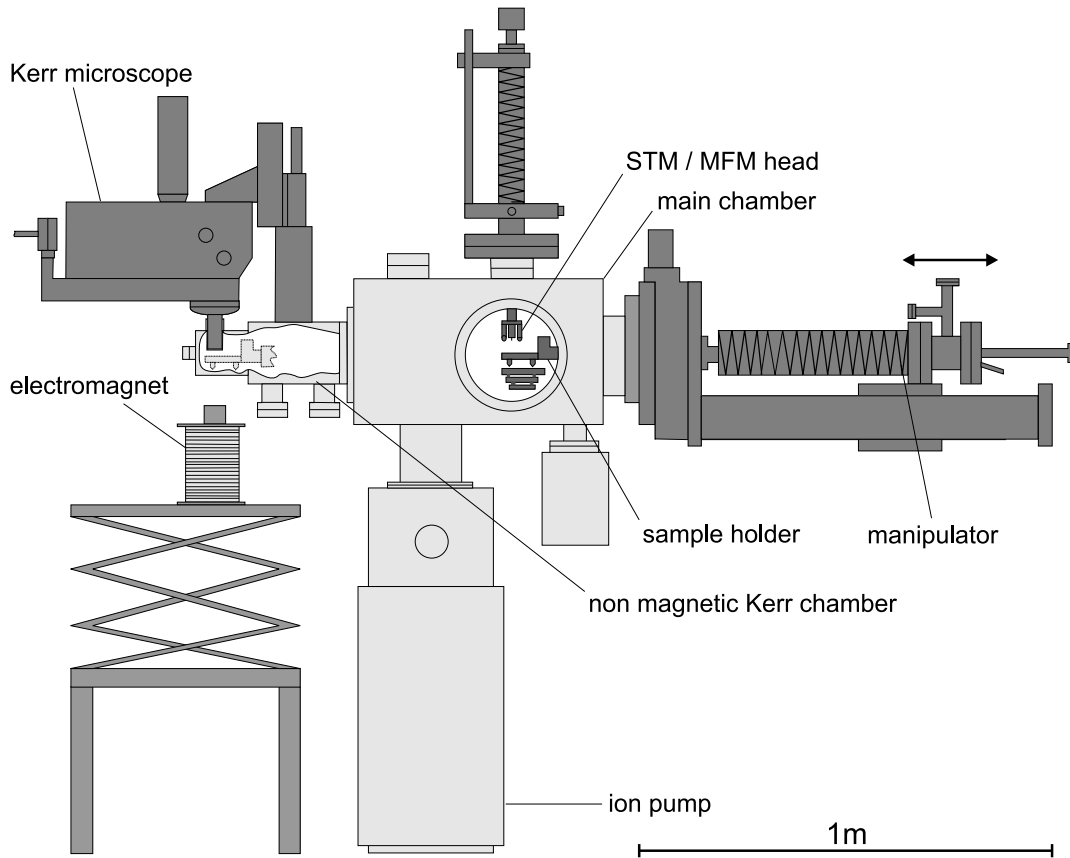


Figure 2.1: Drawing of the UHV system. Instead of the Kerr microscope a MOKE setup can be adapted to the Kerr flange.

natively as an atomic force microscope (AFM) using piezoresistive cantilevers. Both microscopes are described in detail in Sect. 2.2 and Sect. 2.3.

A schema of the chamber is shown in Fig. 2.1. The UHV system consists of a main preparation chamber and a smaller non-magnetic chamber for magnetic investigations. The system is driven by a turbo pump, a titan sublimation pump and an ion pump. A base pressure of $< 9 \cdot 10^{-11}$ mbar can thus be obtained. The sample can be moved by a manipulator with a travel range of 600 mm. The sample holder is mounted on the front end of the manipulator.

The STM/MFM is incorporated into the UHV chamber on a vertical manipulator, which moves the microscope along the main axis and rotates them around the manipulator z -axis. The MOKE and the Kerr microscope are mounted from the atmospheric side to the non-magnetic flange of the chamber. The incoming and outgoing polarized light detects the sample through a strain-free window, which is welded into a non-magnetic Kerr flange. Magnetic fields can be applied from the atmospheric side in direction of the sample surface and perpendicular to it. The setup of these single components

will be described in detail in Sect. 2.3. The adapted load-lock (not shown in Fig. 2.1) allows tip exchange of the STM or MFM without breaking the vacuum. Further the chamber is equipped with several gas inlets. Oxygen, hydrogen and CO gas were used for the adsorption experiments and argon served as ion sputtering gas. All gases are obtainable in gas bottles which are simple to replace. After each bottle mounting the pipeline is flushed several times until the mass spectrometer shows only a negligible amount of residual gas. For dosing the more reactive NO gas, only tubes and gas inlets made of stainless steel are used. As an addition to the standard analysis tools two metal evaporators heated by electron bombardment are implemented for iron and copper evaporation.

Experiments were carried out at a base pressure of $1 \cdot 10^{-10}$ mbar. During all measurements the whole chamber are decoupled from the frame and suspended by springs mounted on the ceiling. The spring constant are chosen to damp the system against low frequency vibrations.

The horizontal manipulator (1) with the mounted sample holder positions the sample in front of the preparation and analysis tools. The design of the sample holder is shown in Fig. 2.2. The support plate (2), which is fixed on the end of the manipulator, carries the base plate (3) with sample holder (4) and the sample (5). During the STM/MFM measurements the manipulator arm is lowered until the base plate with sample holder and sample rest on the viton damped stack (6). The sample holder with sample is

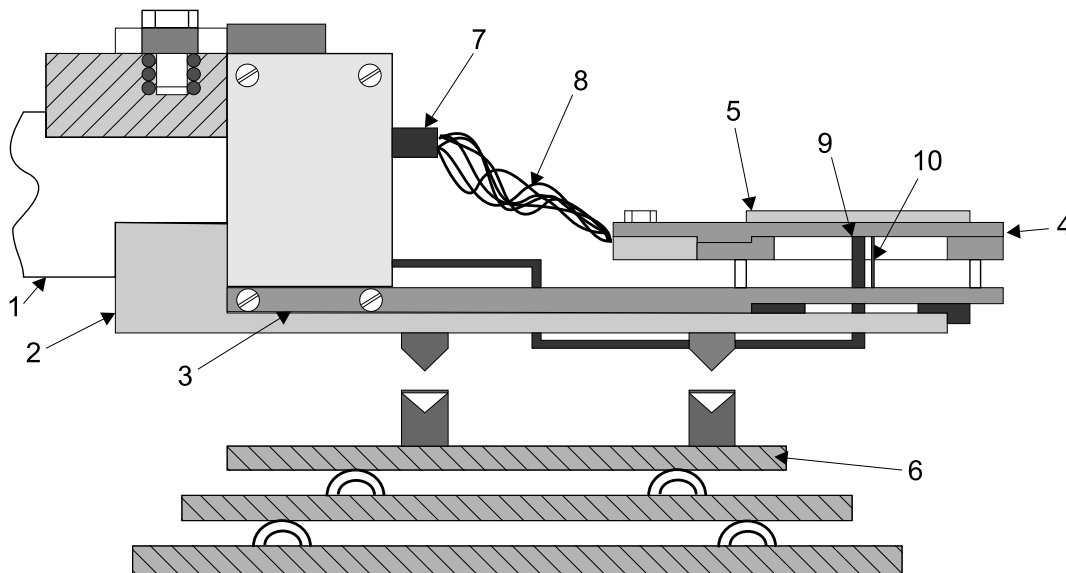


Figure 2.2: Side view of the sample manipulator made of non-magnetic materials. (1) manipulator arm, (2) support plate, (3) base plate, (4) sample holder, (5) sample, (6) viton damped stack (7) cryostat, (8) copper braid, (9) filament wire, (10) thermocouple.

then decoupled from any external vibrations of the manipulator. Only the sample itself is thermally coupled to a helium flux cryostat (7) via a copper braid (8). The wire netting provides good cooling and temperatures down to 80 K can be achieved while the transferred vibrations are reduced to a minimum. At the backside of the sample holder a commercial halogen lamp filament (Philips, $P = 20$ W) is mounted (9) to heat the sample either by radiation or by electron bombardment (maximal 1400 K). The temperature is measured by a copper/constantan thermocouple (10) instead of a Ni/NiCr thermocouple to suppress any disturbing external magnetic stray fields close to the sample. Thermal contact is achieved by pressing the thermocouple by means of a small spring to the backside of the hat-like shaped sample. The thermocouple was calibrated in boiling liquid nitrogen outside the chamber.

Sample preparation

Cu(100) single crystals are used as substrates for the growth of ultrathin ferromagnetic films. The crystals were mechanically polished ex-situ by crystal trade MaTeck. The orientational misfit of the crystals is better than 0.2° . The Cu substrates are prepared in-situ by the standard procedure of three subsequent Ar^+ sputter and

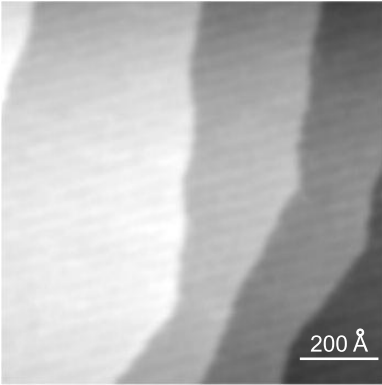


Figure 2.3: STM image of a clean Cu(100) surface. The image size is $1000 \times 1000 \text{ \AA}^2$.

annealing cycles [39,40]. The Ar^+ ions have a kinetic energy of 500 eV and hit the sample under an angle of incidence of 45° . The first and second annealing is done at 840 K, the final annealing only at 650 K. During the last annealing the sample temperature is decreased slowly from 650 K to room temperature (RT) with a rate of approximately 2 K/s. This procedure was found best to maximize the terrace width size and to avoid the formation of Cu clusters on defects. The surface quality was checked by STM (Fig. 2.3).

Fe is deposited by electron beam evaporation from an iron rod with a purity of 99.99%. The pressure during evaporation is kept always below $2 \cdot 10^{-10}$ mbar. The deposition rate of the Fe evaporator as a function of the Fe-ion flux was calibrated by preparing a submonolayer film on the Cu (100) crystal and measuring the actual coverage by STM. The achieved accuracy was exceeded 0.05 atomic layers. The flux rate is kept constant by controlling the high voltage on the target. Hence the film thickness was determined from the flux rate and duration of evaporation. The typical evaporation rate was about 0.4 ML/min.

2.2 The variable temperature MFM/STM

In the first part of this chapter the experimental setup of the magnetic force microscope/scanning tunneling microscope is described. The main part is a new in-situ tip exchange mechanism which allows operating the instrument in both modes by replacing the magnetic MFM cantilever by a tunneling tip. A plug/screw joint mechanism supplies the mechanical stability for the self-excitation of the cantilever oscillation in the non-contact AFM/MFM mode. The delicate coating procedure of the used piezoelectric cantilevers is presented. Finally the operating principles of a magnetic force microscope are discussed.

Microscope setup

The new microscope is designed to work in three different operation modes: MFM and AFM in contact and non-contact mode and STM, at variable temperatures between 80 K and 500 K. The in-situ operation of the MFM and AFM relies on Si_3N_4 piezoresistive cantilevers. The advantage of these levers is the simple tip exchange without severe requirements for mechanical or optical alignment. The microscope head, the tip holder and the sample holder are entirely made of non-ferromagnetic materials to avoid the presence of any stray field in the vicinity of the sample.

A schema of the MFM microscope head and the exchangeable tip holder is shown in Fig. 2.4. The microscope head is based on a beetle type STM originally designed by Besocke [28, 41]. The STM/MFM is supported by three ruby balls (1) which are glued to the ends of the outer piezo legs (2). The latter provide the coarse approach and the coarse lateral motion of the microscope by a slip-stick motion on a triple helical ramp which is mounted around the sample. These outer tube scanners (Staveley Sensors Inc., East Hartford, USA) with the outer dimensions of $0.25 \times 0.02 \times 0.61$ inch are equipped with Ag electrodes instead of commonly used Ni electrodes. The piezos are made of EBL No.1 material which has a low dependence of the piezoelectric coefficients on the temperature range of interest. The scan piezo itself (3) has to be large enough ($0.375 \times 0.03 \times 1.2$ inch) to accommodate the connector for the tip holder. With the scan piezo used, a scan range of $10 \mu\text{m} \times 10 \mu\text{m}$ can be achieved.

In the following we focus on the new design of the in-situ tip exchange mechanism. The mechanical and electrical connection between the scan piezo of the microscope head (Fig. 2.4a) and the tip holder (Fig. 2.4b) was inspired by a common audio stereo jack (chinch connector). The tip holder is equipped with a Ti pin (4) and an outer Ti contact with thread (5). Both contacts are electrically insulated from each other and from the

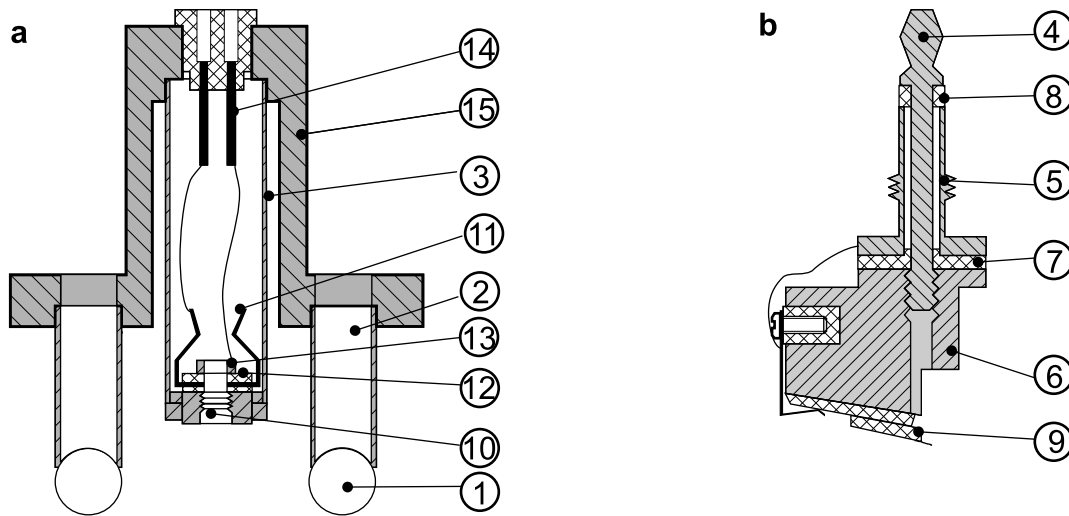


Figure 2.4: **a:** Beetle type microscope head with socket for the tip; **b:** exchangeable tip holder; (1) rubby ball, (2) outer piezo, (3) scan piezo, (4) Ti pin, (5) Ti contact with thread, (6) Ti body, (7, 8, 12) macor spacers, (9) piezo-resistive cantilever with contact pads, (10) female contact with inner thread, (11) spring contact, (13) Ti nut, (14) electrical contact, (15) microscope Ti body.

main Ti body (6) by macor spacers (7, 8). The cartridge containing the piezoresistive cantilever and contact pads for electrical connection is clamped on the bottom of the tip holder (9). It can be replaced by a tunneling tip which is then mounted into an opening on the Ti body. The female counterpart at the bottom end of the scan piezo consists of a Ti contact with inner thread (10) and a spring contact (11) electrically isolated by two macor spacers which have been glued into the end of the scan piezo. Both, the spring and the Ti contact are wired to a socket to allow the output of the electrical signals. Additionally the wire is shielded inside the scan tube by a grounded metal tube to prevent any disturbing crosstalk from the piezo-voltage. The whole instrument is picked up by a suspension tube (I) (Fig. 2.5), which is mounted on the arm of the x, y, z, φ -translator.

The probe stock (III) is attached to a rack and pinion linear manipulator. It can store up to four tip holders and is mounted to a bakeable load-lock. In order to attach the tip holder to the microscope head (II), the tip is positioned under the center of the microscope by the linear manipulator (Fig. 2.5a), then the microscope is lowered to pick up the required tip holder. The accurate positioning of the microscope with respect to the tip holder is done by the x, y, z, φ -translator. After a perfect alignment has been achieved, the tip holder is simply plugged into the opening of the scan piezo by a z -motion, followed by a half turn of the microscope head to tighten the screw mechanism (Fig. 2.5b). Pin (4) and spring contact (11) as well as contacts (5) and (10)

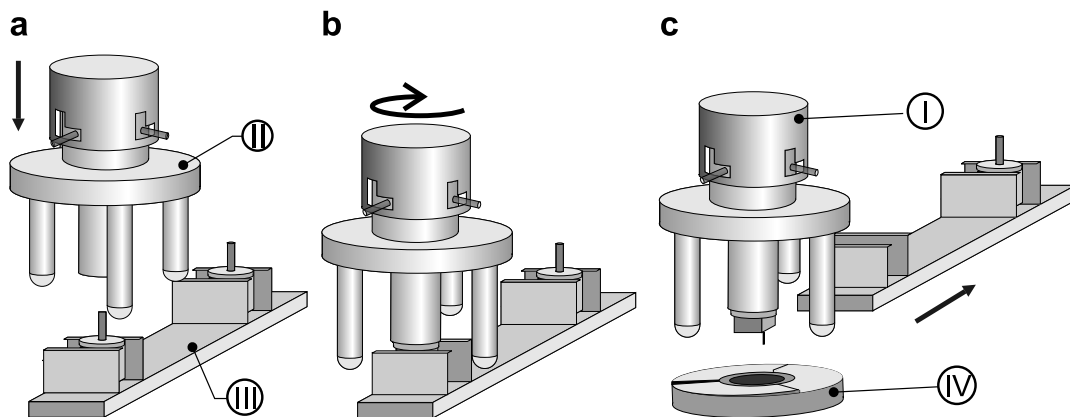


Figure 2.5: Tip exchange process. **a:** The microscope is lowered over the tip holder position and tightened; **b:** via the plug/screw joint. **c:** Remove of the probe stock and positioning of the microscope. (I) suspension, (II) microscope head, (III) probe stock, (IV) sample holder with ramp and sample.

in Fig. 2.4 establish the electrical connection. Now the microscope including the tip is moved upwards and can be positioned on the sample (Fig. 2.5c). The plug/screw joint mechanism provides mechanical stability as is necessary for the self-excitation of the cantilever oscillation in the non-contact AFM/MFM mode. The control electronics is based on a commercial AFM/STM electronic module by Park Scientific Instruments and was adapted to the special needs of the beetle type microscope.

The lateral calibration of the piezoscanner was performed on a grating with a periodicity of $1\ \mu\text{m}$ (Fig. 2.6a). The scan range in x and y direction differs since the time dependent piezo creep leads to a larger motion of the piezo in the slow scan direction. For the calibration of the z-motion, a freshly cleaved KBr single crystal was used. Such a crystal is suitable for the calibration because of its well-defined step height. Terraces can be seen in Fig. 2.6b. The inset shows the line scan across the surface. Different terraces are separated by a monoatomic step height of $3.3\ \text{\AA}$.

Piezoresistive tips and magnetic coating

During the last years a number of techniques have been developed to measure the deflection of a small AFM cantilever. Such deflection arises from the force interaction between tip and sample and is described further down in this chapter. The most widely applied methods for cantilever bending detection in scanning force microscopy (SFM) uses laser beam deflection [42], tunneling junctions [43, 44] and fiber-optic interferometry [45–50]. Despite many successful applications of these techniques the manipulation and alignment under UHV conditions are still non-trivial. The alignment of the op-

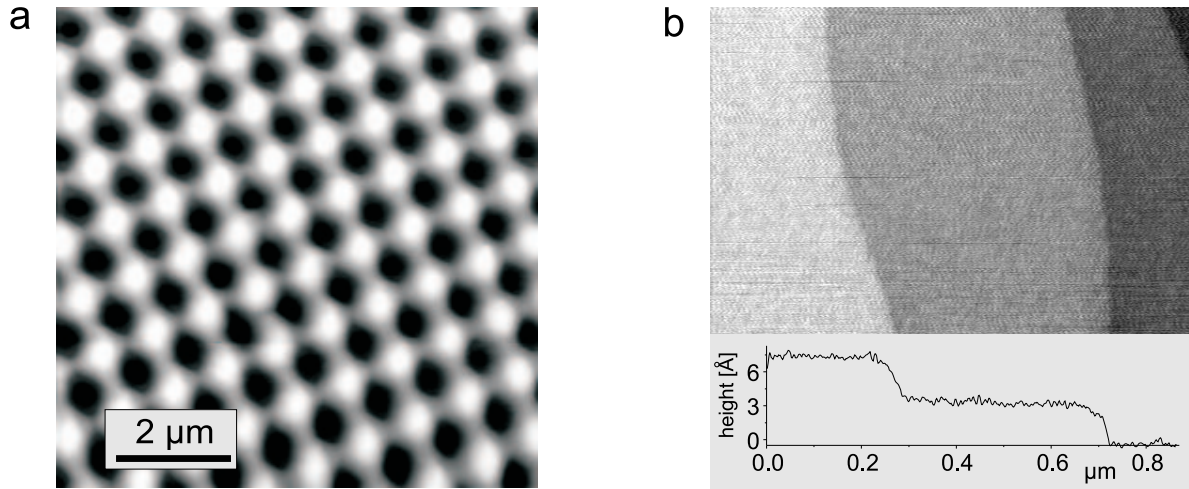


Figure 2.6: **a:** Calibration grating with a periodicity of $1 \mu\text{m}$. **b:** Terraces on KBr crystal, cleaved in air.

tical components outside of the chamber or the placing of the deflection sensor with respect to the cantilever represent most of the difficulties. A quite promising approach to circumvent these restrictions is the use of piezoresistive cantilevers [51, 52]. These force sensors are made of boron doped silicon. An anisotropic etching process forms the conical tip at the end of the cantilever. The piezoresistive effect is due to the change of the bulk resistivity from semiconductor material under stress. Therefore the deflection of the cantilever during scanning over the sample surface results in the change of the cantilever resistivity which can be monitored online with an external Wheatstone bridge [53]. To achieve sensitivity to the magnetic stray field of the sample, the MFM tips are coated with ferromagnetic layers. Depending on the application, the coatings are made of cobalt, nickel, or iron. For some applications hard magnetic tips are desired and are achieved by $\text{Co}_{80}\text{Cr}_{20}$ or $\text{Co}_{80}\text{Ni}_{20}$ alloys.

The piezoresistive tips used in this work are commercially available cantilevers for the Autoprobe VP instrument of the Park Scientific Instruments. The company supplies two types of piezoresistive cantilevers for contact and non-contact AFM, whose characteristics mainly differs in the resonant frequency and force constant. The mechanical properties of the MFM tips used in this work are summarized in Table 2.1. The force

Force constant (N/m)	Resonance frequency (kHz)	Width (μm)	Length (μm)	Thickness (μm)
20	60–240	90	150	3.0–4.5

Table 2.1: Typical mechanical features of a non-contact piezolever.

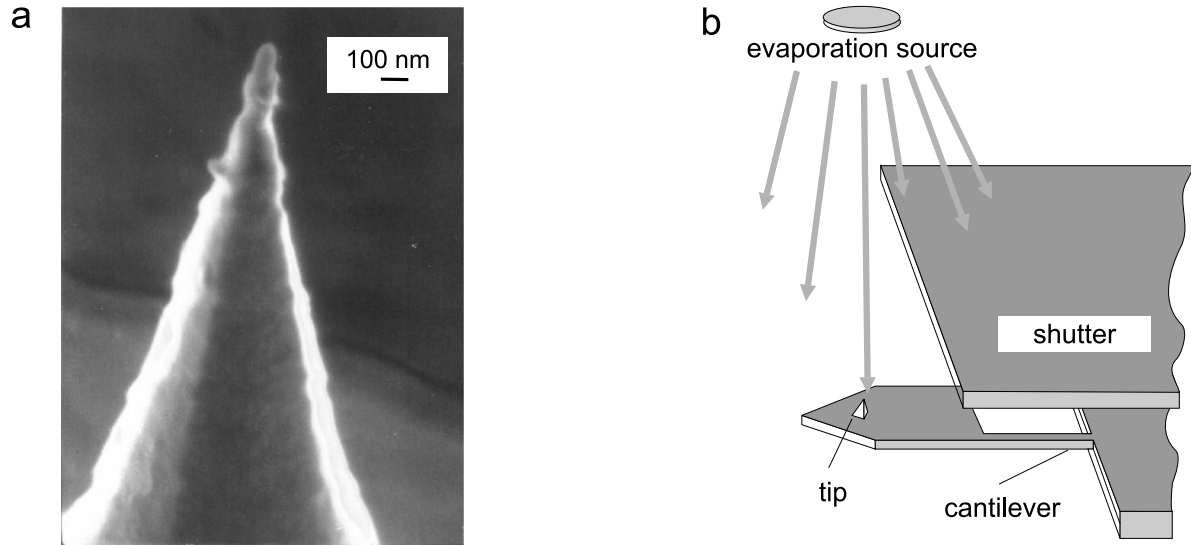


Figure 2.7: **a:** Scanning electron microscope image of piezoresistive cantilever tip; **b:** geometry of the evaporation process.

gradients in MFM/AFM are rather small and require a proper detection of the cantilever. The optimal cantilever has a large resonant frequency combined with a small force constant. Generally, fabricated tips for MFM applications show a force constant from 10^{-2} up to 10^2 N/m and resonant frequencies in the range of 10–500 kHz.

The lateral resolution achievable by MFM mainly depends on the working distance between tip and sample and the specific characteristics of the tip, i.e. the coating and the tip curvature. To receive qualitative information about the tip geometry, several piezoresistive sensors have been investigated by scanning electron microscopy (SEM) (Fig. 2.7a). The average tip radius was found to be smaller than 50 nm. As can be seen in the work, this tip radius mainly limits the lateral resolution in the experiments. In comparison, if piezoresistivity of the tips is not required, silicon tips with a nominal tip radius below 10 nm are commercially available.

The coating of the piezoresistive tips was performed outside the UHV chamber in two different ways. On the one hand a thin Co film was deposited by electron beam evaporation. On the other hand CoCr was deposited by sputtering to obtain a hard magnetic tip. To exploit the resistance of piezoresistive tips, it is extremely important not to alter the resistance by the coating process. This is an unique difference to standard Si tips, where the bending of the cantilever is measured with other methods than the resistance. Only tips evaporated with Co kept the original resistance of 2 k Ω . This is the fundamental requirement for the correct functionality of the Wheatstone bridge. Responsible for the strong deviation of the sputtered tips are the backscattered Co and Cr

ions during the sputtering process. They cause a resistance increase in the doped area of the cantilever. The geometry of the electron beam evaporation process is shown in Fig. 2.7b. The evaporation source is located 20 cm above the tip. The setup allows the parallel coating of four MFM tips. They are glued by double-sided tape on a metal block and are covered to the half by a shutter in a distance of approximately $500 \mu\text{m}$ above the tip. This way, the deposition of coating material onto the piezoresistive cantilever is prevented. The thickness of the Co films on the Si cantilever was varied between 200 \AA and 500 \AA . The highest sensitivity and resolution were achieved at a thickness of 300 \AA . After evaporation of Co, the film was passivated by 50 \AA Au to prevent any oxidation. Table 2.2 shows the most important parameters in the evaporation process.

The evaporation rate can be determined by a microbalance with an accuracy of 20%. Before finally introducing the cantilevers into the UHV chamber via a load-lock, they were magnetized along the tip direction by an external magnetic field of 0.9 T.

	Film thickness (\AA)	Substrate temperature (K)	Evaporation rate ($\text{\AA} / \text{s}$)	Vacuum conditions (mbar)
Co	200–500	300	0.8	$< 2 \cdot 10^{-6}$
Au	50	300	2	$< 1 \cdot 10^{-7}$

Table 2.2: Evaporation parameters of Au and Co.

Forces between tip and surface

Any interaction between tip and sample or any force acting on the tip is detected by the MFM experiment. To distinguish force contributions experimentally, the fact is used that different forces show a different decay rate with increasing distance. Therefore, different forces dominate at certain distances to the surface.

Short range forces: They dominate the region within 1 nm above the surface and usually show a high force derivative. The interatomic coulomb repulsion due to the ionic character of the cores is a short range force. A second force of quantum mechanical origin, the exchange force, might be interesting for magnetic imaging. True atomic resolution is expected in magnetic imaging if its detection becomes possible.

Van der Waals interaction originates from the induced dipole-dipole interaction between probe and sample. This force is always attractive and also present in neutral atoms or molecules without a permanent dipole moment. In general the Van der Waals forces between two atoms are proportional to $1/z^7$. The decay of the interaction force

depends very strong on the shape of the interacting species. With the assumption of a sphere tip and a planar sample surface and integrating over interactions of all dipole moments yields the force, which decays in this case quadratically with the distance [54]:

$$F = -\frac{Ar}{6z^2} \quad (2.1)$$

where r is the tip radius and A the Hamaker constant. In the case of a rectangular bar with the width b , the thickness s and an infinite length, the force is given by

$$F = -\frac{Abs}{6\pi z^3} \quad (2.2)$$

which represent a third power law dependence.

Electrostatic forces: These forces are strong long-range forces which exceed the Van der Waals forces in the range above 10 nm of tip-sample spacing. Electrostatic forces are generated, when a voltage between insulating sample and tip is applied.

Magnetic forces: The detection of the MFM is based on the interaction of a magnetic tip and the emanating stray field of a magnetic sample. The calculation of the sum of magnetic forces acting in z -direction on the tip is given by summarizing all magnetic dipole forces between tip and sample [55]:

$$F(z) = \int_{tip} d^3\vec{r}_1 \int_{sample} d^3\vec{r}_2 f_z(\vec{r}_1 - \vec{r}_2), \quad (2.3)$$

where $f_z(\vec{r})$ is the interaction between two magnetic dipoles, \vec{m}_1 and \vec{m}_2 , at a distance $\vec{r} = \vec{r}_1 - \vec{r}_2$:

$$f_z(\vec{r}) = \frac{\mu_0}{4\pi} \frac{\partial}{\partial z} \left(\frac{3(\vec{r} \cdot \vec{m}_1)(\vec{r} \cdot \vec{m}_2)}{r^5} - \frac{(\vec{m}_1 \cdot \vec{m}_2)}{r^3} \right). \quad (2.4)$$

Integration yields the resulting attractive or repulsive force for parallel and antiparallel magnetic moments pointing in z -direction. The force decays in the fourth power with the distance $F(z) \approx 1/z^4$ and their derivatives F' are proportional to $-1/z^5$.

The tip geometry strongly influences how the sample stray field will be detected. In practice, the tip shape is determined by the tip preparation process. A few theoretical works provide some detailed calculations of forces resulting from some well defined and idealized tip geometries (i.e. pyramidal, conical, cylindrical) and stray field distributions. These predictions could be compared with the experimental data. Some references [56–60] give examples of the calculation of forces or derivatives given and provide analytical formulas or numerical approaches for a known domain structure in the sample.

Operation mode of MFM

In AFM, a microscopic tip positioned at the front end of a flexible cantilever is scanned across the specimen. Any forces acting on the tip, as described in the previous chapter, cause a deflection of the cantilever. The deflection is a function of the acting force. The force or the force gradient are measured during scanning over the sample. The curve in Fig. 2.8 represents the superposition of all forces that act on the cantilever in a surfaces potential which is similar to the Lennard-Jones potential. One distinguishes between contact and non-contact mode of operation. The MFM measurements in this work are done in the non-contact operation mode. Therefore, to understand how MFM senses the magnetic forces or force gradients in the following section a description of this dynamic non-contact mode is given.

The **static mode** is used in the contact AFM. The tip scans in mechanical contact with the sample surface where the repulsive short range forces are dominating (Fig. 2.8). The tip is repelled and the resulting cantilever deflection yields a DC signal accordingly. In contact AFM the cantilever deflection and thereby the applied forces to the cantilever are kept constant. This task is accomplished by the feedback loop. Deviations from a setpoint force are compensated by a scan piezo, which adjusts the distance from the tip to the sample in order to maintain a constant force. The applied voltage to the piezo is used to generate the image.

In the **dynamic mode** the tip is kept some nanometers above the surface, thus the cantilever works in the region where the attractive forces are dominating and the force gradient is positive (Fig. 2.8). Here the microscope mainly senses Van der Waals forces

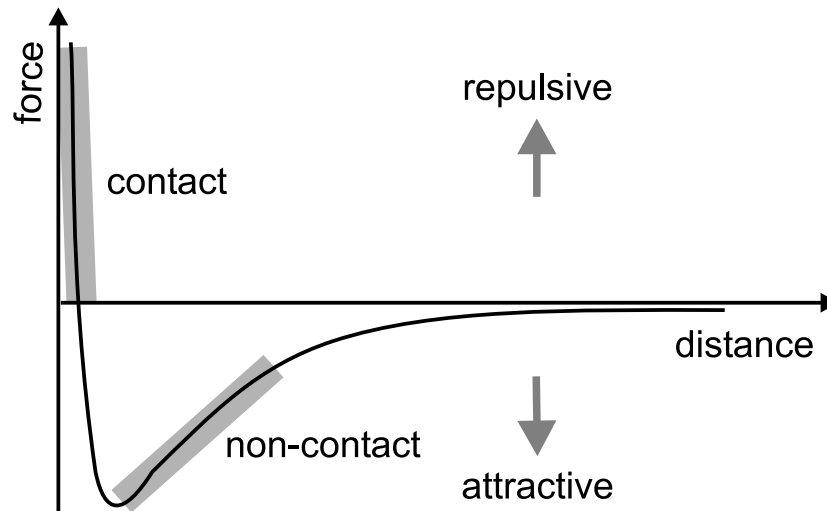


Figure 2.8: Working ranges of non-contact and contact AFM are illustrated in the force-distance curve.

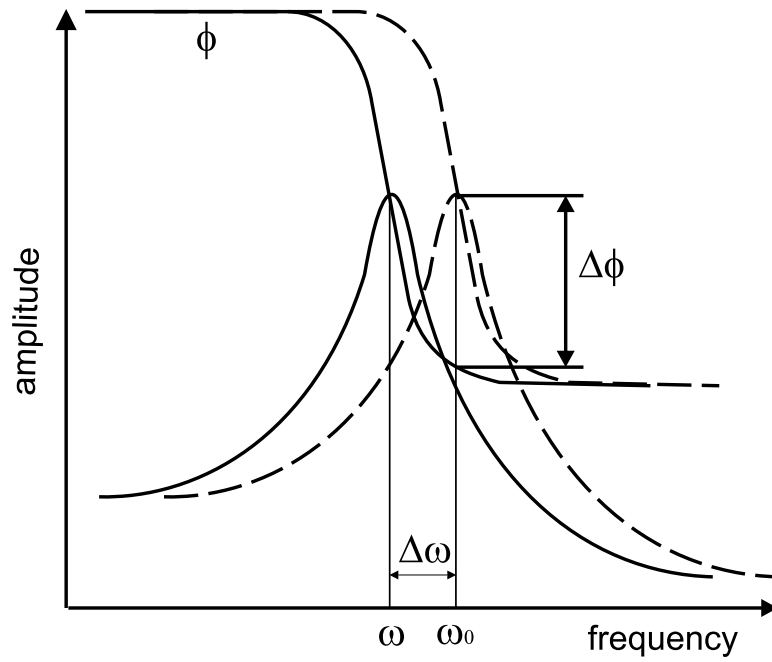


Figure 2.9: Principle of resonance detection in non-contact AFM. The frequency shift $\Delta\omega$ can be indirectly detected as phase shift $\Delta\phi$ (according to [62]).

or other long range forces such as electrostatic and magnetic dipole forces. Since the magnitude of these forces acting on the cantilever is considerably smaller than the interatomic forces detected in contact AFM, a different detection mode is needed. In non-contact AFM the changes of the resonant frequency of an oscillating cantilever are measured, thus providing the needed sensitivity to the long range forces [61]. This dynamic method is in the first approximation sensitive to the force gradient $F' = \frac{\partial F}{\partial z}$, along the z-direction, since in many cases the cantilever is almost parallel to the sample. The presence of a force gradient results in a modification of the effective spring constant (c_{eff}) of the cantilever according to:

$$c_{eff} = c - F' \quad (2.5)$$

where c is the spring constant of the unperturbed cantilever. The change in the effective spring constant results in a shift of the resonance frequency ω_0 to ω of the cantilever:

$$\omega = \left(\frac{c_{eff}}{m}\right)^{1/2} = \left(\frac{c - F'}{m}\right)^{1/2} = \omega_0 \left(1 - \frac{F'}{c}\right)^{1/2} \quad (2.6)$$

where m is the effective mass of the cantilever. F' is small with respect to c , the shift $\Delta\omega$ is

$$\Delta\omega = \omega - \omega_0 \approx -\frac{F'}{2c}. \quad (2.7)$$

This means that the resonance frequency shifts to lower frequencies in the presence of an attractive tip-surface interaction (Fig. 2.9) and to higher frequencies under a repulsive tip-surface interaction.

There are two commonly used detection methods for the shift of the resonance frequency. In the amplitude modulation (AM) technique the cantilever is driven at a constant frequency near the resonance frequency. Changes in the force gradient result in an increase or decrease of the vibration amplitude, which is detected. Secondly in the frequency modulation (FM) technique the amplitude is kept constant and the frequency shift $\Delta\omega$, caused by force gradients, can be measured. In the control unit used in this work, $\Delta\omega$ is converted into phase shift (Fig. 2.9) as will be explained in the following section. This phase shift is then detected.

Feedback technique

In non-contact AFM-mode the z-piezo, driven by the feedback loop, has to fulfill two tasks. Firstly, the cantilever is excited to oscillate. The oscillating frequency is chosen close to the resonance frequency and kept stable by the feedback loop. Secondly, the deviations from the resonance frequency as caused by tip-sample interactions are converted into a phase shift signal which is picked up by the feedback loop to adjust the tip-sample distance. This z-correction signal represents the force gradient on the tip as caused by the sample and is used to generate the image. The resonance frequency is the characteristic feature of each cantilever. It depends on the mass and the spring constant. The tip can be easily excited at this frequency by a bump or by thermal vibrations, since the quality factor of the cantilever oscillation in UHV is usually very high ($Q \approx 10^5$). The block diagram (Fig. 2.10) shows the signal path of the feedback loop. The essential components are the oscillator, responsible for the constant amplitude, and the phase detector which detects the frequency shift.

The cantilever signal is detected and then pre-amplified. The pre-amplified signal is input to both, the oscillator module and the phase detector. In the oscillator module the current amplitude is compared with a reference value. The difference signal is the deviation of the current amplitude from this reference and is multiplied by a gain factor. The resulting, phase shifted signal (amplitude correction signal in Fig. 2.10) is used to excite the piezoscanner in order to stabilize the amplitude at the reference setting. The oscillator does not affect the frequency of the cantilever. The second module, the phase detector contains a tunable bandpass filter and a phase comparator. The incoming signal from the pre-amplifier (the cantilever oscillation signal) passes the filter which is set to the resonance frequency of the cantilever. The characteristic of

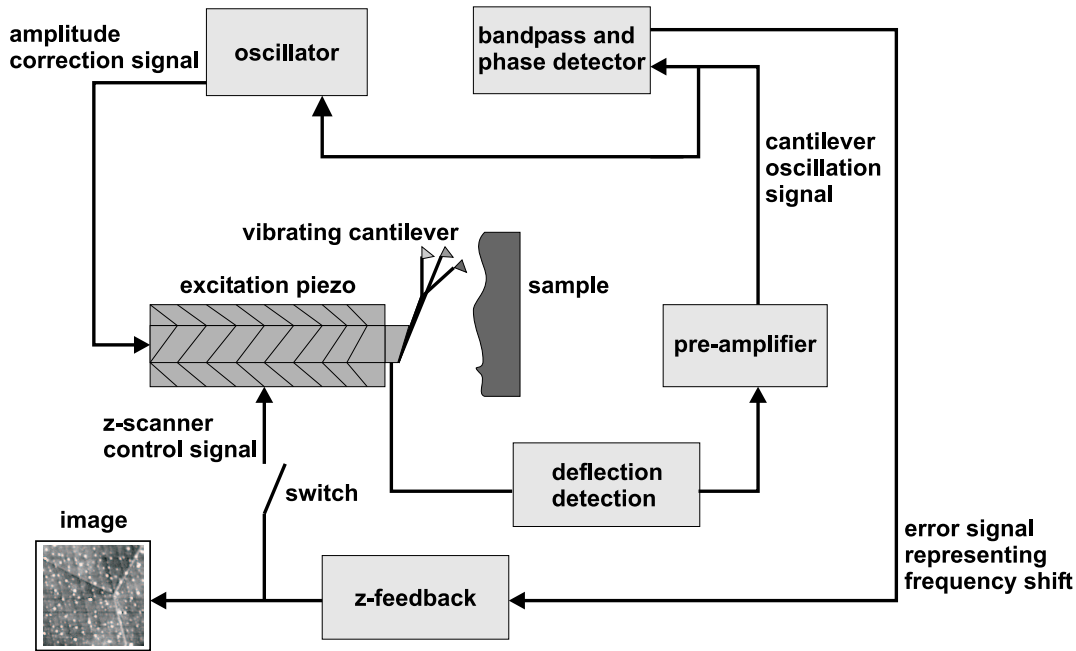


Figure 2.10: z-feedback loop of dynamic non-contact detection.

bandpass is that any deviation of the cantilever oscillation signal (due to changes in the force gradient experienced by the tip) from the resonance frequency produces a phase shift in the output of the bandpass filter [63]. The phase-shifted signal and the original unshifted cantilever signal are passed through the phase comparator which outputs a phase difference $\Delta\phi$ or error signal. The error signal reflects therefore shifts $\Delta\omega$ in the resonance frequency which are equivalent to changes in the force gradient. With the generated error signal a new input signal is produced which drives the z-scanner and adjusts the tip-sample spacing. The resulting image of topography mirrors contours of a constant force gradient.

In MFM the error signal can be fed back to the z-piezoscanner. This mode is called constant signal mode. In contrast, in constant distance mode the feedback loop is opened. Both techniques are compared in Chap. 3 on images obtained on Bloch walls of an iron whisker.

In **constant distance mode** the MFM operates without feedback loop and allows the separation of forces of different origin, i.e. the Van der Waals from electrostatic or magnetic forces. To achieve this the sample has to be scanned from two different heights. Firstly, the tip scans over the sample close to the surface (region of Van der Waals forces) and maps the topography. Secondly, the tip is moved some nanometers away from the surface and follows the stored line profile from the sample surface with

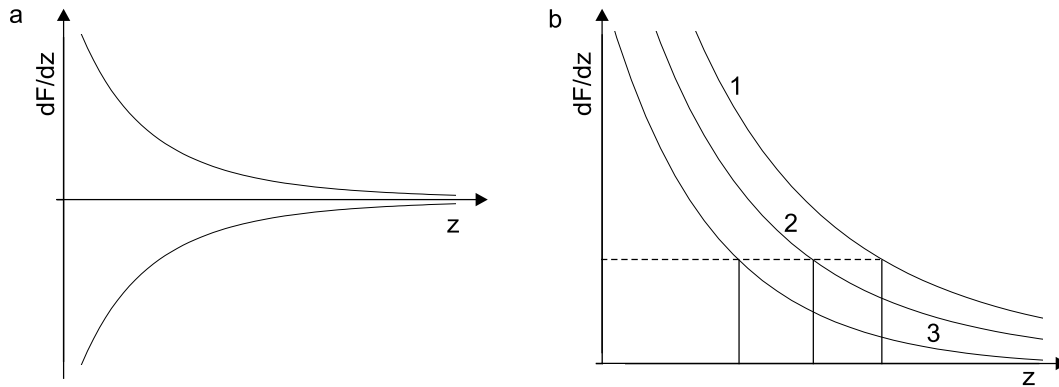


Figure 2.11: Biasing effect to make possible the feedback loop technique in MFM. **a:** Repulsive and attractive magnetic force gradient; **b:** superposition of the force gradient in the left figure by an additional Van der Waals force derivative.

the feedback loop opened. The tip responds to the attractive and repulsive forces of any magnetic domain distribution of the sample. In this way the local stray field of the sample can be measured directly and also quantitatively, if the characteristics of the tip are known. In this work, similar to the technique described above, topographical line scans in x - and y -direction are taken at first, to determine the sample surface slope. The tip then scans in an averaged constant height following this slope while details are neglected.

Constant signal mode: This method is sensitive to the sum of the magnetic and non-magnetic signals. It operates at reduced tip-sample distance, and the active feedback loop controls the z -piezo. The presence of net attractive interaction is necessary for stable working of the feedback loop. Since the magnetic forces can either be attractive or repulsive, an additional offset force has to be applied to convert any force into an attractive force to warrant feedback loop stability. This can either be done by applying a bias voltage of 0–10 V [64], which complies with the task of a positive electrostatic force gradient, or by using the Van der Waals force for this purpose. The sum of the detected force gradients F' in the feedback method can thus be specified as:

$$F' = F'_{V.d.Waals} + F'_{magnetic} + F'_{electrostatic} \quad (2.8)$$

The non-linearity of the MFM response to a magnetic signal results from the non-linear dependence of the biasing force on the increasing distance z . Figure 2.11 demonstrates the role of the attractive Van der Waals force derivative. The idea behind it, is to create a net attractive force by superimposing an attractive force to make the feedback possible. In Fig 2.11a the positive and negative magnetic force gradients from a magnetic

interaction are shown. Figure 2.11b shows the net attractive force gradient resulting from the superposition of the Van der Waals force derivative (2) with the maximum force derivative of the repulsive (3) and attractive (1) magnetic force gradient of Fig. 2.11a. Moving along the horizontally dashed line in Fig. 2.11b, corresponds to the operation in constant force derivative mode.

2.3 Magneto-optical measurement methods

In this work a Kerr microscope and an experiment to measure the Kerr effect (MOKE) was set up to investigate the magnetic properties in-situ. Both measurement methods are based on the magneto-optical Kerr effect. The first part of the chapter is addressed to the understanding and deriving of the MOKE principle. Thereafter, the experimental setup of both techniques is described in detail.

Magneto-optical Kerr effect

The history of magneto-optics is more than 150 years old and starts with Faradays discovery in 1846 of the rotation of the polarization plane when linearly polarized light propagates through a flint glass under an applied magnetic field [65]. The magneto-optics is based on emission, absorption and propagation of light under the influence of magnetic fields. Besides the Faraday effect also the Kerr effect [66,67], the Voigt [68,69] and Cotton-Mouton effect [70] are counted to the magneto-optical phenomena.

All effects describe the change of the polarization and/or ellipticity of light upon interaction with magnetic matter. Both, Faraday and Voigt effect describe the change of polarization/ellipticity of linearly polarized light when passing through a transparent medium. In the Faraday effect, the propagation direction of light is parallel to the external field H . The effect is explained by circular birefringence, i.e. different indices of refraction for the left and the right circularly polarized light, in which the linearly polarized wave can be decomposed. In the first approach the Faraday effect is proportional to the magnetization M . However in the Voigt effect the propagation direction of light is perpendicular to the applied field H . In contrast to the Faraday effect, the Voigt effect depends on M^2 . The Cotton-Mouton effect, which also leads to induced birefringence, is observed in some liquids whose magnetic anisotropic molecules are oriented in a magnetic field.

The Kerr effect, known as magneto-optical Kerr effect, is measured in reflection. Linearly polarized light is reflected on a magnetic surface and as a consequence polarization/ellipticity will change. Depending on the relative orientation of the magnetization

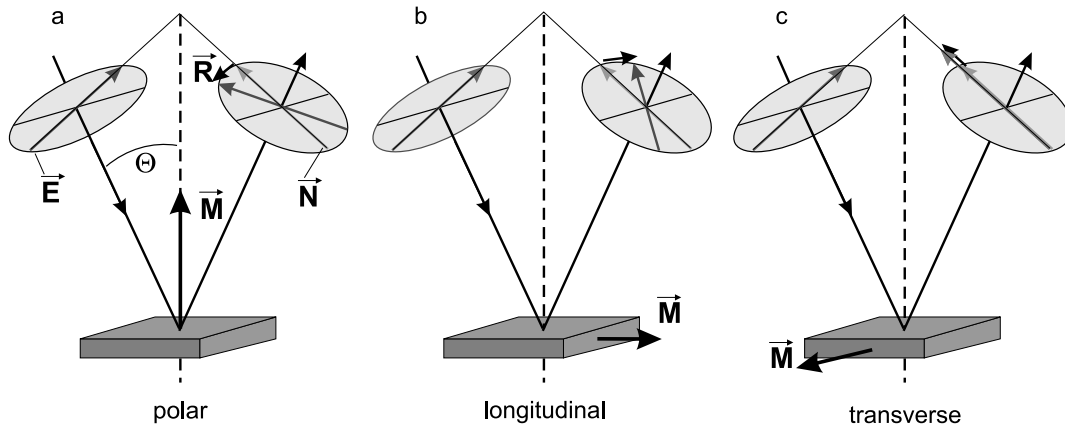


Figure 2.12: The three MOKE geometries. Polar **a**, longitudinal **b** and transverse **c** magneto-optical Kerr effect. \vec{E} denotes the incident polarization vector, \vec{N} the regular component of the reflected light and \vec{R} denotes the perpendicular part of the Kerr amplitude after reflection.

\vec{M} and the electric field vector \vec{E} of the incident light with respect to each other, one distinguishes the polar, longitudinal and transverse Kerr effect. These three possible geometries for MOKE are illustrated in Fig. 2.12.

In the polar Kerr effect, the magnetization \vec{M} is oriented perpendicular (out-of-plane) oriented to the surface plane (Fig. 2.12a). The polar Kerr signal is roughly proportional to the Kerr amplitude $R \approx \cos \Theta$ and shows its maximum at $\Theta = 0$. Θ is the angle between the surface normal and the direction of the incident light. In the longitudinal Kerr geometry the magnetization lies in the sample plane and occurs within the plane of incidence which is created by the incoming and reflected light (Fig. 2.12b). In this case the Kerr amplitude vanishes for $\Theta = 0$ and is proportional to $\sin \Theta$. With the transverse Kerr effect the magnetization lies in the film plane but perpendicular to the plane of incidence. As no light component propagates in direction of the magnetization vector, the reflected light does not change the rotation in the polarization direction. Only changes in the variation of the amplitude, which is also proportional to $\sin \Theta$, are detected.

Phenomenological description of the polar Kerr effect

The interaction of light with matter can be properly described in a theoretical model which includes the quantum mechanical contemplation of the dielectric susceptibility tensor. In this quantum mechanical calculation, the rotation of light polarization follows asymmetries of the absorption and emission for left and right circular polarized light under consideration of the dipole selection rules. However, in practice a phenomenological model which considers the Lorentz force of the excited electrons in the sample

in the presence of a magnetic field turns out to be very useful. In this work MOKE is used to characterize the qualitative behavior of thin Fe films. The present macroscopical approach relates the Kerr ellipticity and the Kerr rotation to the dielectric susceptibility term by Maxwell's equations. Despite the simplified model, the calculation is often useful for experimentalists to describe the observations in the experiments. In polar geometry, the magnetic field $\vec{B}_0 = \vec{H}_0 + \vec{M}$ lies in z-direction and within the plane of incidence. It is convenient to express linear polarized light as a superposition of right circularly polarized (RCP) and left circularly polarized light (LCP), whose wave vectors \vec{k} propagate in z-direction. In the classical theory, the electric susceptibility tensor $\vec{\chi}$ follows from the Lorentz oscillator model and the polarization \vec{P} . Therefore the picture is a system of bound electrons in a harmonic potential with the resonance frequency ω_0 . The electrons are excited to oscillate by the electromagnetic field of the incident light wave ($\vec{E}(\vec{r}, t) = \vec{E}_0 e^{i(\omega t - \vec{k}_0 \cdot \vec{r})}$, $\vec{B}(\vec{r}, t)$). The equation of motion of each electron can be written as:

$$\ddot{\vec{r}} + \gamma \dot{\vec{r}} + \omega_0^2 \vec{r} = \frac{q}{m} \left\{ -\vec{E}(\vec{r}, t) - \frac{\dot{\vec{r}}}{c} \times [\vec{B}_0 + \vec{B}(\vec{r}, t)] \right\} \quad (2.9)$$

where $\gamma \dot{\vec{r}}$ is a phenomenological damping coefficient. Equation (2.9) is a system of differential equations and contains the Lorentz force as the last term. With the formulation $\vec{r} = \vec{r}_0 e^{i\omega t}$ and under the assumption of $\dot{\vec{r}} \ll c$, the force component resulting from $\vec{B}(\vec{r}, t)$ is negligible, and with the assumption of small oscillation amplitudes ($\vec{k}_0 \cdot \vec{r} \approx 0$), then the equation of motion can be solved:

$$-\omega^2 \vec{r} - i\omega \gamma \vec{r} + \omega_0^2 \vec{r} = \frac{q}{m} \left\{ -\vec{E}(\vec{r}, t) - \frac{i\omega \vec{r}}{c} \times \vec{B}_0 \right\}. \quad (2.10)$$

These coupled equations yield for the x- and y-component of \vec{r} and the z-component:

$$r_x = \frac{-q}{m} \frac{-E_x + i\omega r_y B_z}{(\omega_0^2 - \omega^2 + i\omega\gamma)} \quad r_y = \frac{-q}{m} \frac{-E_y + i\omega r_x B_z}{(\omega_0^2 - \omega^2 + i\omega\gamma)} \quad r_z = \frac{-q}{m} \frac{-E_z}{(\omega_0^2 - \omega^2 + i\omega\gamma)}. \quad (2.11)$$

The deviation of the electrons from their equilibrium position induces a dipole moment \vec{p} , which is in first approximation proportional to the product of the electron charge q and the elongation \vec{r} . Now the polarization \vec{P} is defined as the number N of dipole moments per volume unit V :

$$\vec{P} = \vec{p}N/V = q\vec{r}N/V. \quad (2.12)$$

Further the amplitude of the dipole moment is a linear function of the electric field and couples over the electric susceptibility tensor $\vec{\chi}$ [71]:

$$\frac{q\vec{r}N}{V} = \vec{\chi}\vec{E} \quad \text{with} \quad \vec{\chi} = \varepsilon_0(\vec{\epsilon} - \mathbf{1}) \quad (2.13)$$

With Eq.(2.11) and Eq.(2.13) one obtains the components of this tensor:

$$\chi_{xx} = \chi_{yy} = \frac{\rho q^2}{m} \frac{\omega_0^2 - \omega^2 + i\omega\gamma}{(\omega_0^2 - \omega^2 + i\omega\gamma)^2 - 4\omega^2\omega_L^2} \quad (2.14)$$

$$\chi_{xy} = -\chi_{yx} = \frac{\rho q^2}{m} \frac{2i\omega\omega_L}{(\omega_0^2 - \omega^2 + i\omega\gamma)^2 - 4\omega^2\omega_L^2} \quad (2.15)$$

$$\chi_{zz} = \frac{\rho q^2}{m} \frac{1}{(\omega_0^2 - \omega^2 + i\omega\gamma)} \quad (2.16)$$

where $\omega_L = -\frac{qB_0}{2mc}$ is the Lamor precession frequency, ρ the electron density and γ proportional to a resistivity. Considering an isotropic medium or a medium with cubic symmetry, the tensor $\vec{\chi}$ has the following form:

$$\vec{\chi} = \begin{pmatrix} \chi_{xx} & \chi_{xy} & 0 \\ -\chi_{xy} & \chi_{yy} & 0 \\ 0 & 0 & \chi_{zz} \end{pmatrix} \quad (2.17)$$

The free electron limit is obtained by allowing $\omega_0 \rightarrow 0$. In absence of the magnetic field, the off-diagonal elements vanish and χ is just a scalar. In presence of \vec{H} , Eq.(2.15) represents the dependence of the off-diagonal elements from the electric susceptibility tensor to the magnetization $\vec{B}_0 = \vec{H}_0 + \vec{M}$. The direct proportionality to \vec{M} cannot be explained with the classical theory and requires quantum mechanical consideration with respect to the spin-orbit coupling, which will not be shown here.

In the next step it will be explained that different refraction indices for LCP and RCP exist, by following a simple formalism. Starting from Maxwell's equations

$$\vec{\nabla} \times \vec{E} = -\frac{\partial \vec{B}}{\partial t} \quad (2.18)$$

$$\vec{\nabla} \times \vec{B} = \mu_0 \frac{\partial \vec{D}}{\partial t} = \vec{\epsilon}\mu_0 \frac{\partial \vec{E}}{\partial t}, \quad \vec{D} = \vec{\epsilon}\vec{E} = (1 + \vec{\chi})\epsilon_0\vec{E}, \quad (2.19)$$

and the plane wave approximation for the light $\vec{E} = \vec{E}_0 e^{i(\omega t - kz)}$ and $\vec{B} = \vec{B}_0 e^{i(\omega t - kz)}$, the operators take the form $\vec{\nabla} \rightarrow -i\vec{k}$ and $\frac{\partial}{\partial t} \rightarrow i\omega$.

Now taking the curl of Eq.(2.18) and using Eq.(2.19) we obtain:

$$-i\vec{k} \times (-i\vec{k} \times \vec{E}) = \mu_o \vec{c} \omega^2 \vec{E}_0. \quad (2.20)$$

By replacing $\epsilon_0 \mu_0$ by $1/c^2$, $\vec{k} = (1 + \vec{\chi})$ and by the use of $\omega/c = k_0$ and the identity of the vector product $\vec{a} \times (\vec{b} \times \vec{c}) = (\vec{a} \cdot \vec{c}) \cdot \vec{b} - (\vec{a} \cdot \vec{b}) \cdot \vec{c}$ follows:

$$(n^2 \mathbf{1} - \vec{k} \vec{k} / k_0^2 - \vec{\kappa}) \vec{E}_0 = 0, \quad (2.21)$$

where n is the index of refraction given by $n = \vec{k}/k_0$. The system of Eq.(2.21) possesses a non-trivial solution for \vec{E}_0 , if the determinant of the coefficients vanishes. The complex solutions are RCP (marked +) and LCP (marked -) waves:

$$n_+^2 = 1 + (\chi_{xx} + i\chi_{xy}) \quad n_-^2 = 1 + (\chi_{xx} - i\chi_{xy}) \quad (2.22)$$

The difference of the refraction index ($n_+ - n_-$)

$$n_+ - n_- = \frac{i\chi_{xy}}{n_a} \quad (2.23)$$

is proportional to χ_{xy} . The average refraction index $n_a = \frac{n_+ + n_-}{2}$ is almost equal to the refraction index without magnetization $n_0 \approx (\chi_{xx})^{\frac{1}{2}}$, because $|\chi_{xy}| \ll |\chi_{xx}|$.

Finally, the reflection coefficients are calculated to quantify the polar MOKE effect. Resulting from the continuity conditions on a surface of a medium for the incident $\vec{E}_{inc} = \vec{E}_0 e^{i(\omega t - k_0 z)}$, reflected $\vec{E}_{refl} = \vec{E}_1 e^{i(\omega t - k_0 z)}$ and refracted wave $\vec{E}_{refr} = \vec{E}_2 e^{i(\omega t - kz)}$:

$$\vec{E}_0 + \vec{E}_1 = \vec{E}_2, \quad k_0 E_0 + k_0 E_1 = k E_2 \quad (2.24)$$

follows the reflection amplitude r :

$$r = \frac{E_1}{E_0} = -\frac{n-1}{n+1} = |r| e^{i\Phi}. \quad (2.25)$$

In case of incident linear polarized light, which can be resolved into circular polarized components with equal amplitudes, the reflected light will be elliptically polarized, because the reflection coefficients r_+ and r_- differ in phase and magnitude. The Kerr rotation is the rotation of the major axis of the ellipse by the angle

$$\Theta_K = \frac{1}{2}(\Phi_+ - \Phi_-). \quad (2.26)$$

The factor $1/2$ is the result of the decomposition in RCP and LCP. Using Eq.(2.25) the Kerr rotation θ_k and the Kerr ellipticity ϵ_k are obtained:

$$\Theta_k = -\Im \left\{ \frac{n_+ - n_-}{n_+ n_- - 1} \right\} \quad \epsilon_k = -\Re \left\{ \frac{n_+ - n_-}{n_+ n_- - 1} \right\}. \quad (2.27)$$

The proportionality Θ_k to the off-diagonal element of χ_{xy} of the susceptibility and therefore to the magnetization \vec{B}_0 can be seen from Eq.(2.23).

MOKE apparatus

An experiment to measure the magneto-optical Kerr effect was built up to investigate the magnetic properties of atomically thin layers on Cu(100). The MOKE setup mainly consists of three components: a light source to illuminate the sample, an electromagnet to apply a magnetic field to the sample and a light detector to measure the reflected intensity of light. In dependence of the Kerr effect which will be measured respectively, the electromagnet in this experiment can be turned around the sample. Alternatively, two Helmholtz like coils can be used. The light source and the detector are mounted on an optical table. This setup allows easy variation of the angle between incident and reflected light beam and therefore the adaptation to the experiment.

The incident light is linearly polarized by passing a prism. Thereafter the light hits the sample surface and is reflected on it. The reflected light beam passes now a second prism whose crystallographic axis is turned to 90° with respect to the first prism. Now only light passes the prism whose polarization direction deviates from the direction of the incident light and can be recorded by the detector. Figure 2.13 sketches the optical path close to the sample, as for Kerr microscopy and MOKE measurement. The extinction ratio determines the sensitivity of the MOKE setup. It is given by the ratio of the light intensities in the case of crossed (90°) and parallel (0°) polarizers with respect to each other.

Basically the Kerr microscope is sufficient to characterize the magnetic state of the sample. This technique contains the full magnetic information about the surface magnetism of a sample, but laterally resolved. In order to obtain a hysteresis curve of a domain picture one can either project the reflected light rays of the microscope with lenses to a photo diode or analyze the digitally obtained image from the CCD camera by integrating its gray scales to a personal computer (Fig. 2.17). The advantage of the MOKE setup is its easy handling and the increased sensitivity as compared to the Kerr microscope. The incident angle can be varied in a range between 0° and 15° , and is limited by the design of the UHV windows. A laser diode serves as light source ($\lambda = 670 \text{ nm}$, $P = 5 \text{ mW}$; chassis: Newport model 700c), temperature stabilized by a peltier element. With two control units (Newport temperature controller model 325; Newport laser diode driver model 505) the operating temperature is stable within 0.1% and the power of the laser diode deviates maximal by 0.02% from its setpoint. Because of the high stability of the laser diode a lock-in-technique is unnecessary.

The light of the laser diode is focused by a lens which is mounted directly in front of the laser diode. A spot of approximately 0.2 mm^2 on the surface plane is achieved. The entire optical system can be adjusted for s-polarized or p-polarized light respectively. In

One of the unwanted side effects is the Faraday effect which occurs when light travels through the window, which is exposed to the external magnetic field, also called window effect. The Faraday effect appears as linear function of H , superimposed on the Kerr signal. The data can easily be normalized afterwards by removing this linear magneto-optical effect.

The Kerr microscope

The Kerr chamber was specially designed for MOKE and high resolution Kerr measurements. For magneto-optical Kerr microscopy at variable temperatures, several requirements have to be fulfilled. A compact and rigid construction is necessary to avoid mechanical vibrations and thermal drift during the cooling or heating of the sample. Some problems are specially related to the in-situ magneto-optical Kerr microscopy. Samples used for ex-situ studies (in air) are often covered with a dielectric antireflection coating to enhance the contrast [72, 73]. In comparison, unprotected thin film samples for UHV applications show very weak Kerr images, caused by the very low thickness of the magnetic layer and the disturbing, regularly reflected light from the sample surface. Special windows have to be used to reduce the loss of sensitivity due to depolarizing effects by the window.

Only three UHV-Kerr microscopes have been developed and published in literature during the last years [26, 27, 38]. Giergiel et al. [26] and Mentz et al. [38] illuminate the sample with a mercury lamp and use long distance microscopes (Questar) to overcome the big working distance [74]. A somewhat different approach was made by Vaterlaus et al. [27], where a laser diode was used to image the magnetic domains. In this case the focused laser beam scans the sample by moving the sample laterally.

The Kerr instrument presented in our work is based on a modified commercially available polarization microscope (JENAPOL polarizing microscope; Carl Zeiss Jena). To achieve a high optical resolution, we adopted a setup suggested by Hubert [75].

The illumination source, the polarizer and analyzer mounts and the support have been adapted to fit the needs of the Kerr microscope and to keep the versatility of the UHV system. The base, the sample stage and the transmission illumination module have been removed while the microscope, equipped with a Nikon microscope mount (Nikon GmbH, Modular focusing Unit MBD64000) has been attached to a solid tripod directly to the UHV chamber. This type of setup combines ease of adjustment and easy removal of the microscope for the bake out of the chamber.

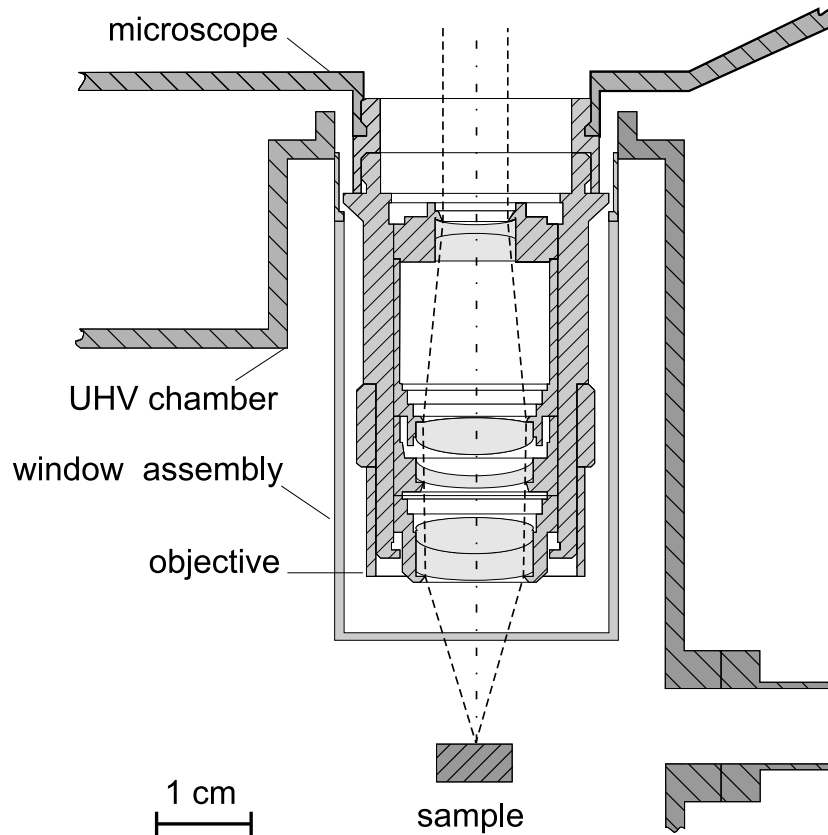


Figure 2.14: The design of the UHV window for Kerr microscopy allows for objective-sample distances of 2 mm.

Figure 2.14 shows a schematic drawing of the light path through the objective lens and illustrates the realization of the short working distance between the objective on the atmospheric side and the sample in ultrahigh vacuum. A strain-free window (Bomco Inc, Gloucester, MA) with a molybdenum-quartz seal is welded into the stainless steel adapter of the Kerr flange. The UHV window and the microscope objective project into the chamber close to the sample. This particular window design allows to operate at a minimum sample-lens distance and to use microscope objectives with a working distance as short as 2.0 mm. An antireflective coating with an effacement efficiency of 99% was deposited on the flat bottom of the window to reduce the glare due to the backscattered light from the window itself. Additionally, the inner side of the Kerr chamber is deposited with absorbent coating of graphite, to suppress stray light.

Proper illumination plays an important role as is needed to achieve high quality images specially for weak magneto-optical Kerr contrast microscopy. A 1 W Ar ion laser ($\lambda = 514 \text{ nm}$) was used as a light source. Advantages of laser illumination in comparison to high pressure mercury lamps are the high intensity and the stable output power [76].

The laser light is coupled into a 30 m long quartz-quartz multimode fiber (MMF) with a diameter of $200\ \mu\text{m}$ and a numerical aperture (NA) of 0.20. The output of this fibre provides a monochromatic, stabilized, high intensity light source of small size and easy handling, ideally suited for Kerr microscopy. Because of the small size of the light source, no aperture stop is needed.

Disadvantages of this setup are a slight degradation of the image quality, due to interference and refraction artifacts, and in particular strong speckle patterns in the image, due to the highly coherent nature of the laser light and the mode propagation in the MMF. Different methods of dithering the MMF to overcome this problem are successfully demonstrated by Argyle et al. [77]. The authors combined simultaneously three methods of dithering the mottle and suppressed with that nonhomogeneities in the illumination pattern. During the first procedure the mode excitations in a MMF are scrambled by a rapidly spinning glass disk having a randomly undulated surface. Secondly, the MMF is agitated mechanically. And finally, a spinning glass disk wedge provides an improvement in the homogeneity. We found that, a satisfactory result could already be obtained by agitating several meters of the MMF. To achieve this we have attached several fibre loops to a commercial bass audio speaker with the membrane cut out to minimize acoustic noise. The speaker is driven close to the loop's eigenfrequencies (in the order of some 10 Hz to 100 Hz) by a frequency generator. In this way, after optimizing the vibration amplitude and the frequency, a very homogenous illumination is achieved.

For illumination adjustment, the tip of the MMF can be displaced by micropositioning screws in all spatial directions of the microscope. To attain uniformly illuminated high quality Kerr images of the specimen with homogeneous extinction across the entire field of view, well-adjusted reflection Köhler illumination is necessary. This is achieved by adjusting the MMF tip position along the optical axis of the microscope. Adjustment of internal lenses, as needed with Kerr microscopes using a slit aperture diaphragm [78], is not needed. The position of the image of the light guide in the objective back focal plane, and by this way the angle and direction of incidence of the light onto the surface, can be adjusted by displacing the MMF tip perpendicular to the optical axis. The Kerr observation mode can thus easily be changed between longitudinal, transverse and polar geometry. The optical path adjusted in Köhler illumination is described in the following section.

Optical path

The illuminating light path and the image forming light path are shown schematically in Fig. 2.15 to visualize the principle of Köhler illumination in the built microscope. Due to the dimensions of the MMF tip, the assumption is made that the image of the light guide acts as a point source. The emitted light from the optical fiber passes in oblique angle the collector lens which focuses the image onto the plane of the aperture diaphragm. In contrast to other spatially distended illumination sources, where the opening and closing of the diaphragm controls the angle of emerging light and thus the numerical aperture, here this effect is negligible due to the small image size in the plane of the diaphragm. Only the aperture of the objective determines the numerical aperture of the microscope.

The second lens in the optical path creates parallel light which passes through the field aperture and the polarizer. This field aperture is responsible for the light cone diameter and therefore restricts the field of view. It also eliminates to some extent unwanted reflected light from oblique angles. It does not affect the optical resolution or the intensity of illumination. At next the linearly polarized light is focused by the tube lens onto the back focal plane of the objective, on its way passing a Berek prism. Our microscope setup allows the replacement of the prism by a beam splitter which permits

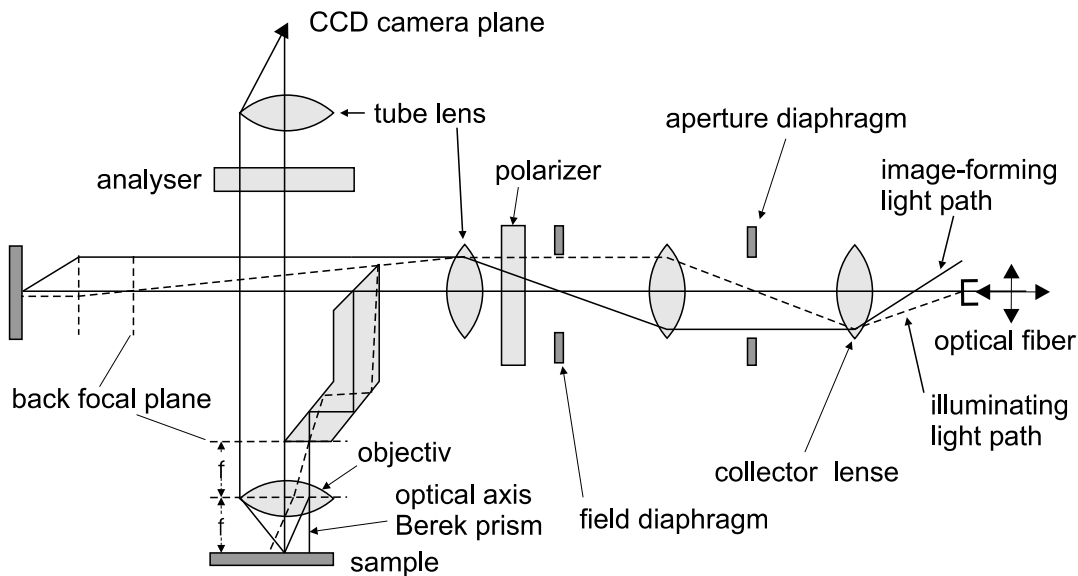


Figure 2.15: Köhler illumination light path used in the Kerr microscope. Emitting light from the optical fiber is directed through the collector lens and then focused onto the back focal plane of the objective. Parallel light illuminates the sample with a uniform lightness. The angle and path of incidence of light on the sample is adjusted by positioning the MMF tip perpendicular to the optical axis.

full perpendicular incidence in polar Kerr geometry. Focussing on the back focal plane creates a parallel light beam emerging from the objective to the sample (illuminating path ray). The reflected light from the sample passes again the objective and proceeds as parallel light ray through the analyzer, before the image is focused by the tube lens onto the CCD camera (image-forming path ray).

For troubleshooting of unwanted side effects like dust or fiber, mapped in the sharp focus, the presence of conjugated planes is very helpful. Conjugated planes mark areas with a common focus. An object that is in focus at one plane is also in focus at other conjugated planes of the optical path. These conjugated planes are the light source, the aperture diaphragm and the back focal plane of the objective for the path of the illuminating light ray and the field diaphragm, the sample plane and the camera plane for the image-forming light path, respectively. When artifacts occur in the sharp focus, then they must originate from near the surface of the imaging-forming part of the conjugated planes. Thus they can be identified and eliminated.

Glan-Thompson prism polarizers were attached to the polarizer and analyzer mounts because they give a better extinction ratio than the standard sheet polarizers. The maximum possible extinction ratio was smaller than $< 2 \cdot 10^{-5}$. The frequently used long-distance objective lens (Planapochromat Carl Zeiss Jena) has a magnification of 16x and a NA of 0.2. Its working distance of 17 mm is corrected for a cover glass of



Figure 2.16: Optical grid with a spacing of $2 \mu\text{m}$ between two grid lines. Slightly reduced resolution in one direction is visible.

the same thickness as the UHV window. Numerical aperture and working distance allow an angle of incidence of about 15° for longitudinal and transverse geometry. The theoretical possible optical resolution d of an optical microscope under the assumption of incoherent light is given by the Rayleigh equation:

$$d = \frac{1.22\lambda}{2n \cdot \sin \Theta}, \quad (2.28)$$

where $n \sin \Theta$ is the numerical aperture and λ the wavelength of the light. In this case, with $\lambda = 514 \text{ nm}$ and the $\text{NA} = 0.20$, the lateral resolution

can be calculated to $d = 1.56 \mu\text{m}$. Figure 2.16 shows the experimental resolution taken on a line grid. The spacing between two black lines is $2 \mu\text{m}$.

Taken the given resolution d , after which two adjacent particles can be distinguished separately, the experimental resolution is determined better than $2 \mu\text{m}$. This is in good agreement with the theoretical value. A somewhat reduced resolution ability can be

found in horizontal direction in the picture. The reason for this is the shape of the light bundle in the sample plane. The bundle is slightly reduced in one direction and has an elliptical shape, which causes a reduction of the numerical aperture along one in-plane axis.

The microscope setup is mounted rigidly on the extension flange to avoid any mechanical vibration of the setup. The arrangement of the external magnet is identical to Fig. 2.13. The images (640×509 pixel) were recorded by a computer controlled CCD camera. The image quality can be greatly improved by background subtraction, image accumulation and averaging with a real-time digital image processor (Hamamatsu Argus 20). Image sequences can be taken with a repetition rate of 5 s/image.

Hysteresis curve from Kerr image

All hysteresis curves obtained in this work were measured with the MOKE setup as described before in Sect. 2.3. However, hysteresis loops can also be obtained by the Kerr microscope as will be demonstrated in the following passage. The spot size of the laser diode in the MOKE apparatus covers approximately the same area as the illuminated field of view of the Kerr microscope, which is 0.12 mm^2 . The MOKE photo diode integrates the reflected polarized light. Any lateral information within the light beam is lost. This information particularly is exploited by the Kerr microscope. The hysteresis loop is obtained by integrating of the grey level of each Kerr image, taken during a full field sweep, individually, and plotting the result versus the field. The calculated hysteresis curve and the corresponding Kerr images of 3 ML Fe film are seen in Fig. 2.17. The film was grown and imaged at 130 K and has a magnetization oriented perpendicular to the surface plane. Figure 2.17a shows the calculated hysteresis curve. With increase of the external magnetic field the domains parallel to the field (dark areas) grow at the expense to the domains with opposite out-of-plane magnetization (bright areas) (Fig. 2.17b to d).

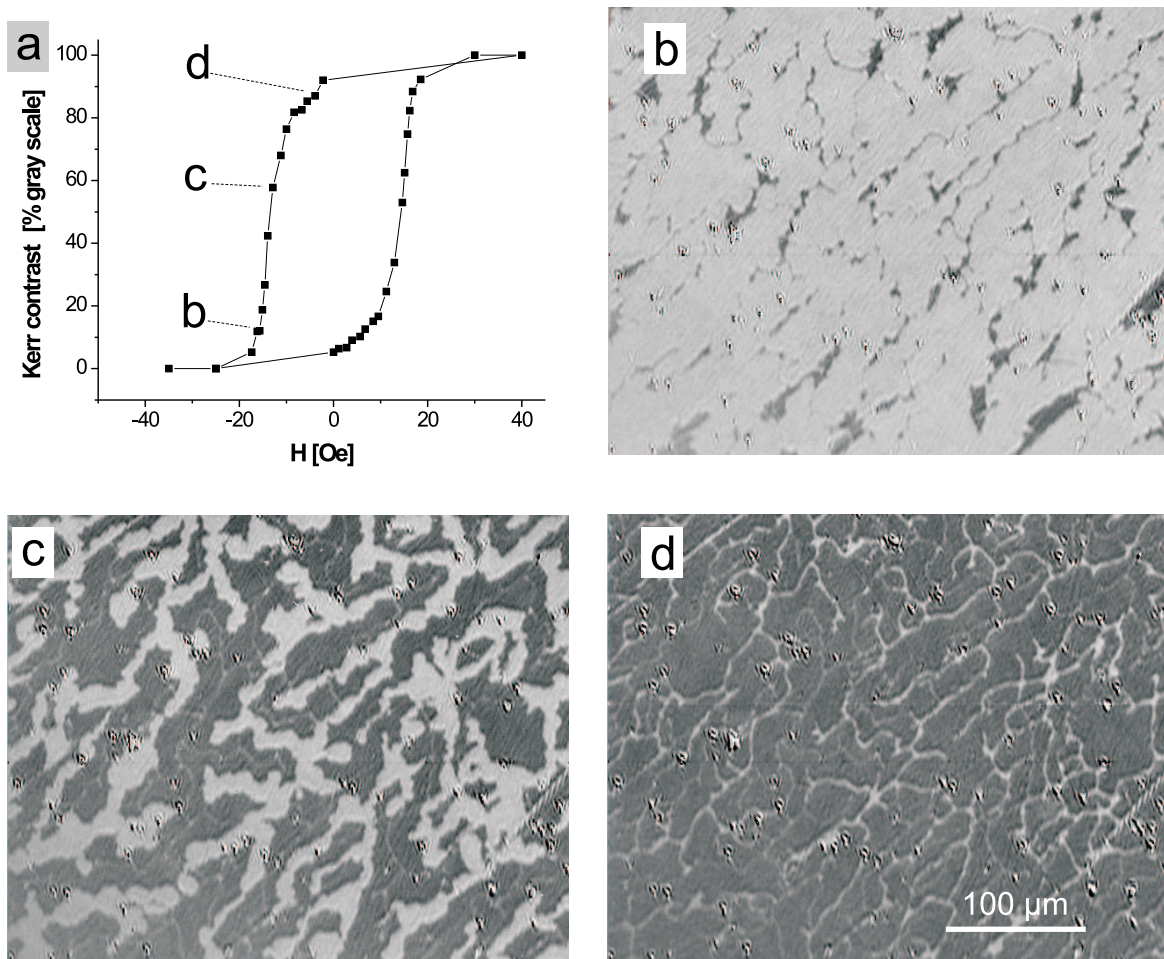


Figure 2.17: Series of Kerr microscopy images taken on 3 ML Fe film on Cu(100) at 130 K. The film was evaporated at the same temperature. **b–d:** The reversal magnetization process is mapped at different magnetic fields. The hysteresis curve is shown in the upper left figure. Each point in the polar hysteresis curve corresponds to the calculated Kerr contrast of a taken image.

Chapter 3

Complementary magnetic imaging with Kerr/MFM

The UHV apparatus was equipped with two separate techniques to image domains in ferromagnetic systems, Kerr microscopy and magnetic force microscopy. The experimental setup was fully described in Chap. 2. In the following it will be shown that this combination of both techniques does not only extend the lateral range in which domains can now be imaged. It will also be demonstrated that both techniques deliver complementary information and can complete each other. As an example it is shown that alterations on the domain structure of an epitaxial Fe film due to the magnetic stray field of the MFM tip can be traced by the Kerr microscope. The well-defined domain structure of an iron whisker is used as a standard to compare the images obtained by both techniques and to estimate the lateral resolution.

3.1 Domain imaging on an iron whisker

The well-known flux-closure domain structure of an iron whisker has been imaged by both techniques, Kerr microscopy and MFM. The combination of both techniques provides information about domains and the domain walls. An iron whisker is a single crystal of several mm length and $\sim 200 \mu\text{m}$ width. The surfaces are (100) planes of the bcc lattice. The magnetization of the domain areas lies in the crystal plane. Two basic domains are found along the long axis of the whisker, separated by a 180° wall. Flux closure domains are formed at each end, reducing the external stray field to a minimum. This classical domain pattern is called Landau-Lifshitz structure (Fig. 3.1). A Kerr image of the Landau-Lifshitz structure of an iron whisker is shown in Fig. 3.2a. Different contrasts in the image correspond to three different magnetization directions, as indi-

cated by white arrows. MFM allows to image the same spot on the whisker, where 180° and 90° walls meet, with higher resolution. Such an image is shown in Fig. 3.2b. Only contrast resulting from the internal wall structure appears in the image. Unlike in the

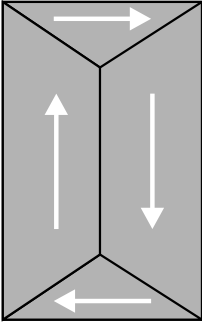


Figure 3.1:
Flux-closed
domain pattern.

Kerr image here no magnetic contrast is seen from the in-plane. Black and white contrast only arises from the 90° walls and the 180° wall separating the in-plane domains. The monopolar contrast of the 90° walls shows the different magnetization paths of Bloch walls. Also the appearance of dipolar contrast has been observed and was attributed to a rotation of the surface part of the domain wall caused by the tip field [79]. The latter produces a more antisymmetric line profile for the repulsive tip-sample interaction.

The half width of the 180° wall is 230 nm (Fig. 3.3). This value is a factor of three larger than the theoretically predicted width of ~ 70 nm [24]. The lateral stray field distribution around the magnetized MFM tip is one of the main limiting factors for the lateral resolution. Other limiting factors were discussed in Chap. 2.

The image in Fig. 3.2b was taken in constant distance mode, while the image in Fig. 3.2c is taken in constant signal mode. In constant signal mode technique the tip scans much closer to the sample surface. Therefore the method detects non-magnetic and magnetic signals. The magnetic contrast already seen in Fig. 3.2b is therefore superimposed here by structural contrast from the whisker surface. In Fig. 3.2b the tip is some 10 nm away of the sample surface (constant distance mode) and only sensitive to the long-ranging magnetic force. Therefore only magnetic contrast is visible. In order to obtain a MFM

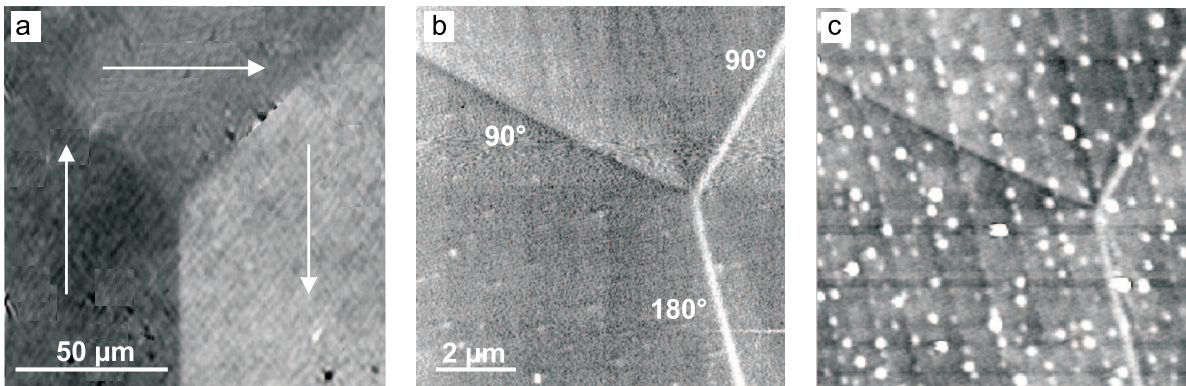


Figure 3.2: **a:** Kerr image of an iron whisker. MFM scan in **b:** static and **c:** dynamic non-contact mode, respectively. Two 90° Bloch-walls with different magnetization path and a 180° wall can be seen.

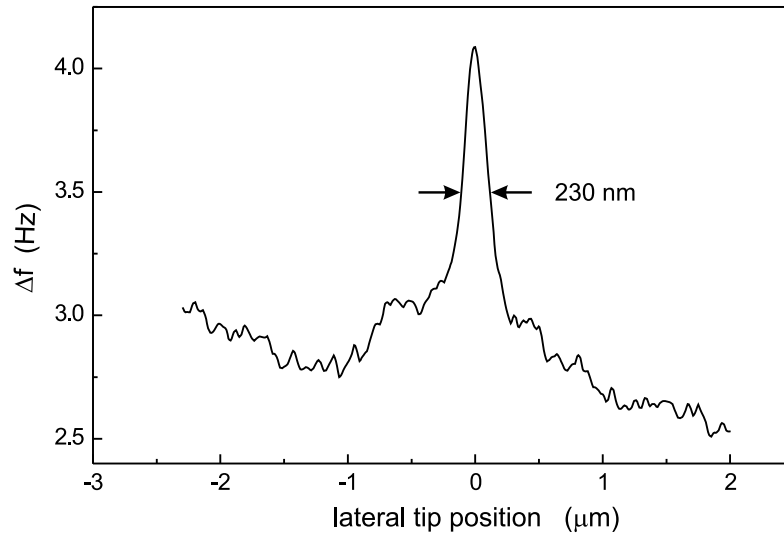


Figure 3.3: MFM line scan of a 180° domain wall. The full width at half maximum is 230 nm.

image of the surface with magnetic contrast only, a large tip-surface distance is necessary. This, on the other hand, decreases the lateral resolution due to the larger component of the tip stray field. Also the contrast is reduced at larger distances due to the smaller magneto-static interactions. In the experiment one has to find the optimum distance with good magnetic contrast and resolution, while structural contrast is suppressed.

3.2 Domain wall displacement in epitaxial Fe films

To achieve a high lateral resolution, the tip has to be brought as close as possible to the sample surface. On the other hand a short tip-sample distance causes a strong magneto-static interaction between tip and surface. That means the stray field of the tip influences the magnetization of the sample and vice versa. Therefore in soft magnetic samples the MFM tip often leads to alterations of the sample magnetization. This is also observed in Fig. 3.4 on a 3 ML thin Fe on Cu(100) film, grown and imaged at 130 K. The as-grown multidomain pattern at low temperatures was described already in this work (Sect. 5.1). It is now imaged with Kerr microscopy and MFM, as shown by the sequence in Fig. 3.4. The dark and bright contrast in the Kerr images in Fig. 3.4a and f is due to magnetic domains with magnetization in-plane or out-of-plane. These Kerr images are taken without background subtraction. Thus, defects on the sample surface are visible. These defects are used to guide the MFM tip to the same spot on the sample surface previously seen by the Kerr microscope under control of an optical telescope. The same magnetic domain, as highlighted by a white square in the Kerr image in Fig. 3.4a, can be found by MFM. It is further investigated with the enhanced resolution of the MFM

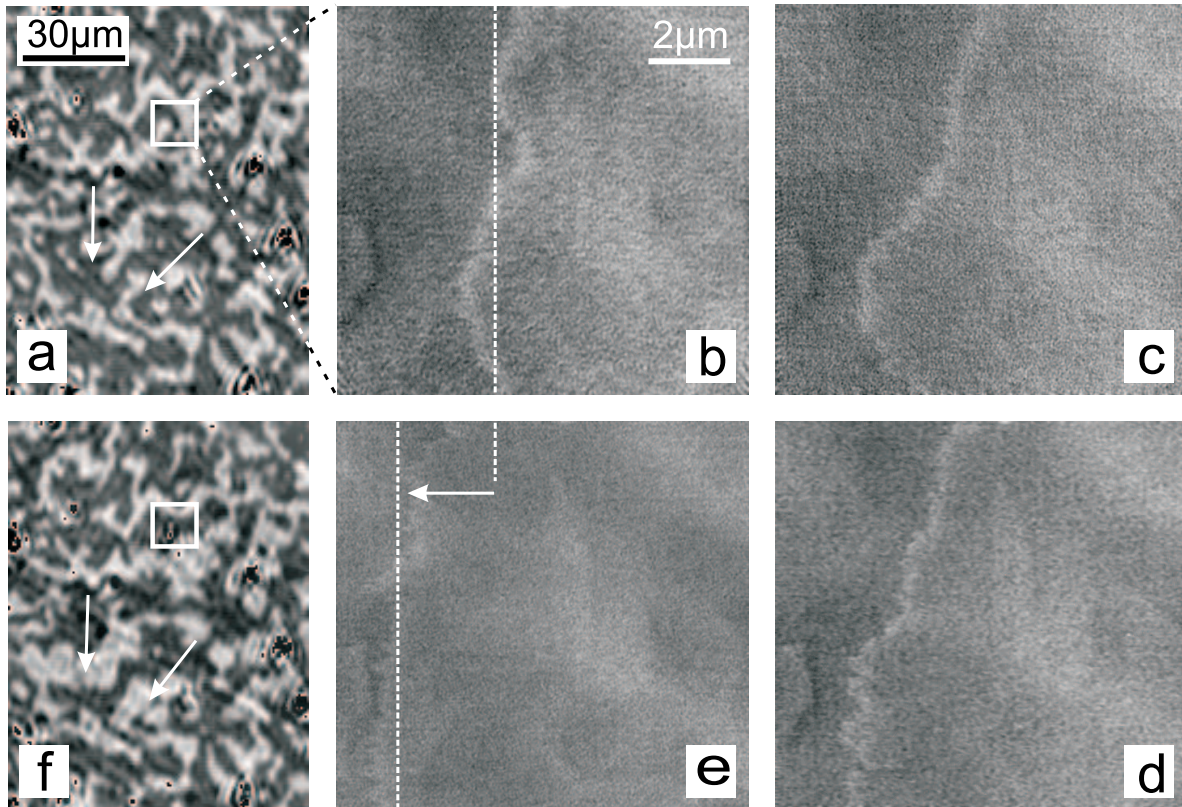


Figure 3.4: Kerr effect image before (a) and after (f) several MFM scans (b–e) of the same magnetic domain of a 3 ML thick film on Cu(100) taken at 130 K. Between figure b and e the tip to sample distance was reduced to 60 nm. The dotted line marks the domain wall motion caused by the increasing stray field of the tip. The arrows denote domains displaced by the tip.

(Fig. 3.4b). The domain wall separating two regions of perpendicular magnetization is clearly visible in the center of the image in Fig. 3.4b. After acquisition of the MFM image in Fig. 3.4b in constant height mode the distance between sample and MFM tip was gradually reduced by 20 nm steps (Fig. 3.4b to e). With decreasing distance the dipolar field of the magnetic tip acting on the film became strong enough to drag the domain wall during scanning. The MFM image in Fig. 3.4c already shows the domain wall slightly displaced towards the left border of the image. Finally, in Fig. 3.4e the domain is almost driven out of the imaged region. The Kerr image in Fig. 3.4f subsequently taken after the MFM studies on the same spot clearly shows these alterations. Other changes in the domain pattern, marked by white arrows in the Kerr images, are also visible in Fig. 3.4f and are due to previous MFM scans on different positions.

In conclusion: a direct correlation between two different domain imaging techniques, Kerr microscopy and MFM could be achieved. In the case of the Fe whisker magnetic contrast of the in-plane domains was achieved by Kerr microscopy, while MFM mainly delivered information about the domain walls. In epitaxial Fe films on Cu(100) the Kerr microscope was used to reveal alterations in the film magnetization due to the tip stray field.

Chapter 4

Magnetic reorientation transition in ultrathin films

In this chapter the relevant magnetic energy contributions to the total energy of ferromagnetic samples are discussed, with emphasis on the unique magnetic properties of epitaxial films. The spin reorientation transition often found in thin films at a critical thickness is described as the result of competing energy contributions.

The structural and magnetic properties of Fe films grown at 300 K and at low temperatures on Cu(100) substrates are summarized. The influence of adsorbates on the magnetic properties of these films is outlined.

4.1 Energy contributions to the magnetic anisotropy

Characteristic for ferromagnetism is the presence of spontaneous magnetization below a certain temperature, the Curie temperature T_c , in absence of any external magnetic field. The origin of ferromagnetism in the 3d transition metals, Fe, Co and Ni is the exchange coupling, which tends to align neighboring spins parallel. According to the Pauli principle, a parallel spin alignment requires extra energy, which is gained by increasing the interatomic distance, which on the other hand lowers the Coulomb energy. The energy expense for parallel spins is overcompensated by the gain in Coulomb energy if the Stoner criterion is fulfilled. A priori there is no directional dependence involved in magnetism, originating from the exchange interaction. However, in single crystals energy contributions arising from spin-orbit interaction and dipolar interactions make certain directions within the crystal more favorable than others. These directions are

called “easy axes of magnetization”. The energy required to rotate the magnetization away from the easy axis to any other directions is called the anisotropy energy with respect to these directions. In the following, the relevant contributions to the magnetic anisotropy are described.

Magneto-crystalline anisotropy

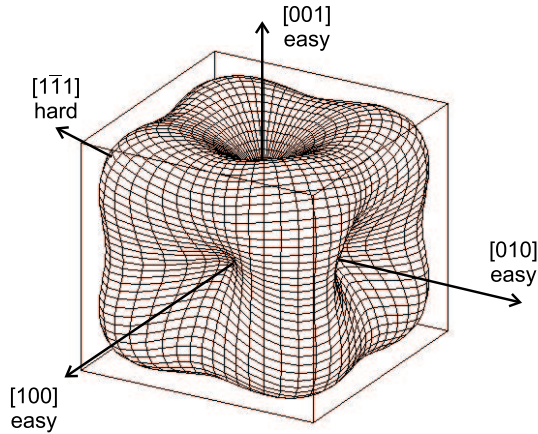


Figure 4.1: Anisotropy energy f_{MC} as function of the crystallographic directions of a cubic crystal structure. The hard directions are given by maxima in f_{MC} .

When considering only crystals with cubic symmetry (e.g. Fe, Ni), f_{MC} can be expressed in a power series of trigonometric functions:

$$f_{MC} = K_4(\alpha_1^2\alpha_2^2 + \alpha_1^2\alpha_3^2 + \alpha_2^2\alpha_3^2) + K_6(\alpha_1^2\alpha_2^2\alpha_3^2) \quad (4.1)$$

where K_4 and K_6 are the fourth and sixth order anisotropy constants. In the case of iron $K_4 = 4.2 \cdot 10^4 \text{ J/m}^3$ and $K_6 = 1.5 \cdot 10^4 \text{ J/m}^3$ at room temperature [80]. The equation contains only terms higher than the third order in α , because of the cubic symmetry of the lattice. In Fig. 4.1 the magneto-crystalline anisotropy energy is plotted as a function of the crystallographic direction for a single crystal with cubic symmetry and $K_4 > 0$, i.e. Fe. The easy axes are along the $\langle 100 \rangle$ directions due to the minimum in f_{MC} . In contrast, the hard axes lie along the $\langle 111 \rangle$ directions and are recognized by maxima in the magneto-crystalline anisotropy energy. In the case of Ni the K_4 has a negative sign, therefore the $\langle 100 \rangle$ are the hard and the $\langle 111 \rangle$ are the easy axes of magnetization. Depending on K_4 , f_{MC} corresponds to an energy contribution of $10^{-6} - 10^{-4} \text{ eV/atom}$.

For undistorted spherical single crystalline samples the work required to turn the magnetization from easy direction to hard direction is given by the magneto-crystalline anisotropy f_{MC} . This magneto-crystalline anisotropy originates from the spin-orbit interaction: spins are coupled to the electron orbits, which are on its own exposed to the crystal field. Therefore, usually the magneto-crystalline anisotropy mirrors the symmetry of the crystal lattice. The magneto-crystalline anisotropy is assumed to be a function of the direction cosines α_1, α_2 and α_3 of the magnetization vector \mathbf{M} with respect to the crystallographic axes.

Magneto-elastic anisotropy

The volume and the shape of a crystal underlie changes, if external forces are applied. Any distortion of the crystal lattice acts on the spins via the spin-orbit interaction and therefore gives rise to a strain dependent energy contribution, the so called magneto-elastic energy (f_{ME}). This contribution describes to what extent an applied strain modifies the energy and thus the anisotropy of the sample. The f_{ME} is also the origin of magnetostriction, that is the spontaneous lattice distortion upon magnetization. The most general expression to describe the magneto-elastic energy is:

$$f_{ME} = \sum_{i,j,k,l} B_{ijkl} \varepsilon_{ij} \alpha_i \alpha_j + \dots \quad (4.2)$$

B_{ijkl} , are called the magneto-static coupling constants. Considering again only structures with cubic symmetry, the magneto-elastic energy can be written as [81]:

$$f_{ME} = B_1(\varepsilon_{11}\alpha_1^2 + \varepsilon_{22}\alpha_2^2 + \varepsilon_{33}\alpha_3^2) + 2B_2(\varepsilon_{12}\alpha_1\alpha_2 + \varepsilon_{23}\alpha_2\alpha_3 + \varepsilon_{31}\alpha_3\alpha_1) + \dots \quad (4.3)$$

where ε_{ij} are the components of the strain tensor and B_1 and B_2 are the magneto-elastic coupling constants for cubic lattices. Latter explain to what extent the magneto-elastic energy depends on the strain in the crystal. For Fe these coefficients are $B_1 = -3.43 \cdot 10^6 \text{ J/m}^3$ and $B_2 = -7.97 \cdot 10^6 \text{ J/m}^3$ [82]. Therefore in some cases small strains of less than 1% can give f_{ME} exceeding f_{MC} , thus determining the easy axis of magnetization. Especially during the epitaxial growth of ultrathin films the lattice mismatch between substrate and film can cause film strain as high as 10%, as in the case of Fe/W, and higher. The magneto-elastic contribution can therefore significantly influence the magnetism. A negative sign of B_1 indicates that the direction of the applied strain is also favored as easy axis, if the strain is sufficiently large. In contrast, a positive sign pushes the magnetization away from the strain direction, as in the case of Ni ($B_1 = +6.21 \cdot 10^6 \text{ J/m}^3$).

Shape anisotropy

The preferred direction of magnetization of a ferromagnet also depends on its shape. This contribution originates in dipolar interactions. For a spherical specimen with isotropic shape the anisotropy energies depend only on the orientation of the magnetization with respect to the crystalline axes. In the case of a thin plate on the other hand the magnetization curves for in-plane and out-of-plane magnetization are found to be different. Spontaneously the magnetization lies within the film plane, since out-of-plane magnetization creates large surface poles and requires thus higher energy. This

effect is called the shape anisotropy (f_{shape}). The shape anisotropy is a consequence of the anisotropic demagnetizing field H_d , given by $H_d = -4\pi\mathbf{NM}$, where \mathbf{N} is the demagnetizing tensor. When considering a ellipsoidal ferromagnet with the half axes a , b and c the shape anisotropy is given by:

$$f_{shape} = \frac{\mu_0}{2}M^2(N_a\alpha_1^2 + N_b\alpha_2^2 + N_c\alpha_3^2) . \quad (4.4)$$

N_a, N_b and N_c are the demagnetizing factors in direction of the main axis and α_i the direction cosines. It is $N_a + N_b + N_c = 1$. Values for N for various aspect ratios are listed in [83]. Therefore in non-spherical bodies the energy is anisotropic. The shape anisotropy plays an important role for the magnetization of thin films and small particles.

Magnetic anisotropies in ultrathin epitaxial films

In the previous considerations about the magnetic anisotropy terms, no restrictions were made on the dimensionality of the ferromagnetic crystal systems. In contrast, for ultrathin epitaxial films or multilayered systems, the magnetic anisotropy can be markedly different from the respective bulk materials. Mainly the modified electronic structure of surfaces, the layered shape and epitaxial strain can alter the magnetism in thin films. With increasing film thickness the influence of the interfaces decreases and the magnetic properties approach eventually bulk behavior. One effect sometimes found in thin film magnetism is the existence of an easy axis of magnetization perpendicular to the film plane. Such a perpendicular anisotropy can be a consequence of the dominating interface contributions to the magnetic anisotropy energy [8]. This contribution can be large enough to exceed the shape anisotropy in ultrathin ferromagnetic films favoring in-plane magnetization, as shown previously. Such a transition of the easy axis from in-plane to out-of-plane is known as reorientation transition (ROT) of magnetization and occurs at a critical thickness (t_{crit}).

Now all relevant energy contributions to the total energy of thin epitaxial films are summarized. This model is then used to describe adsorbate and thermally induced changes of the ROT in LT grown films on Cu(100) in Chap. 5. Considering only magnetism relevant contributions, the total energy of a ferromagnetic thin film can be written as the sum of magneto-crystalline anisotropy f_{MC} , the magneto-elastic energy f_{ME} , the magneto-static energy f_{shape} and a surface term f_{surf} , which considers interface effects described above, $f_{tot} = f_{MC} + f_{ME} + f_{shape} + f_{surf}$. The magnitude of f_{tot} depends mainly on the direction of magnetization, lattice strain with respect to bulk, ε_i , and the film thickness t . Neglecting terms of higher than fourth order, f_{MC} takes the form

$$f_{MC} = K_4 (\alpha_1^2\alpha_2^2 + \alpha_2^2\alpha_3^2 + \alpha_3^2\alpha_1^2) . \quad (4.5)$$

The magneto-elastic term f_{ME} in equation (4.3) simplifies in cubic systems to

$$f_{ME} = B_1(\varepsilon_{\perp} - \varepsilon_{\parallel}) \alpha_3 \quad (4.6)$$

under the assumption of homogenous in-plane strain ε_{\parallel} and strain ε_{\perp} perpendicular to the plane, with respect to bulk lattice dimensions. Expression (4.6) reflects the difference in magneto-elastic energy between magnetization out-of-plane ($\alpha_3 = 1$) and in-plane ($\alpha_1 = 1$). If f_{ME} is negative, f_{tot} is decreased and out-of-plane magnetization is favored. The term of the shape anisotropy derived from Eq.(4.4):

$$f_{MS} = \frac{1}{2} \mu_0 M_S^2 \alpha_3^2 \quad (4.7)$$

and is always a positive energy contribution. If the magnetization rotates out-of-plane, making it energetically unfavorable, due to the creation of a magnetic dipole field. Here, the demagnetization factor for thin plates, $N_c = 1$, is already taken into account. Finally, the interface term

$$f_{surf} = -\frac{(K_{f-vac} + K_{f-s})}{t_f} \alpha_3^2 \approx -\frac{2K_S}{t_f} \alpha_3^2 \quad (4.8)$$

summarizes all interface effects which lead to a deviation from bulk behavior, by introducing the interface anisotropy constants K_{f-vac} and K_{f-s} , for the surface and the film-substrate interface, respectively. The f_{surf} decays with increasing film thickness. Both interface anisotropy constants take into account interface effects such as the modified electronic structure and the roughness of each interface. Adsorbate induced changes in reorientation transition as presented in this paper, are attributed to a modified K_{f-vac} , while in these experiments K_{f-s} is assumed to be unchanged. Often though, $K_{f-vac} = K_{f-s} = K_S$ is assumed for simplicity and experimentally confirmed for several systems. To determine the easy axis of magnetization as a function of film thickness, the difference in total energy for a thin film between out-of-plane and in-plane magnetization is calculated using equations 4.5 to 4.8, which is

$$f_{tot}(\perp) - f_{tot}(\parallel) = \Delta f_{tot} = B_1(\varepsilon_{\perp} - \varepsilon_{\parallel}) + \frac{1}{2} \mu_0 M_S^2 - \frac{K_{f-vac} + K_{f-s}}{t_F}. \quad (4.9)$$

If Δf_{tot} is positive, in-plane magnetization is preferred. In contrast, for negative Δf_{tot} , perpendicular magnetization is expected. A change in sign of Δf_{tot} from negative to positive with increasing t_F indicates a reorientation transition for the magnetization into the plane, as can be seen in Fig. 4.2. The intersection of the function with the x-axis ($\Delta f_{tot} = 0$) gives the condition for the critical thickness t_{crit} :

$$t_{crit} = \frac{2(K_{f-vac} + K_{f-s})}{2B_1(\varepsilon_{\perp} - \varepsilon_{\parallel}) + \mu_0 M_S^2}. \quad (4.10)$$

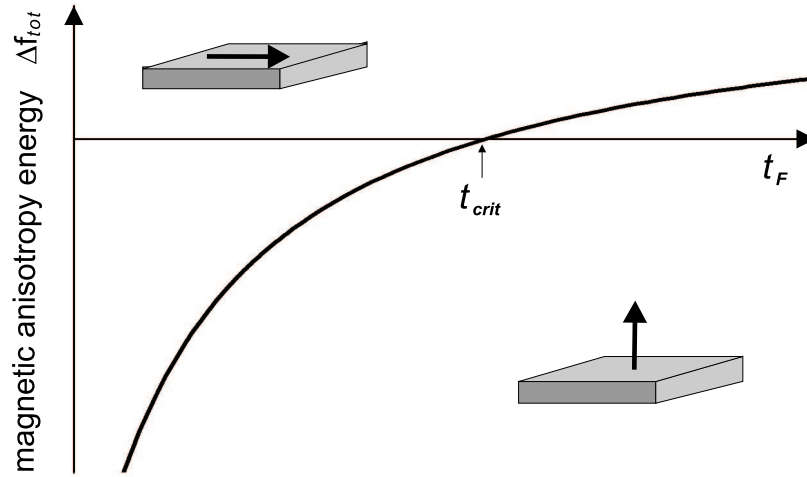


Figure 4.2: Thickness dependent switching of the magnetization direction at t_{crit} as result of the competition between surface and shape anisotropy.

This phenomenological model is used together with the experimental results presented in this thesis to deduce adsorbate and thermally induced changes of the surface anisotropy constants.

4.2 Structural and magnetic properties of Fe/Cu(100)

For the study of the correlation between film structure and magnetism epitaxial Fe films on Cu substrates are of particular interest. This is due to the difference in the crystallographic structure. Fe has a bcc structure in the bulk phase, while Cu has a fcc structure. It has been shown that epitaxial Fe films can be stabilized on the Cu substrate in a fcc structure below a certain film thickness already at RT, resulting in a small epitaxial misfit of only 0.7% [84]. This so called γ -phase is found in bulk Fe only at a temperature above 1184 K. It is therefore unique to epitaxial films that materials can be stabilized in a crystallographic structure other than bulk structure. In addition to Fe/Cu this was also observed (for example) for Fe/Ni [85] and Fe/Ag [86].

Besides the structure, these films also show unique magnetic properties such as perpendicular magnetization. With increasing film thickness the film undergoes structural and magnetic transitions in order to approach its bulk behavior. The study of these transitions can give insight in the origin of the particular magnetic properties of ultra-thin films and has stimulated extensive work so far. However, many open questions still remain.

Depending on the film preparation technique (i.e. pulsed laser deposition, thermal evaporation) [87, 88], the deposition rate [89, 90] or growth temperatures [91], different film structures with different magnetic properties can be created. Since a considerable interdiffusion between Fe and Cu was found at elevated temperatures, so far only RT and LT at less than 140 K grown Fe films have been investigated. The focus has always been on RT grown Fe because of the layer by layer growth found at this temperature. The properties of RT as well as LT grown Fe films on Cu(100) will be reviewed in the next following.

Fe films grown at 300 K

For Fe films grown at RT on Cu(100) three different structural and magnetic phases have been identified with increasing film thickness in MEED [92], LEED [93, 94], magnetic circular dichroism in x-ray absorption spectroscopy (MCXD) [95] and MOKE [96] measurements. Initially in region I, from 0 to 4 ML, the Fe film growth starts with nucleation of double layer islands, followed by nearly layer by layer growth. A slight intermixing at RT has been reported [97, 98]. The epitaxial Fe film grows pseudomorphically and adopts the in-plane interatomic distance of the Cu(100) of $a_{Cu} = 3.6147 \text{ \AA}$, whereas in normal direction the interlayer spacing is enlarged by 5% to $a_{\perp} = 1.88 \text{ \AA}$ [31, 99]. This expansion is not a Poisson-like response to the in-plane strain since both have the same sign. In region I the film is therefore tetragonally distorted (fct) (Fig. 4.3a).

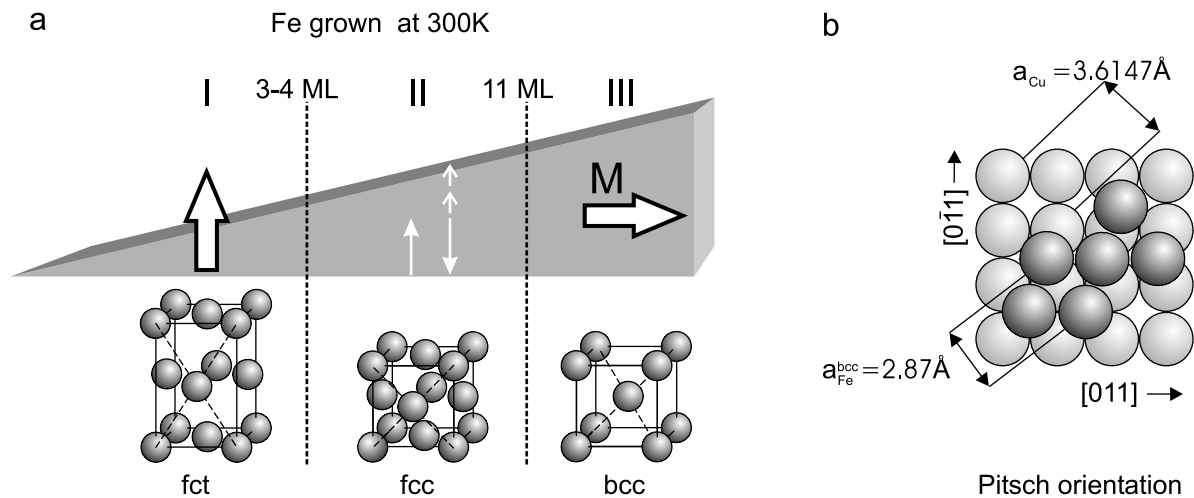


Figure 4.3: **a:** Schematic view of Fe wedge on Cu(100) substrate. With increasing thickness three phases with different structural and magnetic properties are found. **b:** Alignment of a bcc-layer of Fe (dark spheres) with respect to the Cu substrate (bright spheres).

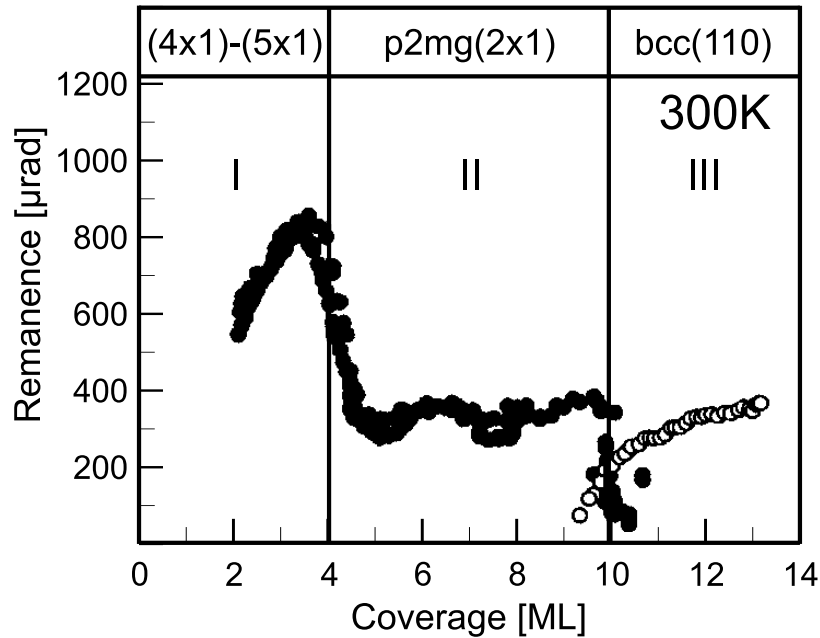


Figure 4.4: Polar and longitudinal MOKE signal of Fe/Cu(100) film as a function of coverage. The film is grown at 300 K. The different magnetic phases are indicated with I, II, and III (according to [31]).

In the thickness range between 4 and 11 ML (region II) a good layer by layer growth is found and characterized by regular intensity oscillations in MEED experiments. In this region the film shows an undistorted face centered cubic (fcc) structure with the two topmost layers remaining expanded [100]. In phase III above 11 ML the film structure has completely transformed into the thermodynamically stable bcc structure of α -iron. The bcc iron is aligned with respect to Cu in a so-called Pitsch orientation, where the [111]-direction of bcc iron is aligned parallel to the [110]-direction of the fcc substrate [101,102]. The real space model of this structure can be seen in Fig. 4.3b.

In experiments of [84], the γ -phase could be stabilized with surfactants up to 60 ML. In the latest STM measurements elongated bcc precipitates have been found at a film thickness of approximately 7 ML [103]. From that the question arises, if the onset of the structural transition, the martensitic transformation (coexistent fcc and bcc phases), takes place which was assumed till now at a higher thickness at around 11 ML.

In this thickness range the Fe film has three different magnetic phases. The long range ferromagnetic order starts around 1 ML. Also an onset of ferromagnetism at 2 ML of Fe was reported and attributed to the onset of coalescence of the second layer. Films below a thickness of 4–5 ML exhibit a perpendicular magnetization. The magnetization increases linear with the Fe thickness, as was demonstrated in polar MOKE measurements [31]. This magnetic phase I is succeeded by a phase II with reduced magnetic

moment (Fig. 4.4). The magnetization is found to drop down to a value corresponding to that of 2 ML Fe in phase I [104]. It was confirmed experimentally by MOKE [96, 105] and theoretically [106] that this phase consists of a film with antiferromagnetic (AF) spin alignment and with the top most two layers coupled ferromagnetically. In this phase a two peak behavior in the remanent signal M_R with increasing thickness was discovered in [107] after cooling the film to 70 K and explained by alternating sheets of spins. Measurements of Kirschner et al. [108] show oscillations in the polar MOKE amplitude between 6 and 9 ML. Spin density-waves in the AF phase are proposed, as was already suspected in [107]. In phase III above 11 ML the easy axis of magnetization lies within the film plane [96, 105]. The transition is characterized by a critical thickness at which the spin reorientation occurs. Since the thickness for magnetic transitions more or less coincides with the structural changes, $fcc \rightarrow fcc \rightarrow bcc$ (Fig. 4.3), the magnetic phases were firstly ascribed to magneto-volume effects [84, 109]. On the other hand theoretical work points out the dominating contribution of the Fe substrate interface to the magnetic anisotropy energy (MAE) due to electronic effects, namely band narrowing and hybridization [32]. Recent experiments with adsorbates support the usual assumption of a dominating surface contribution to MAE rather than magneto-volume effects [34]. In this picture, as was explained in the previous chapter, the perpendicular magnetization in phase I is due to the dominating contribution of the Fe vacuum interface, expressed in a positive K_{f-vac} . This assumption will be supported by experiments with O_2 and CO adsorbates in this thesis.

The transition between phase II and phase III at 11 ML is most likely due to the fcc-bcc transition of the film structure.

LT grown Fe film

In order to prevent segregation of Cu to the Fe surface and to minimize intermixing at the Fe-Cu interface, iron can be deposited at substrate temperatures below 140 K [97]. The growth at LT leads to an enhanced surface roughness, as was observed in LEED and STM [110]. With increasing thickness the film morphology changes. The enhanced roughness was the main reason why RT grown Fe are favored in most investigations. Smooth Fe layers provide a better system for theoretical modelling. On the other hand, LT grown Fe provides the opportunity to observe temperature driven structural changes in the film and its consequences for the film magnetism. Also, a comparison of the differences between LT and RT grown Fe might help to understand the correlations between structure and magnetism. This thesis therefore focuses on the investigation of Fe grown at 130 K.

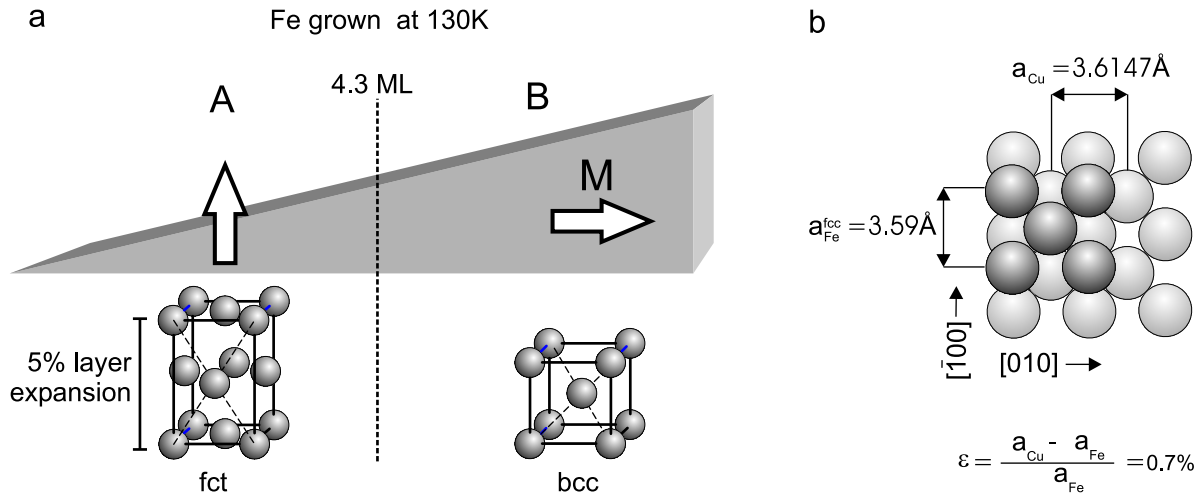


Figure 4.5: **a:** Magnetic and structural phases in LT grown Fe/Cu(100). In comparison to RT grown films phase II does not exist. **b:** Pseudomorphic fcc iron unit cell and resulting strain ϵ , due to the lattice mismatch to the Cu substrate.

Often LT grown Fe films were annealed to 300 K after growth to smoothen the surface. Such annealing causes a sharpening of the LEED spots and the appearance of different layer dependent superstructures (5×1) , (3×1) , (4×1) . It was found that annealing to RT produces no significant intermixing. Nevertheless the annealed films show still a higher roughness and a more island-like surface than the RT grown films [110, 111]. It is therefore assumed that the magnetic properties in this system are influenced by reasons other than the electronic structure.

In the submonolayer region the film nucleates with bilayer islands and high island density. Different results have been found for the onset of coalescence, indicating some sensibility of the system to the preparation conditions. A minimum coverage of about 1.2 ML was reported for the island percolation in the first layer [110]. In recent STM measurements the bilayer island coalescence was found at less than one monolayer deposited Fe [38]. At higher thickness the island density does not change significantly because of the reduced diffusion at LT. At such low temperatures the mobility of the atoms is strongly reduced, as was recently shown for Fe on bcc Fe(110) [112]. Only after annealing to 420 K in the case of Fe/Cu(100) an atomically flat Fe film was obtained [111]. But annealing to such temperatures causes a significant intermixing between Fe and Cu.

A striking difference between LT and RT films is the absence of phase II in structure and magnetism. A transition from the fct phase A¹ directly to the bcc phase B is observed at $t \sim 4\text{--}5$ ML (Fig. 4.5). No intermediate fcc phase was reported. An AF magnetic phase

¹Following a convention of Wuttig et al. [113]. Magnetic phases in LT grown Fe films are marked (A, B), in RT grown films marked (I, II, III).

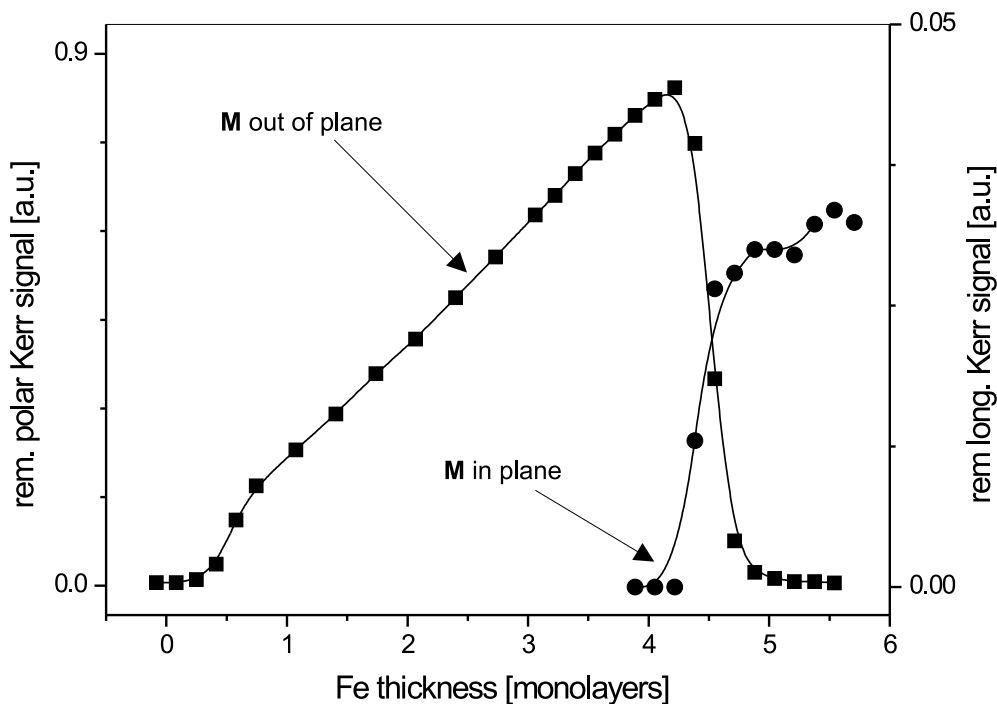


Figure 4.6: Remanent Kerr ellipticity for a film grown and measured at 130 K without subsequent annealing. Perpendicular (squares) and parallel (circles) spontaneous magnetization is shown versus the Fe film thickness.

does not exist, instead, the easy axis reorients from out-of-plane to in-plane directly at $t_{crit} = 4.3$ ML. In Fig. 4.6 the MOKE ellipticity measured at remanence as function of Fe coverage is shown. A wedge-like Fe film was grown and measured at 130 K without annealing to RT. The square symbols denote the remanent Kerr signal obtained in polar geometry. The Kerr signal increases linearly with the Fe thickness, except for the region below one monolayer. The onset of ferromagnetic order was observed below one monolayer at 0.7 ML. In literature values between 0.9 ML and more than 2 ML [74, 96, 114, 115] have been reported for this onset. The delayed onset was attributed to magnetic percolation [116]. Also Curie temperature effects can cause such a behavior. At a thickness slightly above 4 ML the intensity of the polar signal drops down to zero, and instead the longitudinal signal M_{\parallel} increases. The intensity of the polar signal is about one magnitude higher than the longitudinal one, depending also on geometric factors of the MOKE setup [117]. In agreement with [116], we did not observe the vanishing of both magnetization components M_{\parallel} and M_{\perp} at t_{crit} as was observed by [118] with spin-polarized secondary electron emission spectroscopy (SPSEES). A coexistence of M_{\parallel} and M_{\perp} with a reduced remanent magnetization $M = (M_{\parallel}^2 + M_{\perp}^2)^{1/2}$ in the transition range was reported. We have determined the critical thickness at which

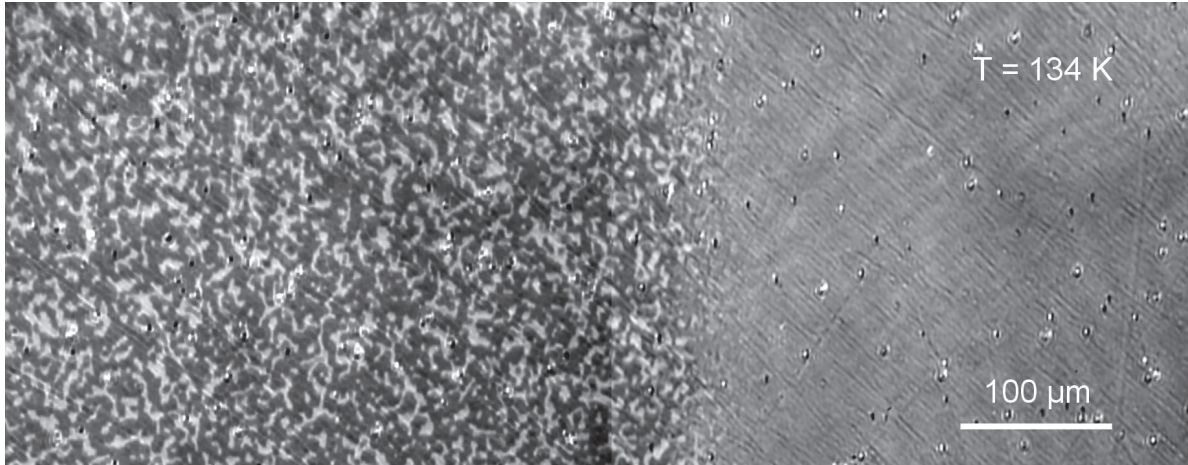


Figure 4.7: Virgin magnetic domain image of Fe film. The wedge like film was deposited and measured at 134 K without annealing. Thickness increases from left to right. A nearly constant domain size below $t_{crit} = 4.3$ ML (light and dark areas) is visible.

the reorientation occurs at 4.3 ML. In literature, values for t_{crit} between 3.8 ML and 6.1 ML are reported [17, 119, 120]. This gives another indication for the dependence of magnetization on the preparation conditions [17, 102].

To determine the influence of the annealing process, in particular on the coercivity, hysteresis loops with and without subsequent annealing have been investigated with MOKE [102] on wedge-like films. For both cases of film preparation, regions with perpendicular and in-plane anisotropy are found, respectively. However, the films which were annealed to RT show a slightly higher critical thickness for the ROT and also the gradient of the polar ellipticity is increased. This is attributed to the film roughness and the influence of the morphology after treatment of the film.

For a better understanding of the magnetization reversal process, domain imaging is helpful. SEMPA experiments on LT grown Fe/Cu(100) laterally resolve the spin reorientation in a narrow region and reveal a multidomain state with domain size of several micrometer [116]. It is predicted that due to the reduction of the magnetic anisotropy and the increase of the dipole energy a microdomain state becomes energetically favorable at the spin reorientation transition [121]. The perpendicular virgin domain structure of an wedge-shaped Fe film on Cu is shown in Fig. 4.7. The image shows a section around $t_{crit} = 4.3$ ML. The Fe thickness increases from left to right by 2.4 ML. The domains have a thickness independent domain size between 6 and 15 μm . A slight decrease of the domain size in the vicinity of the critical thickness is visible and a rapid decay of the contrast could be found above t_{crit} . The contrast dissipates into an average grey tone representing in-plane magnetization. In a small region above t_{crit}

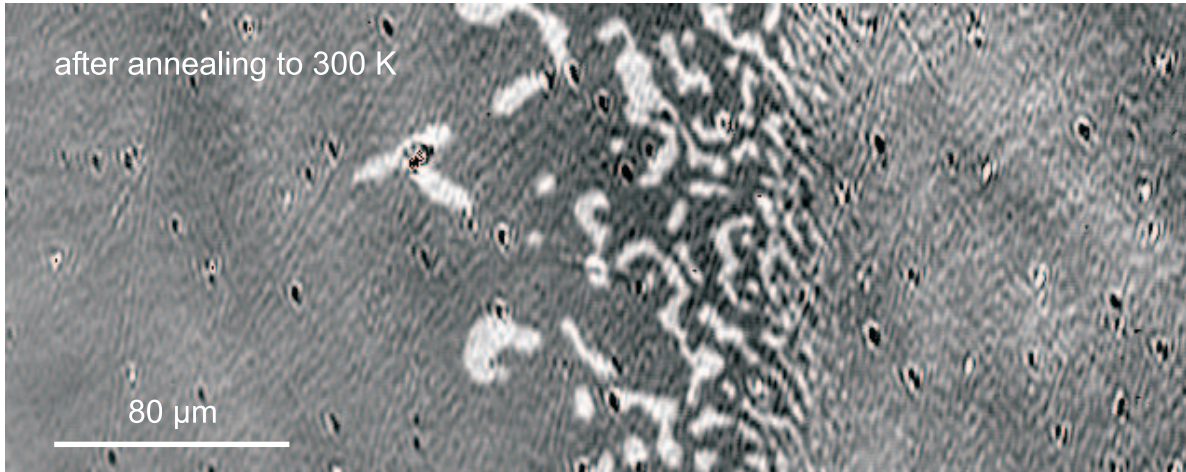


Figure 4.8: Kerr microscope image of magnetic domain state around $t_{crit} = 3.5$ ML. The LT grown, wedge shaped Fe/Cu(100) film was annealed to RT. Thickness increase from left to right. The image shows domains with perpendicular orientation (light and dark areas). Grey tone (right) presents the area with in-plane magnetization.

perpendicular domains are still visible faintly. This might indicate the coexistence of remanent perpendicular and parallel domains at the spin reorientation transition. Such a coexistence has also been suggested by Oepen et al. for the system Co/Au(111) [122]. The independent domain size in the LT film is in contrast to the thickness dependent domain size in the iron film after annealing. Figure 4.8 shows a corresponding Kerr image of a Fe wedge on Cu(100) at RT. The film was also grown at 134 K and afterwards annealed to 300 K. The Fe thickness increases from 2.7 ML to 3.9 ML from left to right. The image has been taken without background subtraction. It shows the modified virgin magnetic domain state after warming up to 300 K. During this annealing process the critical thickness shifts towards smaller film thickness to 3.5 ML. This shows the sensitive dependence of the critical thickness on the temperature of these films, as previously reported by [118]. Thermally activated changes of the ROT are investigated in detail in Chap. 6.

The domain configuration in Fig. 4.8 shows a distinctive pattern around t_{crit} . The single-domain state on the left site of the image below $t_{Fe} = 3.1$ ML branches out with increasing thickness into a multidomain state. The branching leads to a multidomain state around the ROT which cannot be resolved by our microscope. In the region $t > t_{crit}$ no domain structure was detected. As mentioned before, the sensitivity of the Kerr microscope to in-plane magnetization is reduced by more than a factor of ten and thus in-plane domains cannot be imaged. Our MOKE data, on the other hand, clearly proof the presence of a remanent in-plane magnetization above t_{crit} (Fig. 4.6).

The influence of annealing on the magnetic domain structure at the critical thickness was previously been investigated with SEMPA experiments by [123]. The appearance of domains different in size and shape in the vicinity of t_{crit} has been predicted in the theory of domain formation in perpendicularly magnetized films by [124, 125] and has been observed in experiment by [126]. The presence of the domains can be explained by the fact, that domain formation reduces the magneto-static energy and thus perpendicular magnetization can be maintained.

4.3 Adsorbate influences on the magnetic properties

As was pointed out in the previous section the origin of the perpendicular anisotropy in phase A in LT grown Fe/Cu(100) is still under discussion. Exposure of the film to adsorbates provides a powerful tool to investigate the response of the magnetism to modifications of the electronic structure at its surface. Adsorbed atoms can either donate electrons to or accept electrons from the film, thus altering energy level occupation, coordination of the surface atoms and even interlayer spacing. The response of the ROT to such perturbations caused by adsorbates therefore helps to reveal the origin of unique magnetic properties. In this work the influence of O₂, CO, NO and H₂ has been studied in more detail.

Oxygen adsorption

The consequences of oxygen adsorption for the magnetic properties in Fe/Cu films will be investigate in this work. Oxygen is known to accept electrons and to have a strong influence on the electronic interaction on films.

The influence of adsorbed oxygen on the surface magnetism was pointed out already, for instance, in early experiments performed on Fe single crystals [127]. Hysteresis loops have been recorded on Fe(100) and Fe(110) single crystals by polarized secondary electron emission (PSEE) and MOKE. Because of the large signal depth of MOKE larger than 20 nm, in the MOKE curves only a slight change is visible after adsorption of several LO₂. Strong adsorbate induced reductions of the coercive force in the topmost layers are found by more surface sensitive PSEE experiments. The authors [127] attribute this to changes in the crystal symmetry in the surface region and the bond of iron atoms at the surface. Strong effects with very low contaminations of oxygen (~ 4 at.%) are shown in spin polarized secondary electron spectroscopy (SPSEES) experiments [128] on the system Fe/Cu(100). After exposure of only 0.5 L O₂ Fe films with a thickness between 3.4 ML and 6 ML undergo a reorientation of the easy axis of magnetization

from perpendicular to in-plane. For lower O₂ coverage, the perpendicular polarization remains unchanged up to a critical coverage, above which the magnetization begins to switch into the film plane. These results are attributed to the Fe-vacuum interface, due to their high sensitivity of the anisotropy to oxygen.

Calculations [129, 130] using a semiempirical tight binding model predict a destabilization of the perpendicular phase in Fe bilayer on Ag(100) substrate, depending on the amount of adsorbed O₂. For a high oxygen coverage (1×1 O-overlayer) the calculation clearly predicts a switching of the magnetization into the film plane. In the case of low oxygen coverage (3×3 O-overlayer) the calculation predicts a perpendicular magnetization though with significant weakened anisotropy.

A strong electronic interaction with major consequences for the chemical properties of the first layers and the film magnetism is found upon oxygen adsorption on Fe/Ag(100) [131]. The density of states and the spin polarization of Fe near E_F are found to decrease gradually with O₂ coverage. A charge transfer from iron to oxygen leaving behind Fe states with majority character is assumed. On the other hand, for coverage below 1.6 L the O_{2p} states are spin polarized and show ferromagnetic coupling with the substrate. Similar effects were observed for Fe films on different substrates [132]. The formation of several oxides is reported [133–141]: oxygen is known to chemisorb dissociatively and in dependence on exposure rate, temperature and crystallographic orientation of the surface. It appears as antiferromagnetic FeO and α -Fe₂O₃ and as ferrimagnetic γ -Fe₂O₃ and Fe₃O₄. After exposure to approximately 1 L O₂, oxidation on Fe/Ag(100) can already be observed and above 3–4 L, a magnetically dead layer is formed [131, 142].

Carbon monoxide adsorption

Carbon monoxide is the classical model adsorbate to study the catalytic properties of the transition-metal surfaces. CO is characterized by simple and well studied electronic and vibrational properties. It also serves as a model system for understanding the dissociation process at surfaces. Especially the chemisorption of carbon monoxide on iron is of considerable interest [143–147], because of the position of iron in the periodic table between those transition metals which cause CO dissociation and those which do not. The interaction of CO with heteroepitaxial fcc and bcc films on Cu(100) was investigated with ultraviolet photoemission spectroscopy (UPS) and thermal desorption spectroscopy (TDS) [148]. CO bound to bcc films dissociates at RT, in contrast to CO bound on fcc films, where molecular desorption of CO is observed slightly above RT. Such a dependence on the surface orientation can be understood by the different adsorption geometries of CO on fcc and bcc Fe films. CO adsorbs on fcc Fe as a molecule in a

twofold bridge bonding sites, with the C-atom pointing towards the surface (Fig. 4.9a). On the bcc Fe the adsorption in fourfold-hollow site is preferred and the CO molecule is tilted by 55° to the surface normal [149] (Fig. 4.9b).

The electron transfer between the CO molecule and the Fe is commonly described by the Blyholder model [150]: upon chemisorption of CO the non-bonding 5σ -CO MO donates part of its electronic charge into Fe d-band, counterbalanced by a back-donation of charge density from the metal to the anti-bonding $2\pi^*$ MO of the CO, thus weakening the intra-molecular bonding. Due to this particular upright attachment of CO to the metal surface this effect is rather weak compared to the “lying-down” adsorption geometry on bcc Fe where the bonding is stronger exposed to the substrate. The influence of CO adsorbates on the magnetic properties was investigated in thin Ni films on Cu(100) [33, 151]. There an adsorbate induced shift of the critical thickness for reorientation was found upon CO adsorption and ascribed to a modified surface anisotropy, K_{f-vac} . The reorientation transition of the magnetization could be observed with Kerr effect measurements in Fe nanostripe arrays grown on stepped W(110) during the adsorption of CO [152]. Again these studies clearly show the sensitivity of the film magnetism to electronic modifications in the surface region. For a more detailed understanding of the electronic interaction ab-initio calculations are necessary. Spišak et al. predicted profound modifications of the electronic and magnetic properties of γ -Fe/Cu(100) due to chemisorbed CO by using first principles local spin density calculations [153]. Spin-orbit coupling was not taken into account in these calculations, and thus an adsorbate-induced reorientation of the magnetization, as observed in our Kerr studies, could not be modelled. Yet, a reduced magnetic moment and a change in layer spacing due to the magneto-volume effect was predicted. However, a more detailed theoretical model seems desirable and the experimental results described in Chap. 5.2 might be helpful to further improve ab-initio models of this system.



Figure 4.9: Adsorption geometries of CO on fcc and bcc iron. The iron atoms are colored dark gray, the oxygen atoms light gray and the carbon atoms black. **a:** Vertically bonding by the carbon atom to the surface in twofold bridge site. **b:** “Lying down” of the CO molecule and adsorption in fourfold-hollow site.

Other adsorbates

Hydrogen is particularly suitable for studies of electronic effects due to its simple electronic structure. Hydrogen is expected to change the magnetization of the surface layer by hybridization of the H 1s level with the 3d electrons responsible for the ferromagnetism. This can be seen as a filling of the unoccupied 3d states above the Fermi energy. On fcc Fe(100) surfaces hydrogen adsorbs dissociatively. The heat of adsorption (71 kJ mol^{-1}) is considerably less than for bcc iron ($88\text{--}109 \text{ kJ mol}^{-1}$) as was found in LEED and TDS studies [154, 155]. Therefore adsorption on bcc surfaces seems to be more favorable. It shows again a strong dependence on the surface orientation.

IV-LEED and MOKE were performed by Vollmer et al. to determine structural and magnetic changes due to hydrogen adsorption on RT grown Fe films [156]. A reversible shift of the fct-fcc transition in 4 ML films towards higher Fe thickness was found, as well as an irreversible shift of the fcc-bcc transition. The former is accompanied by an increase of the coercivity, probably caused by the coexistence of out-of-plane and in-plane domains. Mankey et al. [157] have investigated the dependence of the magnetic properties on adsorbed hydrogen of thin Fe, Co and Ni films on Cu(100). It was found that the magnetic moment in the ferromagnets Ni and Co is considerably reduced by the chemisorption of hydrogen, while in Fe films hydrogen enhances slightly the magnetic moment. Latter is ascribed to magneto-volume effects. The slight increase of the MOKE signal by $\sim 15\%$ in the case of Fe is in quantitative agreement with the results of Vollmer et al. on 4 ML Fe films. The effect there is more pronounced and ascribed to structural changes in the topmost layers after hydrogen exposure.

Also the influence of hydrogen adsorption on the reorientation transition was studied in thin Ni films, by means of Kerr microscopy [33, 151]. In contrast to most magnetic systems, the magnetization in Ni/Cu(100) switches from in-plane to out-of-plane at a critical thickness of around 10 ML [158, 159]. After hydrogen exposure, the critical thickness is strongly reduced by ~ 4 ML. The shift of the spin reorientation transition is found to be fully reversible in a temperature window around RT. From the experiment it could be excluded that the surface roughness affects the critical thickness. The change in t_{crit} is attributed entirely to a change in the surface anisotropy, as supported by calculations from the Weinberger group [32].

Another group of adsorbates is provided by metallic, ferromagnetic or non-magnetic submonolayer coverage. Experiments with submonolayer Co capping layers exhibiting an opposite effective anisotropy constant on Fe films [34], support the idea of dominating interface effects in LT grown Fe/Cu(100). In these experiments the extrapolated critical thickness is practically the same as the measured critical thickness, which implies that

the origin of the spin reorientation is the usual balance between the surface and the shape anisotropy, rather than the formation of bcc structure. From the ratio M_r/M_s , a propagation of the ROT in RT grown Fe films via a multidomain formation is concluded by [160], which assumes the coexistence of perpendicular and in-plane domains. Also recent experimental results with Cu cap layers on this system rather emphasize the dominant role of the outer Fe interface on the magnetism [104]. On the other hand, theoretical models by Weinberger et al. attribute the perpendicular anisotropy predominantly to electronic effects on the Fe-substrate interface [32]. This model implies that the film should be less sensitive to manipulation of the outer Fe-vacuum interface, which is in contrast to adsorbate experiments. The influence of symmetry breaking due to defects or steps on the magnetic anisotropy was demonstrated in adsorption experiments on Co films grown on stepped Cu(100) surface [161]. The easy axis of the Co film could be switched by 90° within the plane by only submonolayer coverage of different metal adsorbates. The origin of this observations is attributed to an additional surface anisotropy, caused by the broken symmetry at the Co steps [162].

Chapter 5

Adsorbate induced spin reorientation

In this chapter we describe the influence of gas adsorption on the magnetic properties of LT and RT grown Fe/Cu(100) films. We have investigated the micromagnetic structure of the films by means of Kerr microscopy and MOKE. Series of Kerr images taken on Fe wedges at the reorientation transition during adsorption have been analyzed to observe changes in the critical film thickness on Fe wedges. For the first time we could image consequences of different adsorbates to the surface magnetism of Fe/Cu(100) directly.

5.1 Oxygen induced spin reorientation in Fe/Cu(100)

Oxygen adsorption on LT grown films

The Kerr microscopy experiments during gas adsorption have been performed on Fe wedges with a thickness varying from 0 ML up to 8 ML. These wedges have been produced by depositing Fe over a straight metal plate mounted on the front end of the Fe evaporator, thus producing a half shadow region of deposition on the sample surface. In this region of 1.1 mm in length, the film thickness decreases almost linearly from maximum thickness to zero, forming a wedge. The length of the wedge, and thus the slope, was also modified by continuously moving the sample at up to 4 mm in front of the evaporator during deposition. The Kerr image in Fig. 5.1a shows the domain structure of an Fe wedge in a small region around the critical thickness, directly after deposition of Fe on the Cu(100) crystal at 140 K. In this image the film thickness increases from left to right. The image was taken without any magnetic field applied and shows the as-grown domain state. The critical thickness of 4.3 ML separates two regions of different magnetization. Below 4.3 ML a multidomain structure is visible. The domains with

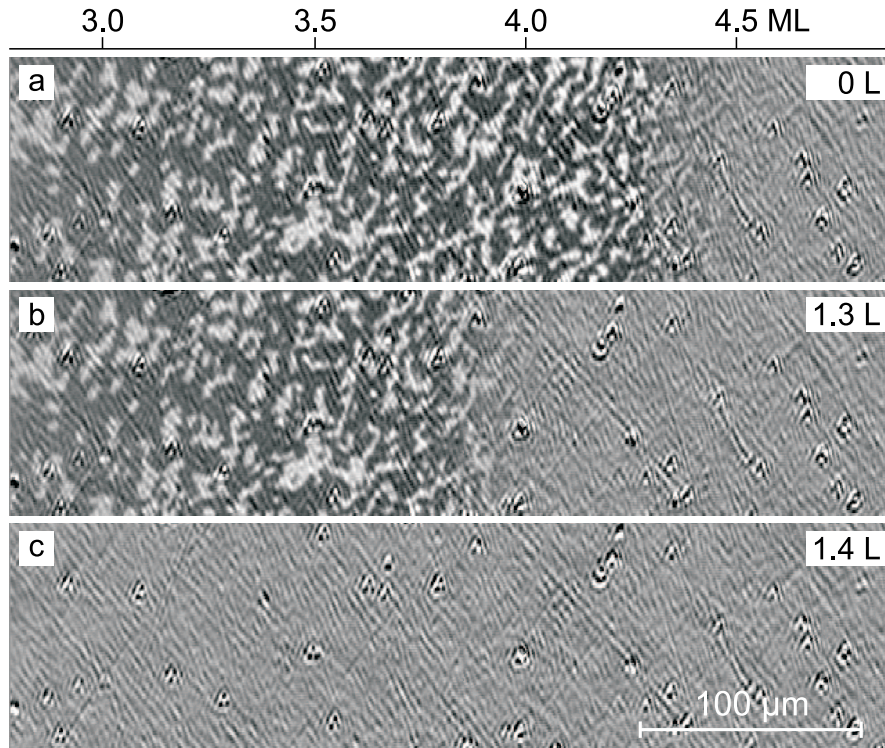


Figure 5.1: Reorientation of the easy axis of magnetization in a Fe wedge on Cu(100) around the critical thickness of 4.3 ML. **a:** As-grown multidomain state with perpendicular magnetization in the left part of the image. The right part of the image shows no magnetic contrasts, here M lies within the film plane. **b:** After exposure to 1.3 L O_2 t_{crit} starts to shift towards lower film thickness. **c:** After further adsorption of 0.1 L the contrast representing perpendicular magnetization has disappeared. The magnetization is now within the film plane.

out-of-plane magnetization can be seen as dark/bright contrast. The domain size depends sensitively on the background pressure during the deposition (in this experiment $2.9 \cdot 10^{-10}$ mbar) and on the temperature.

After LT growth the domain state is not in the energy minimum and can be considered as frozen in a metastable state. Domains start to merge and form a single domain state at RT except in the vicinity of t_{crit} (Fig. 4.8 in Chap. 4).

For thicknesses above 4.3 ML, in the right part of the image in Fig. 5.1 no domain structure is visible. As can be shown by MOKE here the magnetization is within the film plane. In Kerr microscopy no in-plane domains are visible due to the reduced sensitivity of the Kerr microscope in longitudinal geometry. It is evident from Fig. 5.1a that the ROT does not appear sharply at the critical thickness. Rather, a gradual decay of the magnetic contrast of the perpendicular domain configuration over a thickness range of 0.15 ML is observed. Immediately after taking the image the Fe film was exposed to a partial pressure of $2 \cdot 10^{-8}$ mbar. A shift of the critical thickness occurs during the

oxygen adsorption at 140 K. The ROT starts to move towards smaller thicknesses after dosage of 1.3 L O₂ (Fig. 5.1b). After 1.4 L O₂, any perpendicular magnetic contrast has completely disappeared at all thicknesses (Fig. 5.1c). Checking the whole film by Kerr microscopy and MOKE reveals that the perpendicular magnetization has disappeared at all thicknesses after 1.4 L O₂ and the easy axis is now within the plane. A comparison of Fig. 5.1a and b shows that O₂ does not alter the shape or size of the domains at all. Rather, with increasing O₂-coverage the perpendicular magnetization decays at t_{crit} , thus shifting t_{crit} towards smaller thickness and forming a film with in-plane anisotropy. A minimum exposure of O₂ of 1.2 L is necessary to initiate the reorientation. We did not observe an onset of the switching simultaneously with the beginning of the adsorption process. Rather, after a critical coverage of 1.3 L the film reorients very rapidly over the whole thickness.

Two possibilities would explain the observed loss of the perpendicular magnetic contrast after 1.4 L oxygen exposure: on the one hand, the iron film starts to oxidize and creates non-ferromagnetic layers. This for example was observed in [131, 132] for high doses of O₂. On the other hand, the magnetization reorients in the plane and no contrast is visible in our Kerr microscope due to the reduced sensitivity in this geometry. To check which case applies here, subsequent MOKE experiments were performed on the film. Figure 5.2 shows the remanent polar (■) and longitudinal MOKE signal (●) before oxygen adsorption as a function of Fe thickness. The observed linear increase of the polar signal with increasing film thickness, followed by a complete drop to zero at $t_{crit} = 4.3$ ML, is well known for LT grown Fe [102]. For films thicker than t_{crit} only a remanent longitudinal MOKE signal can be measured. After exposing this Fe-wedge to 1.4 L of O₂ the remanent polar MOKE signal has completely vanished. Instead, a remanent longitudinal MOKE signal could be measured for a Fe thickness above 2 ML (○). The magnitude of this signal almost precisely overlaps with the longitudinal signal observed prior to oxygen exposure proving that the magnetic moment of the film has not significantly reduced due to oxygen treatment.

The formation of a thorough layer of non-ferromagnetic FeO or Fe₂O₃ can therefore be excluded. This experiment clearly shows an oxygen-induced reorientation of the easy axis of magnetization from perpendicular to in-plane in the thickness range between 2 ML and 4.3 ML. The inset in Fig. 5.2 shows the corresponding hysteresis loops for out-of-plane (i) and in-plane (ii) magnetization prior to O₂ exposure at a thickness of 4.1 ML Fe. The in-plane loop after O₂ treatment (iii) at the same thickness is shown in the second inset. Below 2 ML no remanent magnetic signal was detected after O₂ exposure. One might speculate whether this rough seed layer mostly consisting of double

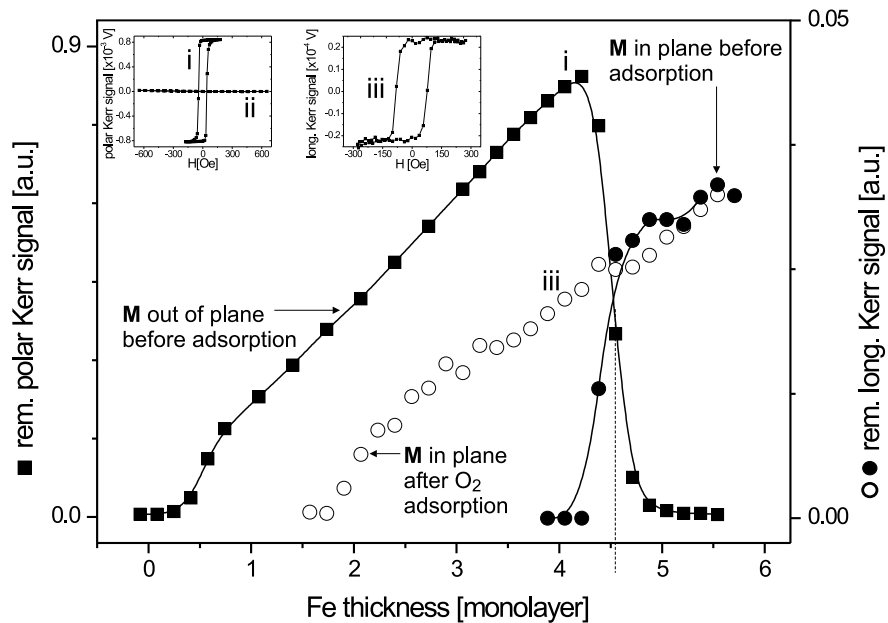


Figure 5.2: MOKE on a Fe wedge grown on Cu(100) at 140 K. The drop of the remanent perpendicular signal prior to adsorption (■) is observed at the critical thickness of $t_{crit} = 4.3$ ML. The remanent in-plane Kerr signal after O₂ exposure (○) matches the in-plane signal prior to exposure (●) for $t_{Fe} > 4.3$ ML within the experimental error. Hysteresis loops before (i), (ii) and after O₂ adsorption (iii) are shown in the inset.

layer islands is more susceptible to oxide formation since coalescence of the islands is not yet finished and a closed layer not yet formed. Also, the Curie temperature of this film might be reduced due to oxygen adsorption.

Oxygen adsorption on annealed LT grown films

As was discussed in Chap. 4, the morphology of the LT grown films changes upon annealing to RT. The behavior of the magnetism of such thermally modified films during oxygen adsorption is discussed in the following. Fe films have been grown at 130 K and subsequently annealed to RT. In Fig. 5.3 the thickness dependent remanent polar (■) and longitudinal (○) MOKE signal of the film during different stages of the experiment is shown. The iron wedge with a maximum thickness of 5.2 ML shows in-plane magnetization (phase A) below 4.3 ML and perpendicular magnetization (phase B) above 4.3 ML at low temperatures (Fig. 5.3a). After annealing to RT the critical thickness is shifted by 1 ML towards lower thickness (Fig. 5.3b). The drop of the remanence for thicknesses below 1.5 ML is possible due to the Curie temperature of this film of less than 300 K [105]. The shift of the ROT from 4.3 to 3.3 ML is thermally induced and will be investigated and described in detail in Chap. 6.

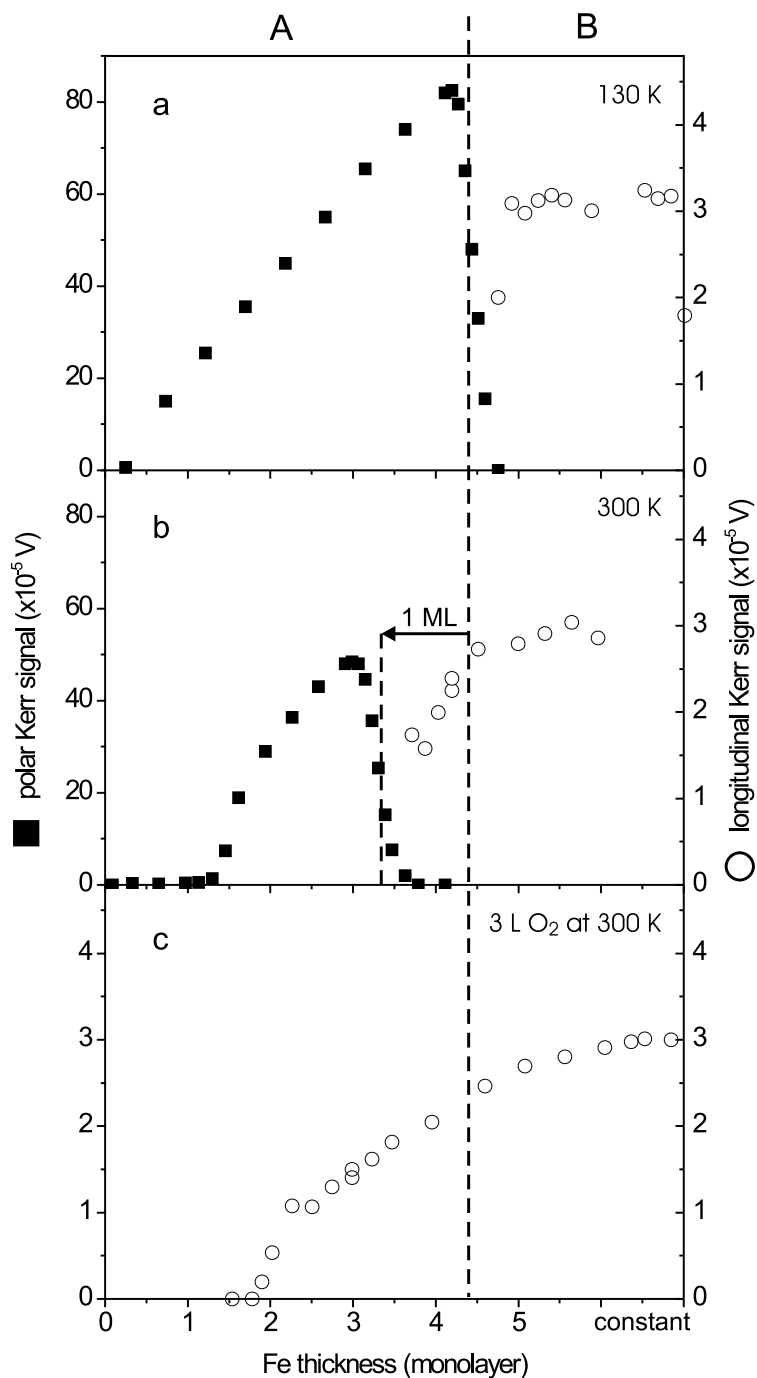


Figure 5.3: Thickness dependence of the remanent Kerr ellipticity of a Fe wedge. **a:** Remanent magnetization for the Fe film deposited at 130 K. **b:** Thermally induced shift of the ROT after annealing to 300 K. **c:** Complete reorientation of magnetization into the plane after adsorption of 3 L O₂ at RT.

The longitudinal Kerr signal of the film above 4.3 ML has the same magnitude before and after annealing. Also the polar Kerr amplitude in a thickness range between 1.5 ML and 3.3 ML remains unchanged after annealing. The exposure of the annealed film to 3 L O₂ switches the perpendicular magnetization of the film into the film plane (Fig. 5.3c). The comparison of the in-plane signals in Fig. 5.3a with c shows no loss of the longitudinal Kerr signal after exposure to 3 L. The main difference to LT grown films without annealing is that twice as high oxygen doses of 3 L instead of 1.5 L are necessary to cause the same reorientation. One possible explanation is that the thermally activated smoothing of the film (see Chap. 6) reduces the number of edge atoms and thus decreases the sticking coefficient. Similar to the LT grown films, the O₂ adsorption causes a complete reorientation of the magnetization into the plane.

Oxygen adsorption on films grown at 300 K

The magnetic and structural properties of RT grown films differ from these of LT grown films and have been described in detail in Chap. 4. In short: here the out-of-plane and in-plane phases are separated by a phase with antiferromagnetic coupling in the thickness range between approximately 4 and 11 ML. Oxygen adsorption on RT grown films can help to understand the role of surface morphology on the adsorption and thus its importance for magnetism. Fe films were grown at 300 K and then cooled to 130 K for magnetic studies. At such low temperatures the available maximum polar field of 600 Oe was not sufficient to overcome the high coercivity of the film and to reverse the magnetization. Therefore the films have to be warmed up to 220 K at which H_c was somewhat decreased and the magnetization could be reversed. The saturation magnetization (\square) and the remanent magnetization (\blacksquare) of a RT grown Fe wedge with $t_{max} = 7$ ML at 220 K are shown in Fig. 5.4. The transition from phase I to phase II is recognized by a sudden drop of the polar magnetization to a constant thickness-independent value at about 4 ML. T_c is a function of the film thickness [105]. The absence of a remanent signal in region II can be understood when a reduced Curie temperature of the FM layers is taken into account.

Also a splitting up of the magnetization into very small domains in zero field can explain the absence of remanence in this thickness range. A resulting polar magnetic moment can only be achieved by applying a polar external field. On the other hand no in-plane magnetization was observed in this thickness range. The observation agrees with the known fact that only the topmost monolayer (roughly 2 ML [156]) are coupled ferromagnetically with polar anisotropy, although in our experiments a resulting moment could only be achieved by applying a field.

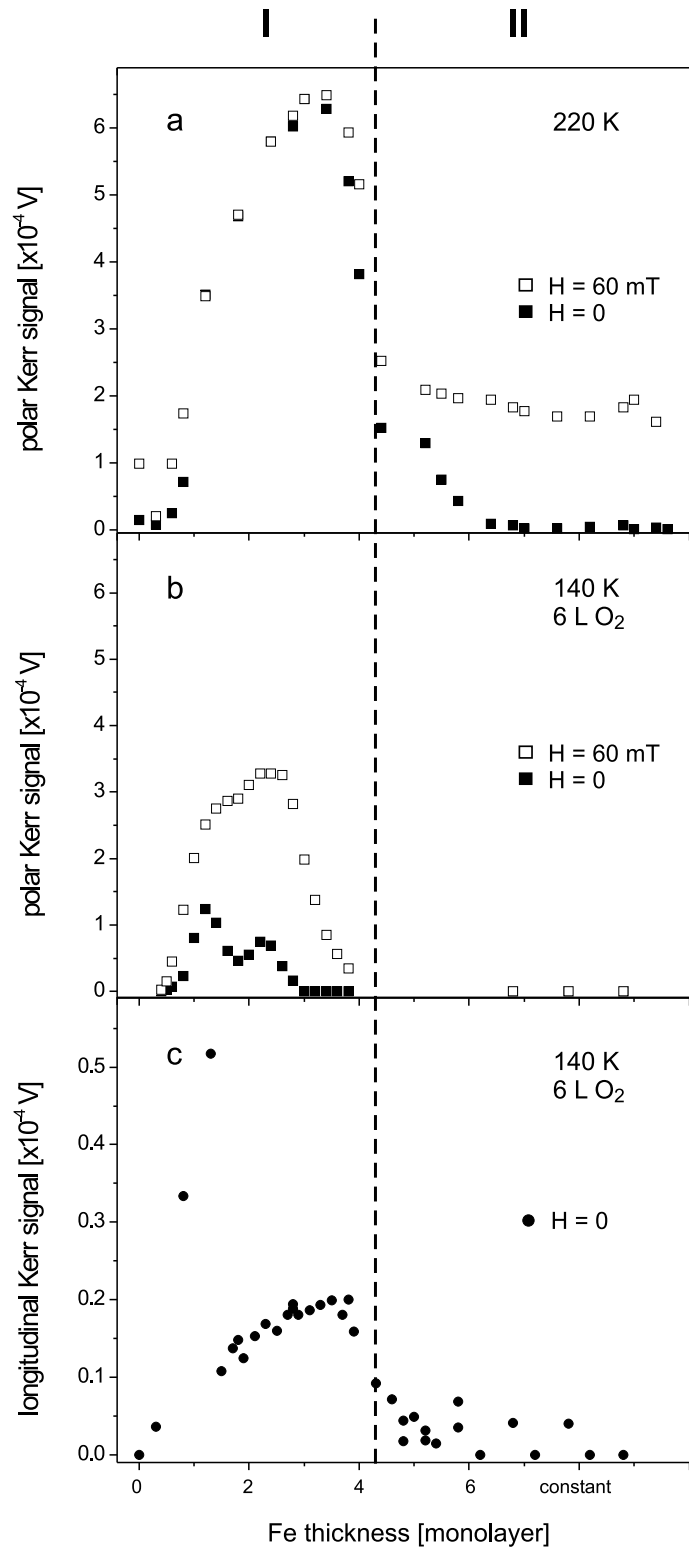


Figure 5.4: MOKE on a Fe wedge grown at 300 K on Cu(100). **a:** Polar Kerr signal at 220 K prior to adsorption. **b:** Polar and **c:** longitudinal Kerr signal after O_2 adsorption. **c:** After O_2 exposure at 140 K the film has a remanent in-plane magnetization. Below 1.4 ML some out of plane magnetization is still found after adsorption of 6 L O_2 .

In Fig. 5.4b and c the longitudinal and polar Kerr signals after exposure to 6 L O₂ at 140 K are shown. In analogy to LT grown films the critical thickness shifts towards smaller thickness with increasing O₂ coverage. Only below 1.4 ML the film shows polar hysteresis curves with some remanence. The curves are s-shaped and therefore the remanent signal deviates from the saturation signal. The remanent longitudinal Kerr signal in Fig. 5.4c clearly proves the switching of the easy axis into the film plane above 1.4 ML. Our MOKE setup is sensitive to the longitudinal and the polar Kerr effect which leads to a crosstalk between both signals. The peak of the longitudinal signal below 1.4 ML in Fig. 5.4c is due to the sensitivity to out-of-plane signals. The angular dependence of the loops and the magnitude of the signals help to distinguish between in-plane and out-of-plane magnetization. In comparison, the critical thickness for the ROT shifts towards smaller Fe thickness in LT and RT grown films due to oxygen adsorption. Also the reorientation does not happen at all thicknesses simultaneously, but rather the ROT does move through the wedge towards smaller thickness with increasing O₂-coverage. While 1.6 L O₂ cause a complete reorientation in Fe at all thicknesses in LT grown films, in RT grown films some remanent magnetization smaller than before the adsorption prevails even after exposure to 6 L O₂. Figure 5.4b shows that the saturation signal of the s-shaped hysteresis loops below 1.4 ML corresponds to the remanence as measured in Fig. 5.4a before the adsorption. After the external field is switched off, this signal decays to a somewhat smaller remanence indicating the presence of a canted magnetization state. The coexistence of in-plane and out-of-plane domains was not observed, neither did we see any change in the domain shape or size.

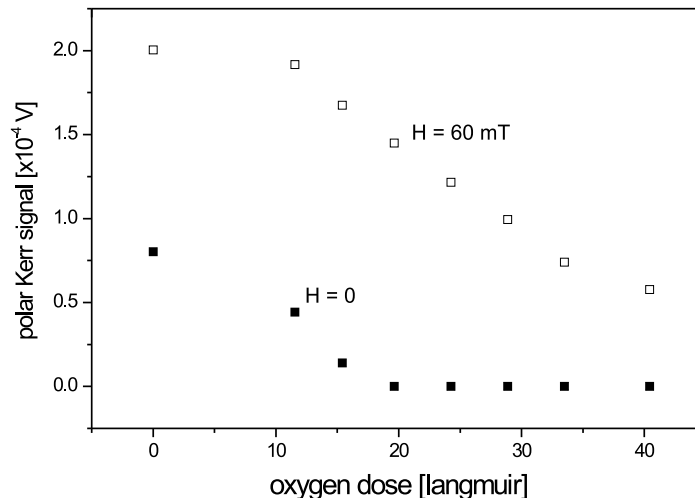


Figure 5.5: MOKE on 1 ML Fe film on Cu(100) at 300 K. The polar Kerr signals in remanence (■) and saturation (□) are taken at RT during oxygen exposure.

The question arises, whether the reorientation below 1.4 ML can be completed by exposing the film to more oxygen. Figure 5.5 shows the decay of the polar remanent and saturation signal of the film at the thickness of 1.4 ML measured during exposing the film to oxygen. The experiment was stopped after 40 L O₂. It was observed that the remanent magnetization disappears after further 20 L O₂, that means 26 L O₂ in total. For even higher doses s-shaped loops without remanence are observed with decreasing saturation. The remanent magnetization gradually decreases to zero after 20 L O₂ and results in the formation of oxide layers, which are non-ferromagnetic.

5.2 Fe thickness selective reorientation during CO adsorption

From the different surface chemistry effects of oxygen and carbon monoxide on metal surfaces one could also expect a different influence to the magnetic properties of metals. In the following we have investigated the influence of CO adsorption on the magnetic anisotropy of iron films. Figure 5.6a shows the Kerr image of a Fe wedge prior to CO adsorption. The wedge-like film with a maximum thickness of 5.3 ML was grown and kept at 132 K. Analogous to the previously described experiments the Kerr image shows the virgin domain state near the critical thickness at 4.3 ML. In the experiment the film was exposed to carbon monoxide at 130 K directly after the LT growth. The critical

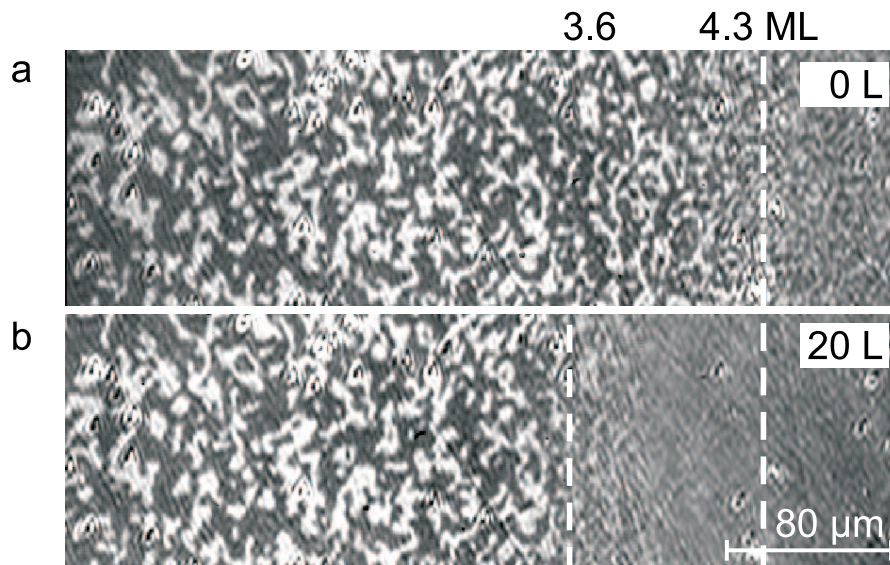


Figure 5.6: Kerr image of the ROT before (a) and after (b) CO adsorption. The ROT shifts to 3.6 ML due to CO. No further shift is observed even if 20 L are applied.



Figure 5.7: Kerr microscope image of Fe films with constant thickness grown at 130 K, shown after CO exposure. **a:** Perpendicular domain state of 3 ML Fe film after dosage of 12 L CO. **b:** Vanishing of the perpendicular domain structure after the same dosage of CO. The film has a thickness of 4.2 ML.

thickness of the ROT is shifted from 4.3 ML to 3.6 ML by adsorption of 4 L of CO. In contrast to oxygen adsorption, films thinner than 3.6 ML remain magnetized perpendicularly, even if the film is exposed to CO doses as high as 20 L (Fig. 5.6b). The film is completely passivated by CO. Subsequent exposure to 50 L O₂ for example gives no further switching of the magnetization from out-of-plane to in-plane as it was observed for the clean Fe/Cu(100) film. Therefore an adsorbate induced thickness selective reorientation is found with CO as adsorbate. A comparison of the results from oxygen and carbon monoxide treatments shows, that adsorbate-induced changes of the ROT depend on the adsorbate itself. That means, the nature of electronic interaction between film and adsorbate seems to play an important role. This result of a thickness dependent effect was confirmed with separate Fe films of constant thickness. In Fig. 5.7 the Kerr image of a 3.0 ML and a 4.2 ML thick film after CO adsorption is shown. Both films with a remanent perpendicular magnetization are exposed to CO. After 12 L CO the 3 ML Fe film in Fig. 5.7a shows still a perpendicular domain configuration. In Fig. 5.7b, the spins are in the film plane at a thickness of 4.2 ML after CO adsorption with the same dose. This means that the wedge shape of the film itself did not influence the result of the experiment.

5.3 Adsorption experiments with NO

To investigate the dependence of the adsorbate-induced reorientation in more detail, different adsorbates with varying electronic interaction with the film have been tested. In analogy to oxygen it is also expected from nitric oxide (NO) to accept electrons from the film after adsorption. The consequences of NO to the magnetic properties of LT grown films is investigated therefore in the following. The starting conditions are similar

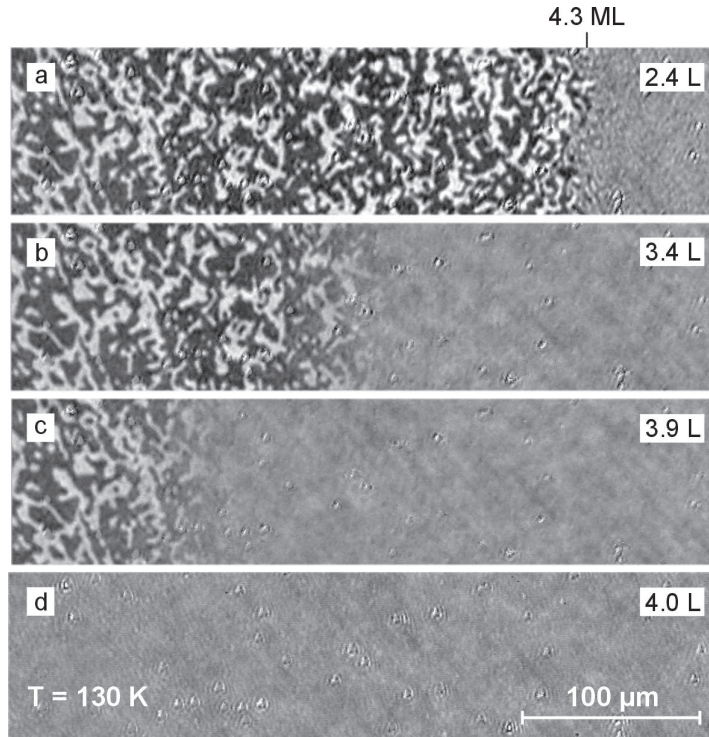


Figure 5.8: Kerr image on a Fe wedge grown at 130 K on Cu(100) for different NO coverage. The film thickness increases from left to right. **a:** For NO adsorption up to 2.4 L the domain configuration remains unchanged. **b, c:** Adsorption of higher NO doses lead to a reorientation of the magnetization into the plane. **d:** Thus the magnetic contrast has disappeared.

to those of the previous LT O₂-adsorption experiments. After the growth of a Fe wedge at 130 K the spin reorientation from out-of-plane to in-plane could be observed at a thickness of $t_{crit} = 4.3$ ML (Fig. 5.8a). Kerr images taken during exposure to NO are shown in Fig. 5.8b to d for several NO coverage. The process of the reorientation of magnetization is comparable to that during oxygen exposure. The perpendicular magnetization of the film starts to switch into the film plane after adsorption of 2.4 L NO. With increasing amount of NO adsorbate the spin reorientation shifts towards smaller film thickness (Fig. 5.8b and c). After 4.0 L NO the magnetization of the entire film lies in the film plane. The in-plane magnetization was checked afterwards with MOKE. Again a gradual decay of the Kerr contrast in the vicinity of t_{crit} is clearly visible. This is observed for all adsorbates investigated so far. To understand the influence of NO adsorption on magnetism, more detailed knowledge about the nature of the interaction with the film is necessary.

The NO adsorption on various metal surfaces was investigated in the past by several research groups. For instance Kerr experiments performed on 1 ML Co/Cu(100) films show an annihilation of the ferromagnetism in these films after adsorption of 7 L NO

at RT [163]. A strong support that oxygen is responsible for the spin transition in our NO adsorption experiments comes from early experiments of Kishi et al. . In combined ultra-violet and x-ray photoelectron spectroscopy experiments the coverage dependence of the N(1s) peak during NO adsorption on iron at 85 K and during annealing to RT indicates a dissociative chemisorption [164]. This might lead to an oxygen dominated electronic interaction with the Fe surface. NO is thermodynamically more instable than CO because of the electron in the antibonding π^* state [165]. On the other hand a free NO molecule has an electronic structure similar to that of CO, but with one extra unpaired electron in its $2\pi^*$ orbital. One would therefore expect a qualitatively similar chemisorption of NO and CO on transition metal surfaces [166,167].

The different influences on the magnetism might arise from possible different adsorption geometries. The electron transfer between CO and surface is found to be much stronger for the “lying down” adsorption of a CO molecule than for the upright attachment of CO to the metal surface [150]. This is due to the C–O bonding which is more exposed to the metal surface in the “lying-down” geometry. The strength of the electronic interaction depends therefore on the adsorption geometry of the molecules. The same was also confirmed in local spin density approximation (LSDA) calculations [168] of the magnetic properties of NO on metal/(100) systems. A quenching of the magnetic moment in Ni was found in the case of bridge site bonding of NO. Different adsorption geometries can therefore explain different changes of the magnetism despite very similar electronic structure of the adsorbates.

In conclusion, our NO experiments show a complete spin reorientation at all thicknesses smaller 4.3 ML, similar to O₂ adsorption experiments. Whether the adsorption geometry or rather dissociation of the NO molecule is responsible for the strong electronic interaction cannot be concluded from our experiments.

Discussion

In our experiments we have investigated the spin reorientation transition in LT grown Fe film due to the influence of the adsorbates O₂, CO and NO. We observed adsorbate-induced shifts of the critical thickness t_{crit} towards smaller film thickness. For O₂ the entire film reorients at all thicknesses from the out-of-plane to in-plane magnetization after exposure to 1.4 L O₂. A quite similar behavior we found for the adsorption of NO. After exposure to 4.0 L NO the entire film exhibits an in-plane magnetic anisotropy. In contrast to that the adsorption of CO causes a thickness dependent spin reorientation effect in iron. Even after doses of 20 L CO, Fe films thinner than 3.6 ML remain in a perpendicular spin configuration.

The results show that adsorbates change the magnetism of ultrathin films. The modified magnetic properties can be caused by structural and electronic changes of the film due to the adsorption of atoms or molecules.

In the literature the tetragonal distortion of the fcc iron to a fct structure with a 5% enhanced interlayer spacing is discussed as the driving force for the perpendicular magnetization via magneto-volume effects [31]. Based on this discussion the question arises whether modified interlayer spacings resulting from adsorbates lead to the observed adsorbate induced effects. A change of layer spacing due to adsorption was not investigated in this work. The possible influence of an adsorbate on the interlayer spacing can be discussed in the following simple model: oxygen is expected to accept electrons from the film, thus causing an electron depletion in the film. This would lead to an increase of the lattice spacing to maintain the balance of electric charges per volume.

In this model one would expect oxygen to stabilize the fct phase. If the enhanced lattice spacing would be the origin of perpendicular magnetization then oxygen adsorption should support this, which is clearly not observed in our experiments. On the other hand, in this picture one would expect from hydrogen to donate its electron partly into the film, thus reducing the interlayer spacing and causing a reorientation of magnetization into the plane. This was also not observed: we did not find any influence of hydrogen adsorption on LT grown films on the magnetism, and the ROT in particular. For RT grown films on the other hand it was found by Vollmer et al. that H₂ adsorption stabilizes the expanded interplanar spacing of the Fe for up to four ML instead of three ML without H₂ [156]. However, this simplified model does not take into account the real nature of the charge transfer between film and adsorbate, that means, which orbitals, bonding or antibonding, are occupied after adsorption, as was pointed out by Feibelman [169].

Although several adsorbates are found to modify the interplanar spacing there is no tendency to support the assumption that enhanced interplanar spacing increases t_{crit} and vice versa. This result indicates that not the interlayer spacing but rather the modification of the electronic structure on the surface itself causes the observed changes of the ROT, supporting the idea of dominant surface anisotropy contributions at low Fe thickness.

The observed adsorbates effects are therefore discussed in the picture of modified surface anisotropy in the following. The influence of the surface anisotropy on the magnetic properties of thin films and ROT in particular was discussed in Chap. 4. The observed thickness selective reorientation upon CO adsorption allows a more detailed analysis of the change in the anisotropy energy and can be used to estimate CO-induced changes on K_{surf} . The perpendicular magnetization in Fe is assumed to be due to the dominating

Property	Value	Ref.
a_{Fe}^{fcc}	3.59 Å	[170]
$d(4 ML)$	1.87 Å	[171]
$\varepsilon_{ }$	1.54 %	
ε_{\perp}	5 %	
$B_1^{eff}(\varepsilon_{ })$	13.5 MJ/m ³	[172]
K_{f-vac}	0.89 mJ/m ²	[173]
K_{f-s}	0.6 mJ/m ²	[174]

Table 5.1: Properties of epitaxial Fe-films on Cu(100).

contribution of the film-vacuum interface to the anisotropy K_{f-vac} . Within this picture the shift of t_{crit} in Fig. 5.6b can be used to estimate the CO induced change of the surface anisotropy K_{f-vac} , using Eq.(4.10) in Chap. 4 and experimental data obtained on this system. All relevant experimental data from the literature, are summarized in Table 5.1.

For the equilibrium lattice constant of fcc Fe different data are found in literature ($a_{Fe}^{fcc} = 3.6468$ Å [175] and $a_{Fe}^{fcc} = 3.59$ Å [170]), leading to in-plane strain of opposite sign ($\varepsilon_{||} = -0.88\%$ vs. $\varepsilon_{||} = +0.69\%$, with $a_{Cu} = 3.6147$ Å [175]). The observation of tensile stress in the Fe film during the growth on Cu(100) [172, 176], supports an expanded lattice constant in the pseudomorphic Fe layer, thus an $\varepsilon_{||} = +0.69\%$ is assumed for the calculation. The perpendicular strain follows from the average interplanar spacing of $d = 1.87$ Å [171] to $\varepsilon_{\perp} = +5\%$. The magneto-elastic coupling B_1 was found to be strain-dependent [172], giving a $B_1^{eff} = 13.5$ MJ/m³ for the pseudomorphic 4 ML Fe. This value differs significantly in magnitude and sign from the respective bulk value, which was used in all previous calculations. Using $M_S = 1751$ kA/m, $K_{f-vac} = 0.89$ mJ/m² [173] and $K_{f-s} = 0.6$ mJ/m² [174] leads to the thickness dependence of ΔF_{tot} as depicted in Fig. 5.9 as a solid line. The critical thickness $t = 4.3$ ML is found from $\Delta f_{tot} = 0$. To reproduce the shift of t_{crit} by 0.7 ML due to CO in Fig. 5.6b, a changed $K_{f-vac} = 0.63$ mJ/m² has to be assumed giving the thickness dependence of f_{tot} shown as a dashed line in Fig. 5.9. The K_{f-s} remains unchanged.

The oxygen induced reorientation in the LT experiment (Fig. 5.1) can only be explained by a change in sign of K_{f-vac} with $K_{f-vac} + K_{f-s} \leq 0$. It is worth to note that despite the large B_1^{eff} the magneto-elastic contribution is not sufficient to compete with the surface anisotropy and thus to alter the easy axis. The CO induced reorientation of M can therefore be understood by assuming a modified surface contribution to the anisotropy. The comparison between the adsorbates O₂, CO and NO leads to the assumption that

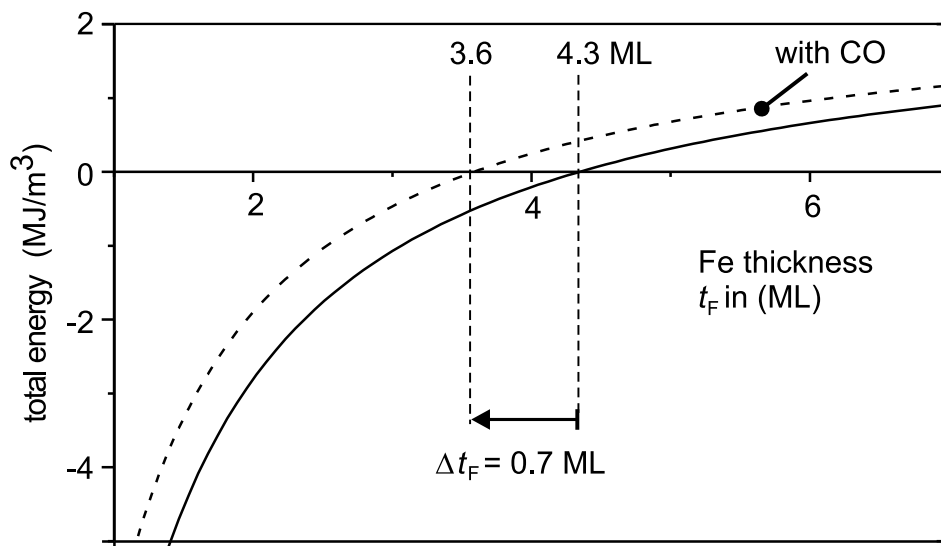


Figure 5.9: The difference of the total energy of the film between perpendicular and in-plane magnetization as a function of thickness (straight line). The change in sign at 4.3 ML marks the critical thickness for reorientation. The CO induced shift can be reproduced with $K_{f-vac} = 0.63 \text{ mJ/m}^2$ (dashed line).

their influence on the magnetism is related to the strength of the electronic adsorbate-film interaction. Various experimental results can be found which support this assumption. For instance the electronic structure of the LT grown Fe/Ag(100) interface was investigated with spin polarized metastable de-excitation spectroscopy (SPMDS) experiments [131,142]. It was found that the d-band splitting of iron is unchanged below a coverage of O_2 1.2 L. With increasing O_2 -coverage the spin polarization of Fe near E_F decreases gradually. A charge transfer from the iron to oxygen leaving behind Fe states with majority character was suggested. On the other hand, for coverage below 1.6 L the O_{2p} states are spin polarized and show ferromagnetic coupling with the Fe. This strong electronic interaction between O and Fe presumably bears the origin of the complete reorientation of magnetization for low O_2 -coverage.

For higher doses of oxygen it was found that O_2 starts to penetrate into the Fe film and forms oxides. Further exposures above 3 L O_2 leads to magnetically dead layers in agreement with our observations. The strong electronic interaction between oxygen and Fe with consequences to the magnetism is shown by the adsorption [128]. A switching of the easy axes after only 0.5 L oxygen was observed in agreement with our results. From the high sensitivity of the anisotropy to oxygen it was therefore concluded that the Fe-vacuum interface makes significant contributions to the total anisotropy of Fe/Cu(100). The much weaker effect of CO can be explained by the adsorption geometry [150],

which was described in Chap. 4. In the upright geometry the electron transfer between adsorbate and surface in this model is weaker due to the separation of the C–O bonding and the film. The electronic interaction is expected to be stronger if the CO molecule adsorbs in a “lying down”-like geometry, where the C–O bonding is more exposed to Fe. Indeed the upright bonding of CO was found on fcc iron, in contrast to the “lying down” geometry found on bcc iron [148]. The influence of the adsorption geometries of CO on Fe and therefore a weaker electronic interaction on fcc surface agrees with our results of a thickness-dependent spin reorientation on the fcc iron between 3.6 and 4.3 ML.

Spišak et al. predicted profound modifications of the electronic and magnetic properties of γ -Fe/Cu(100) due to chemisorbed CO by using first principles local density calculations [153]. Such ab-initio calculations are desirable for a more detailed understanding of the electronic interaction.

In conclusion: the change in the magnetic anisotropy of Fe/Cu(100) upon gas adsorption can be explained by the common picture of competing contributions to the anisotropy, namely magneto-static and surface contributions. The adsorbates alter the surface anisotropy contribution due to the electronic interaction with the film surface. The extent of the magnetic changes depends on the adsorbate itself and on the adsorption geometry.

Chapter 6

Temperature-dependent magnetic properties of Fe/Cu(100)

After the discussion of the sensitivity of Fe films to modifications of the surface electronic structure by adsorbates, in this chapter the dependence of the magnetism on morphology changes is studied. It will be shown that the magnetic properties alter during increasing the film temperature from the growth temperature of 130 K up to 300 K. The critical thickness for the spin reorientation transition sensitively depends on the annealing temperature and shows partly reversible and irreversible changes. The Barkhausen volume as the fundamental unit in the magnetization process is derived from magnetic viscosity measurements, performed with Kerr microscopy and MOKE at various temperatures.

6.1 Thermally induced spin reorientation

An indication that annealing effects the spin reorientation transition, could be seen during the adsorption experiments at different temperatures (Fig. 5.3b in Chap. 5). It was shown that annealing the film to $T_a = 300$ K shifts the ROT by about 1 ML towards smaller thicknesses. In the following it will be shown that the thermal treatment of the film can change the spin reorientation transition reversibly [128] as well as irreversibly. Reversible changes may arise from a pure temperature dependence of the anisotropy constants and will vanish after subsequent cooling of the film back down to the starting temperature. In contrast to that, thermally activated irreversible changes of the magnetism due to diffusion or changes of the film structure and morphology will remain. We performed simple experiments on LT grown Fe wedges to separate temperature-dependent reversible and irreversible changes in t_{crit} due to annealing, using the Kerr

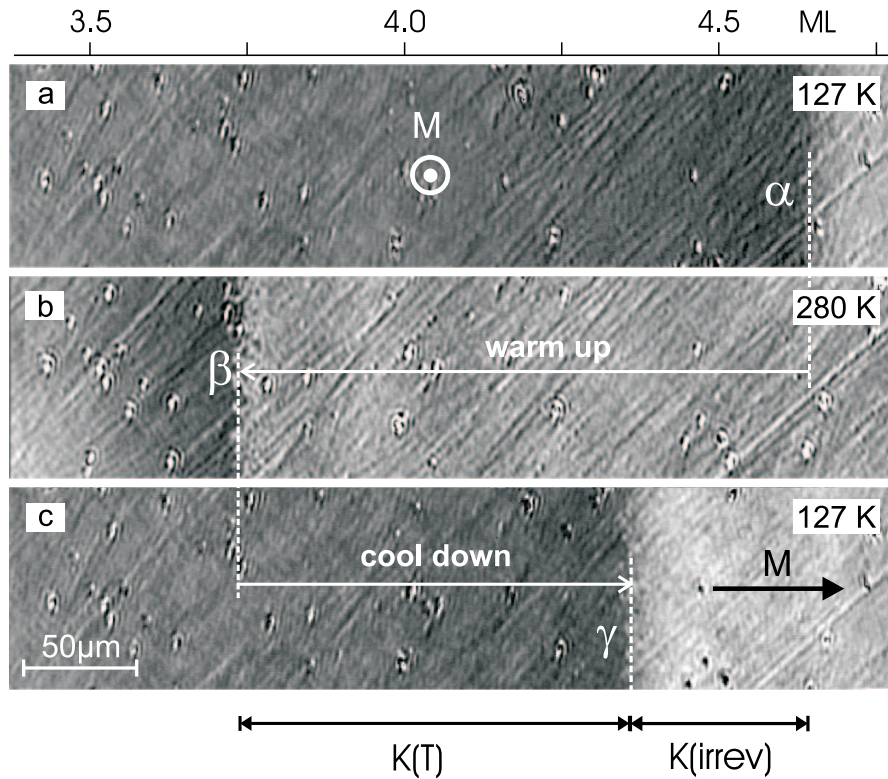


Figure 6.1: Thermally induced shift of the reorientation transition. **a–c:** t_{crit} changes from α to β when raising the temperature from 127 K to 280 K. Cooling back down to 127 K shifts the ROT to $\gamma \neq \alpha$.

microscope. The remanent polar single domain magnetization of a Fe wedge after a magnetic field was applied is shown in Fig. 6.1a. The change in brightness at the crossover from perpendicular magnetization (dark area) to in-plane magnetization (bright area) marks the critical thickness $\alpha = 4.7$ ML of this wedge at the temperature of 127 K, after already having been warmed up to 270 K and cooled back. Annealing of this film to $T_a = 280$ K shifts the critical thickness towards smaller Fe thickness $\beta = 3.7$ ML in Fig. 6.1b. Subsequent cooling of the sample back to 127 K, followed by remagnetization in $H_{\perp} = 250$ Oe brings t_{crit} back to higher film thickness $\gamma = 4.4$ ML, but the critical thickness as in Fig. 6.1a can not be attained again. Instead, repeating the experiment and changing T between 127 K and 280 K reversibly shifts t_{crit} between β and γ .

The dependence of the ROT on the annealing temperature in the temperature range between 100 K and RT is being studied in more detail. Figure 6.2 shows the critical thickness of an Fe wedge as a function of annealing temperature, taken in the same way as described before. Starting at a film temperature of 127 K the film is warmed up to T_a and after that is subsequently cooled down to 127 K. This temperature cycling was repeated several times. During each cycle the annealing temperature was increased

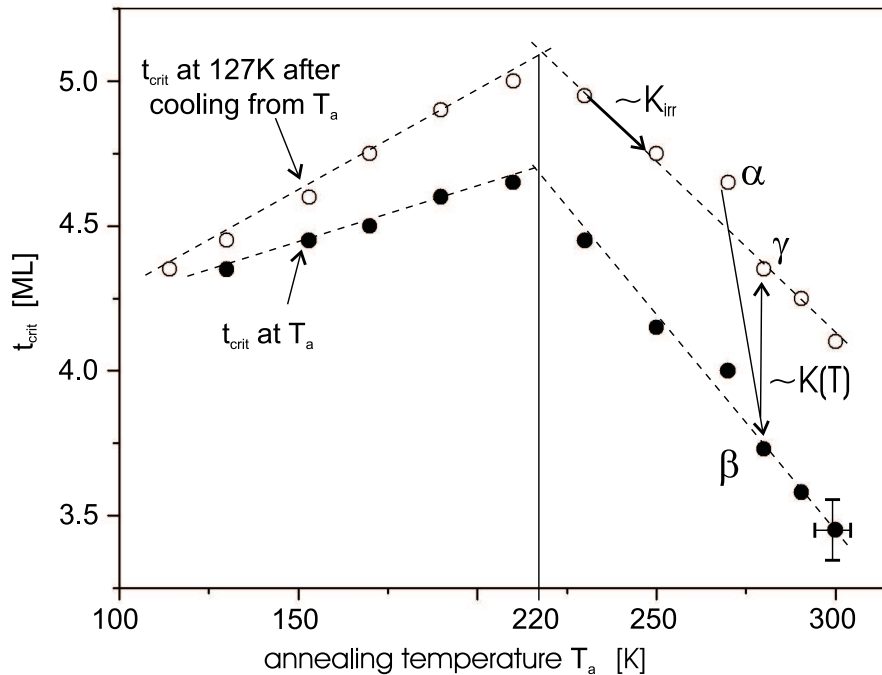


Figure 6.2: Shift of the reorientation transition after cycling of the temperature. Gradual increase of the annealing temperature up to 300 K of at LT grown Fe film. t_{crit} changes from α to β when raising the temperature from 127 K to T_a . Cooling back down to 127 K shifts the ROT to $\gamma \neq \alpha$.

gradually until RT is reached. After annealing at T_a and cooling back to 127 K the film is remagnetized each time in an external field H_{\perp} and the critical thickness is obtained from the Kerr image. Thus, the t_{crit} represented by solid circles (\bullet) in Fig. 6.2 are measured with the film being warmed up to the respective annealing temperature T_a . At the same temperature t_{crit} is plotted as hollow circles (\circ), measured after the film was cooled back from T_a down to 127 K. Therefore, these data are always taken under identical experimental conditions, that means, at the same temperature. The dependence of t_{crit} as represented by hollow circles is therefore due to irreversible changes, while the difference between hollow and solid symbols, plotted at the same T_a , reflects reversible changes. We found in the whole temperature range, that the critical thickness could not be attained again if the sample was annealed to T_a and thereafter cooled back to 127 K. In contrast to that the shift of the critical thickness during cooling from T_a down to 127 K is found to be reversible for all $T_a \leq 300$ K.

Both sets of data in Fig. 6.2, taken at 127 K (\circ) and at T_a (\bullet), show a similar temperature-dependence: Below $T_a = 220$ K the ROT shifts linear with the temperature towards larger film thicknesses by 0.7 ML. The dependence changes abruptly at an annealing temperature of 220 K, where a kink in the curve appears. Further an-

nealing above 220 K leads to a linear shift of the critical thickness in opposite direction towards smaller film thickness. We argue, that the difference between t_{crit} in Fig. 6.1a and c, or more generally, between each data point represented by (\circ) in Fig. 6.2 reflects irreversible changes of the film structure due to the annealing.

Within the anisotropy model introduced in Chap. 4 the temperature-dependence of the critical thickness of spin reorientation could be caused by temperature dependence of the anisotropy constants K_4 , B_1 and K_{surf} . In the chosen symmetry the K_4 does not contribute to an anisotropy between in-plane and out-of-plane magnetization, according to Eq.(4.10). Therefore only the latter two contributions remain. The temperature dependence of the magneto-elastic coupling constants was investigated for bulk Fe [177]. It shows only a negligible dependence on the temperature in the range below 300 K. The observed shift of t_{crit} can therefore not be due to a changed B_1 either. Obviously, the surface anisotropy K_{surf} depends itself sensitively on the temperature, partly reversible and partly irreversible. Inspired by our experimental observations we suggest to split the surface anisotropy in two contributions:

$$K_{surf} = K(T) + K_{irr} \quad (6.1)$$

As was discussed, the shift of t_{crit} during cooling back from annealing temperature (Fig. 6.2b and c) is fully reversible. The full temperature dependence in the temperature range below 300 K can thus be obtained by calculating the difference between the two curves in Fig. 6.2. The result is shown in Fig. 6.3. With increasing annealing temperature the difference Δt_{crit} increases almost linearly and is proportional to $\Delta t_{crit} \sim 4 \cdot 10^{-3} ML/K \cdot T_a$. This corresponds to a change in the surface anisotropy by $1.37 \mu\text{J}/\text{K}$.

Irreversible changes of t_{crit} are due to thermally activated changes of the film structure or morphology. Probably two different competing processes with opposite effect on t_{crit} happen at different temperatures and cause the non-monotonous dependence of the t_{crit} . The influence of film roughness on the magnetic anisotropy was studied by Bruno et al. [11]. A decrease of the film roughness is expected to increase the surface anisotropy, thus shifting t_{crit} towards higher thickness, as observed in our experiments below 220 K. The observed decrease of t_{crit} for $T_a > 220$ K cannot be explained by a surface smoothing. The dependence of the film structure on annealing was investigated with VT-STM. Figure 6.4 shows STM images of a 4 ML Fe film grown at 130 K, after being warmed up to different temperatures. The STM images are taken at the indicated temperature T_a . The image in Fig. 6.4a shows the film at 165 K. A rather rough surface consisting of very small three dimensional islands with a high island density can be seen.

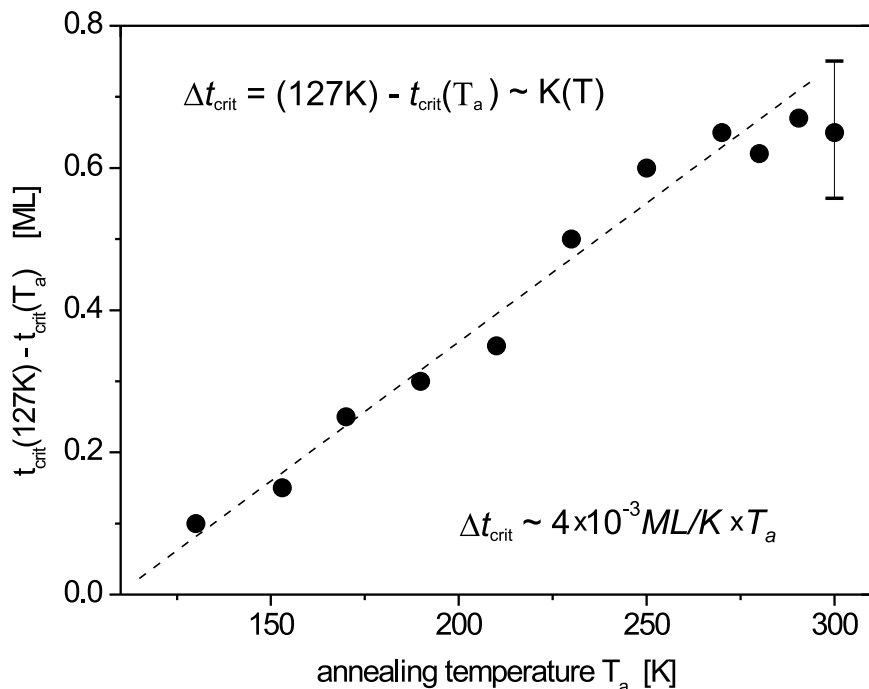


Figure 6.3: Reversible temperature dependent change of the critical thickness.

Further annealing to 215 K changes the film morphology considerably. A significant increase of the island size is observed, whereas the island density decreases. The island size grows continuously up to an annealing temperature of 238 K. At this temperature the film consists of islands with a diameter of 25–30 Å. Further warming to RT leads to no further visible changes of the structure. The film shows similar morphology and island size as observed at 238 K. In a different work a significant flattening of the surface is only observed, if the film is annealed above 350 K [111].

It is tempting to correlate the increase of the island size in the temperature range below 240 K with the observed increase in the critical thickness. In this picture the temperature driven change of the film morphology causes the extension of the perpendicular magnetization to higher film thickness. Our STM investigation, though, cannot explain the decrease of the critical thickness above $T_a > 220$ K. The inner structure of the islands is probably more complex and can only be resolved in high resolution STM experiments. One might speculate, whether the bcc crystallites found in STM studies [178] on RT grown films make the film more bcc like and causes a switch of the easy axis into the film plane. This idea might be supported by recent results showing drastic changes of the morphology of a RT grown fcc-Fe film on Cu(100) after cooling and subsequent warming up to 300 K, which are ascribed to a transition of the film from fcc to bcc structure [108]. Cycling the temperature was indeed found to increase the bcc needle size noticeably in Fe films grown at 300 K [179]. The film structure therefore seems to

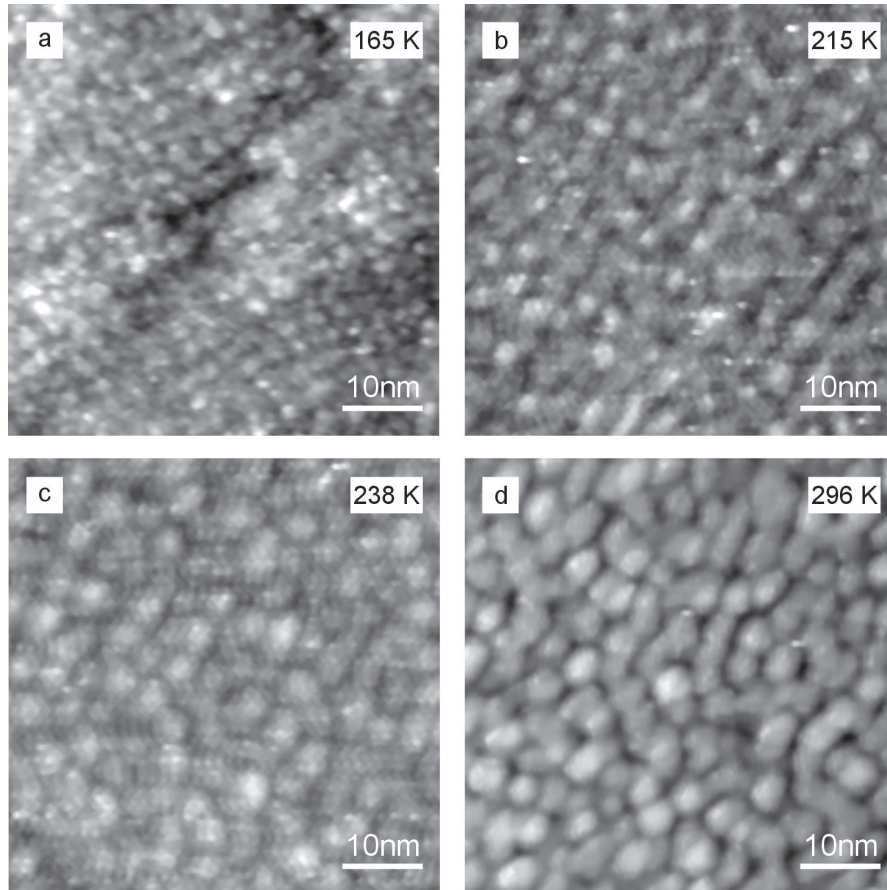


Figure 6.4: VT-STM images of a 4 ML Fe/Cu(100) deposited at 130 K. The images are taken at the indicated temperatures.

depend sensitively on the film temperature already in a temperature range below RT. On the other hand, one also has to take into account temperature-activated diffusion between film and substrate, Fe and Cu, as this is known to alter the magnetic anisotropy energy [32]. It is interesting to note, that other authors [111,119] find a reorientation from in-plane to perpendicular for LT grown 4 and 6 ML Fe on Cu(100) after annealing above $T_a > 350$ K, accompanied by a surface smoothing. Although such high temperatures were not investigated in this work, it contradicts the shift of t_{crit} towards smaller film thickness as observed in Fig .6.1b, as well as to results from RT annealed films in [128] and images in [108].

The smoothing of the film accompanied by a shift of the critical thickness during annealing process underlines the strong correlation between film structure and magnetism. Evidently, the surface anisotropy K_{surf} of the film can be influenced by temperature and structure.

6.2 Magnetic after-effect and the Barkhausen volume

The Barkhausen volume is a fundamental quantity during the magnetization reversal process. It describes the smallest volume which reverses its magnetization as an entity. The size of the Barkhausen volume is determined by the potential energy surface within the film $E(r)$. The temperature dependence of the Barkhausen volume was investigated to get more information about the correlation between structural changes and the potential surface in Fe/Cu(100) during annealing.

The interaction potential $E(r)$ has a complicated structure and is determined on irregularities of the crystal lattice caused by volume effects, surface tension, strain and lattice dislocations. The domain walls are trapped in the local energy minima for some time, until thermal fluctuations help to overcome the energy barriers which separate adjacent local minima. In an applied field H the domain walls will be moved out of their equilibrium position and jump into a new equilibrium state. The irreversible jump of the domain wall is called Barkhausen jump [81] and represents a characteristic mean volume of a magnetic reversal. After the field is switched off ($H = 0$) the domain wall cannot return into their initial position and rests in the new state. The irreversible jump modifies accordingly the magnetization and causes magnetic hysteresis. The deviation of the free energy $\frac{dE}{dr}$ is proportional to the coercivity H_c . The velocity of the relaxation process depends on the energy landscape, which includes the distribution of energy minima and energy barriers and the temperature.

The Barkhausen volume is studied by measuring the magnetic viscosity of the film (also known as magnetic after-effect [180]). In this experiment the time and temperature dependent change of \vec{M} is measured after a constant field $H < H_c$ is applied. The magnetic after-effect is the result of the time-dependent approach of the system to thermodynamic equilibrium within external field at a certain temperature. At the equilibrium the system is in the minimum of the free energy. The magnetic domain size changes by freely moveable domain walls to achieve this minimum of free energy. Thermal relaxation has two main consequences: one is that the shape of a hysteresis becomes dependent on the sweep rate of the external field, because the rate modifies the time spent by the system in front of a certain energy barrier and consequently modifies the probability that the barrier may be overcome by thermal fluctuations. The other is that the magnetization changes in time, even if the field kept constant.

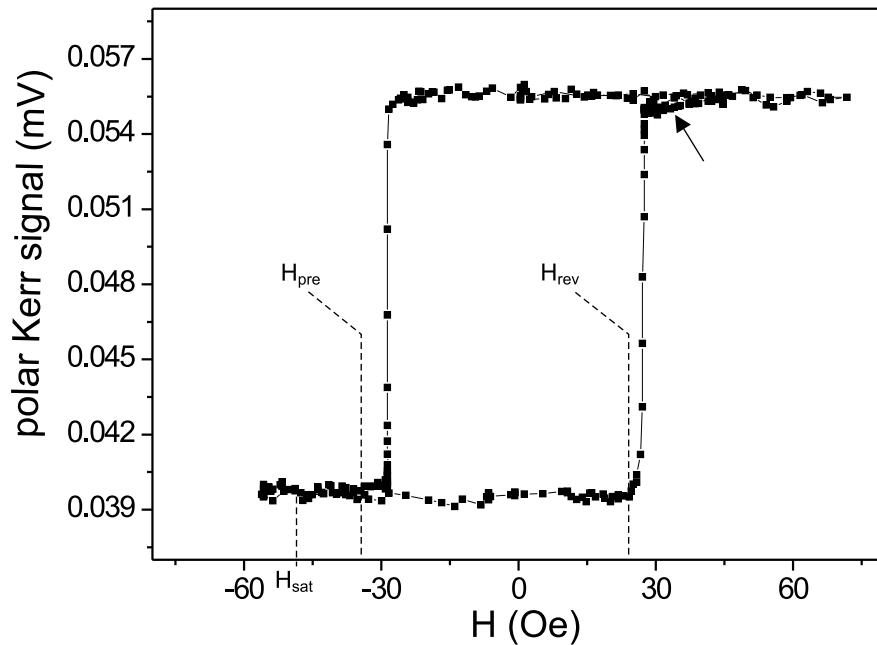


Figure 6.5: Polar MOKE hysteresis loop for 3 ML Fe/Cu(100) at 150 K with coercive field of $H_c = 28.7$ Oe.

A typical square like hysteresis loop as taken on 3 ML Fe/Cu(100) with perpendicular anisotropy at 150 K is shown in Fig. 6.5. At the coercive field H_c the magnetization reaches a value close to the saturation magnetization, as is indicated by the arrow. To saturate the film completely, an external field twice as large as H_c has to be applied. This means that at H_c the magnetization does not completely reverse, rather some small domains with opposite magnetization are still found in the film at H_c . This is due to the fact that the domain wall motion is blocked when the domain walls of opposite magnetization meet. It costs extra field energy to squeeze out the domain walls and to form the single domain state. This was found out by observing the magnetization reversal process with the Kerr microscope.

The magnetic viscosity of the film is determined in the following: The film is pre-magnetized by an external field H_{pre} with $H_c < H_{pre} < H_{sat}$ to create a full magnetized state with nucleated domains of opposite magnetization inside. The field is applied perpendicular to the film plane. The time-dependent change of the magnetization is observed with MOKE or Kerr microscopy. At time $t = 0$ a reversal field $H_{rev} < H_c$ is applied. The field reversal is kept constant during the measurement. It is important to note, that the pre-magnetization field H_{pre} has to be smaller than H_{sat} .

If the film was pre-magnetized in a field $H_{pre} > H_{sat}$, no viscosity measurement were possible. The higher field necessary to create domains of opposite magnetization was considerably larger than H_c and thus the magnetization reversed instantaneously and

without viscosity after domain nucleation has happened. Similar observations were also made in MOKE measurements in thin Ni/Cu(100) films [119]. Therefore, the film was not completely saturated by using smaller pre-magnetization fields $H_{pre} < H_{sat}$, therefore small nucleation centers with reversed magnetization remained. If now a field $H_{rev} < H_{sat}$ is applied, the time-dependent magnetization reversal due to domain wall motion at this temperatures is measured. From this the Barkhausen volume can be derived.

As mentioned earlier, the magnetization reversal process is determined by domain nucleation and domain growth. The interpretation of the dynamical after-effect requires a direct microscopic observation of the development of the magnetic domain structure at a constant magnetic field [181]. Figure 6.6 shows the time evolution of the magnetic domain structure. The 3 ML film is grown at LT and imaged with the Kerr microscope at 143 K. Before starting the measurement, the film was pre-magnetized with a field of $H_{pre} = 34.2$ Oe, smaller than H_{sat} . The image taken after pre-magnetization in a field $H = 0$ contains some nucleated domains with reversed magnetization, and is subtracted as a reference image from all following images to improve the image quality. After applying the field of $H_{rev} = 13.1$ Oe at $t = 0$, the existing domains start to increase their size. Fine lines are visible in the black domains as a result of subtracting the reference image containing already nucleated domains. Basically, a particular domain pattern can be associated to any point of experimental relaxation curves taken by MOKE in Fig. 6.7. The first image in Fig. 6.6 is taken at $t = 0.15$ s, after the external field was applied. The location of the nucleation sites seen in the image is arbitrary. With increasing time the widening of the nuclei by domain wall displacement is visible. The domain walls propagate in-plane along the $\{110\}$ directions. No further nucleation is observed. That means the magnetic after-effect in this films is exclusively controlled by domain wall displacement and not by nucleation processes. Finally the domains partly coalesce and after 45 seconds about 96% of the sample surface is magnetically reversed. The coalescence of the domains seems to require higher fields than necessary to propagate the domain walls itself. From the image in Fig. 6.6 it appears that at such places (marked with an arrow), where domain fronts with opposite propagation direction meet, the formation of a single domain requires considerably higher external fields. Thus, a few gaps with opposite magnetization remain, even after very long times are elapsed. The single domain state cannot be reached within the experiment. It can only be achieved by applying a higher external field.

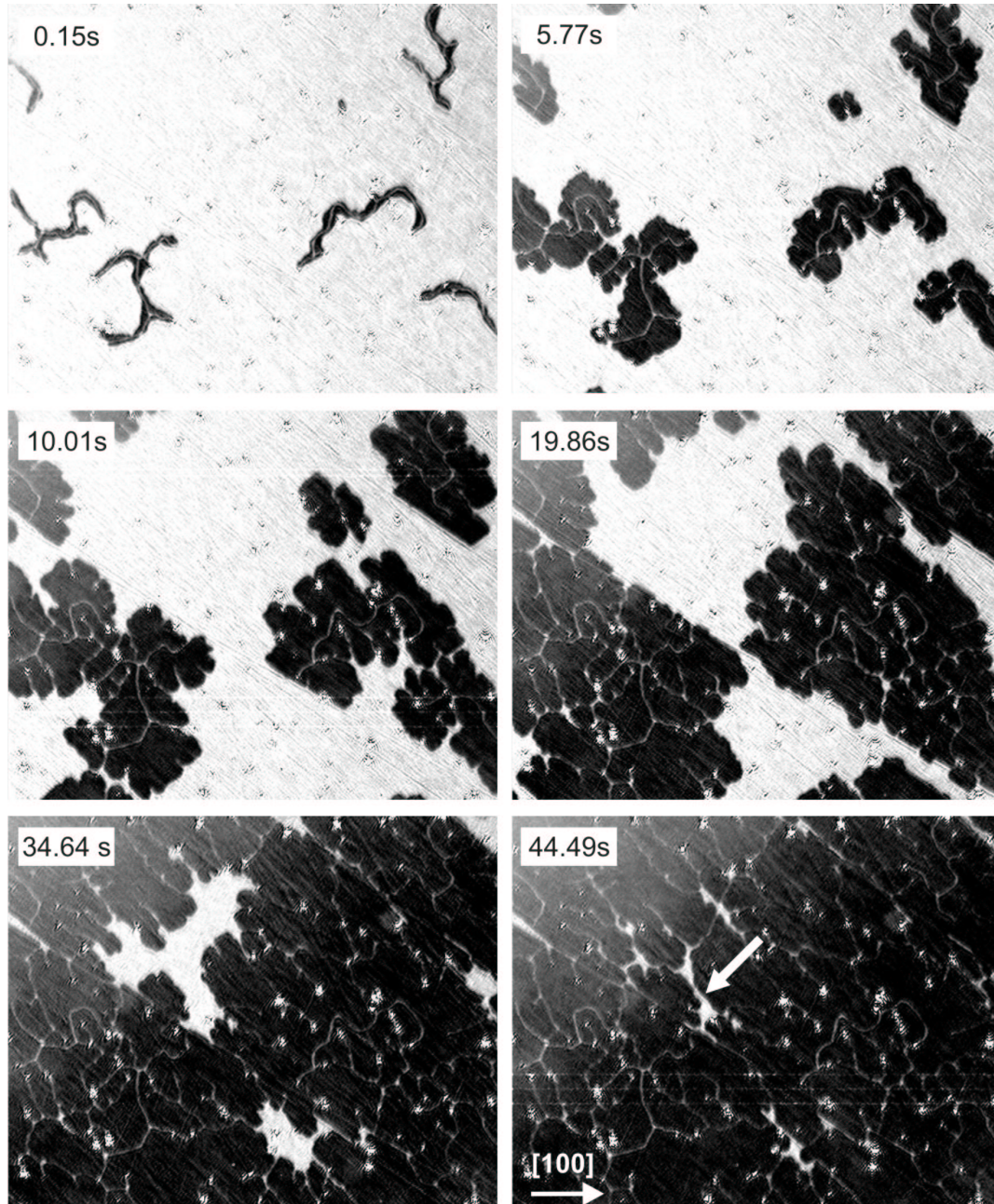


Figure 6.6: Time evolution of magnetic domains imaged at 143 K in the process of magnetization reversal on a 3 ML Fe/Cu(100) film. After the film was pre-magnetized in a field $H_{pre} = 34.2$ Oe, the external field was reversed. The images were recorded in a magnetic field smaller than H_c . The time elapsed after applying the field is noted in the images. The image size is $400 \mu\text{m} \times 320 \mu\text{m}$.

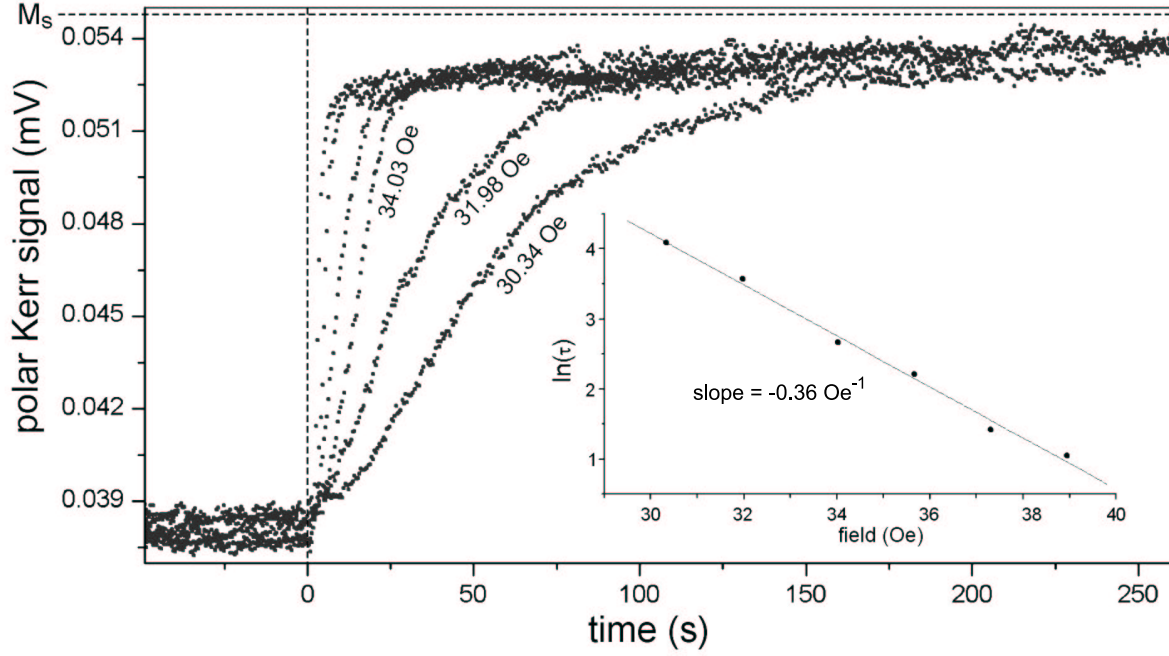


Figure 6.7: Time dependent magnetization reversal as function of time for various external magnetic fields H_{rev} taken at 120 K. Prior to magnetization reversal, the film was magnetized with $H_{pre} = -49.2$ Oe. The linear dependence of $\ln(\tau)$ on the field H is shown in the inset.

The time-dependent behavior of the magnetization M_t of a 3 ML film was additionally analyzed with MOKE at 120 K. The time dependence of the magnetization in different external fields between 30.34 Oe and 38.95 Oe are shown in Fig. 6.7. With increasing field the magnetization speed increases rapidly and the total magnetization converges in a value just below the saturation magnetization. In a simple model the magnetization caused by domain wall displacement¹ grows exponentially at the beginning:

$$M(t) + M_s = 2M_s \cdot \exp\left(-\frac{t}{\tau}\right), \quad M(t=0) = -M_s \quad (6.2)$$

where the temperature dependence of the relaxation time τ follows an Arrhenius law:

$$\tau = \tau_0 \cdot \exp\left(\frac{E_A}{k_B T}\right). \quad (6.3)$$

Here E_A is the average activation energy for one Barkhausen jump. The activation energy is determined by the external field and depends linearly on it. During one Barkhausen jump the magnetization is changed by the Barkhausen volume V_B and the activation energy decreases by $M_S V_B H$. E_A can be written as:

$$E_A = M_s V_B (H_A - H) \quad (6.4)$$

¹An analogous model which considers nucleation differs in the activation energy [182]
 $E_A = M_s V_B (H_A - H)^2 / (2H_A)$

where H_A is related to a propagation field without thermal activation at $T = 0$ (“intrinsic” coercive field) [183]. This approach contains some simplifications. First, the formula takes only a single activation energy into account. An accurate description of the relaxation process should take into account a distribution of activation energies. Good results have been achieved by using the Lorentz distribution [184] on Au/Co/Au films. Second, the shape of domain walls is neglected. A more complex model of [185] includes the wall shape and both domain processes, nucleation and domain-wall propagation.

Each time dependence in Fig. 6.7 was fitted by Eq.(6.2), and the characteristic time constant τ was obtained for every field. The time constant τ as a function of the field is shown in the inset of Fig. 6.7. This plot clearly shows the exponential dependence between relaxation time and the external field as it is expected for thermally activated domain wall motion. The slope of the straight fit line is $-\frac{M_s V_B}{k_B T}$. With M_s and T given, the characteristic volume V_B can be calculated from the slope. From V_B we calculate the Barkhausen length $l_B = \sqrt{(V_B/d)}$ where d is the film thickness. For the 3 ML Fe film at 120 K we obtain $l_B = 80$ nm. As determining factors for l_B the film and the substrate morphology have to be taken into account.

By comparing the value of l_B with the island size obtained in the film as shown in Fig. 6.4a it becomes clear that the island size itself does not determine the Barkhausen volume. The islands found for LT grown films are about 5 nm in diameter and thus more than an order of magnitude smaller than l_B . Other authors find $l_B \approx 220$ nm for LT grown Fe films [186] and conclude also from complementary STM studies on this system, that the Barkhausen volume does not depend on the iron film morphology. Rather, the atomic terrace widths (200–300 nm) of the Cu substrate was proposed to be the determining factor of the Barkhausen volume. The average size of a terrace on the Cu(100) surface after sputtering and annealing in our measurements was found to be 20–50 nm. This is of the same order of l_B , further supporting the assumption of a correlation between Cu(100) terraces and the Barkhausen length.

To rule out to what extent the film structure itself influences the Barkhausen volume, temperature induced changes of the magnetic viscosity have been studied. The temperature dependence of the Barkhausen length was investigated on 3 ML Fe films grown at 120 K. The l_B was determined from the $\ln(\tau)$ versus H -plot taken at various temperatures by using Eq.(6.2)–(6.4). The change of the Barkhausen length with temperature is shown in Fig. 6.8. The data points (\square) are obtained from Kerr image sequences, while the data points (\bullet) are measured with MOKE, on separate films. The data of both techniques are in good agreement and show a clear increase of l_B with temperature by a factor of three. The dashed line is a guide to the eye. Cooling the film back to 127 K

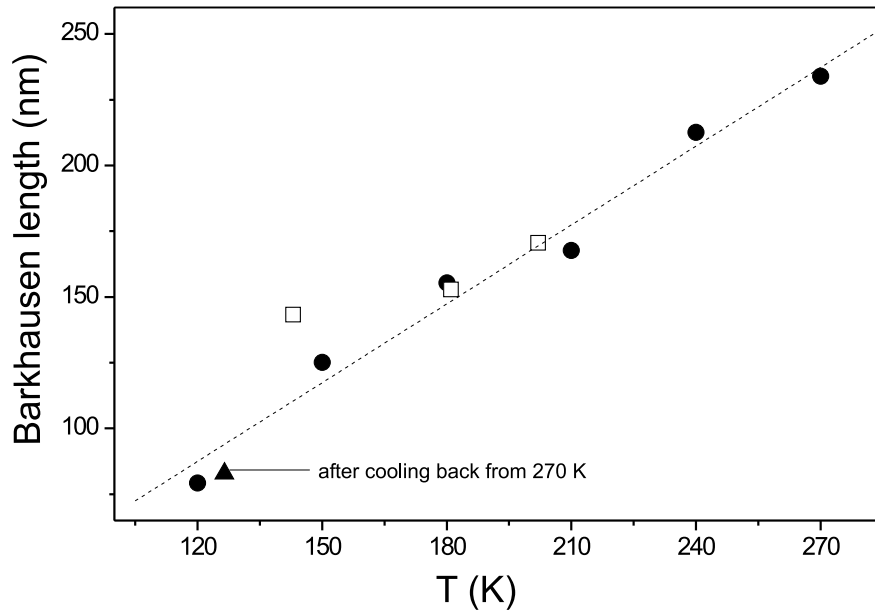


Figure 6.8: Barkhausen length derived by different ways as a function of temperature. The films were grown at 120 K and before taking the data. Data obtained with Kerr microscope (\square) and MOKE (\bullet). The dashed line is a guide to the eye.

decreases the Barkhausen length again to the original value of 83 nm, as can be seen by the data point (\blacktriangle) in Fig. 6.8. The temperature induced increase of the l_B is thus found fully reversible.

An increase of l_B with temperature was also found by [187] in Au capped Co/Au films. Renard et al. argue that an increase of l_B with the temperature could be expected because the probability to make a jump through several small volumes increases with temperature.

Indeed, as was shown in the previous section, temperature treatment leads to an irreversible smoothing of the film. Our STM data (Fig. 6.4) reveal significant structural changes in the film and the formation of three-dimensional islands during annealing. This smoothing suggest a decrease of the energy barriers in the film and thus an increase of l_B . If the film morphology determines the Barkhausen volume, thermally activated irreversible structural changes should cause irreversible changes in l_B . This is clearly not observed in the experiments.

This observation supports the idea of multiple jumps over several terrace widths as the determining length scale of the Barkhausen jumps. These jumps thus control the characteristics of the magnetization reversal process.

Summary

The dependence of the magnetic properties of LT grown Fe films on Cu(100) on the annealing temperature has been investigated. In the first part thermally activated shifts of the spin reorientation transition during annealing have been studied. In the second part the magnetization reversal process has been studied as a function of temperature and of the applied field.

It has been shown that the critical thickness at which the spin reorientation transition occurs changes reversibly and irreversibly with the annealing temperature. The surface anisotropy has been separated into a reversible contribution, attributed to a temperature dependence of the anisotropy constant, and an irreversible contribution due to thermally activated changes in the film structure. Decreasing roughness was made responsible for the increase the t_{crit} below $T_a = 220$ K. Microscopic changes in the film structure not visible in our STM data are suspected to decrease t_{crit} during further annealing above 220 K.

Further information about microscopic changes in the film and its consequences for the Barkhausen volume were expected from magnetic viscosity measurements. The Barkhausen volume was investigated as a function of film temperature and found to increase almost linearly and reversibly with temperature, from 80 nm at 120 K up to 235 nm at 270 K. This increase is attributed to the increased probability to make jumps through several small volumes at once at elevated temperatures.

Some insight has been gained into the magnetization reversal process in LT grown Fe films on Cu(100). It has been shown that a twice as large field is necessary to create domains within the Fe films than required to move domain walls. On the other hand, even after magnetization of the films with external fields slightly larger than the coercivity, domains of opposite magnetization still prevail within the film. This is due to the fact that higher fields are required to remove domain walls in order to form a single domain state.

Conclusions and outlook

In this thesis the reorientation transition of the magnetization at the critical thickness in low temperature grown Fe films on Cu(100) substrates has been investigated. Adsorbate and thermally induced changes of the easy axis of magnetization have been studied on Fe wedges and films of constant thickness by Kerr microscopy and magneto-optical Kerr effect measurements (MOKE). The results point out the importance of the film-vacuum interface for the magnetic anisotropy of the films.

The experiments have been carried out in a newly developed UHV system combining Kerr microscopy, magnetic force microscopy (MFM) and MOKE, as well as scanning tunneling microscopy (STM), for magnetic and structural investigations, respectively. Experiments could be performed at variable temperatures, from 80 K to 500 K. The novel combination of two magnetic imaging techniques, Kerr microscopy and MFM, extends the lateral imaging range from submicrometer up to millimeter. Both techniques deliver complementary information and allow to trace local modifications of the domain structures by the stray field of the MFM tip. The Besocke type scanning microscope head was equipped with a newly designed tip exchange mechanism which allowed the operation of the microscope as a STM, MFM or AFM.

Changes of the magnetization direction caused by the adsorbates oxygen, carbon monoxide and nitric oxide have been studied by Kerr microscopy on wedge shaped Fe films. For the first time, adsorbate induced reorientation transitions in Fe films on Cu(100) could be imaged in-situ. A strong dependence of the magnetic anisotropy of the film on oxygen, NO and CO coverage was found. The observed shift of the spin reorientation transition was found to depend on the adsorbate itself and on the adsorption geometry. It is attributed to a modification of the electronic structure on the film surface by the adsorbates. The data therefore underline the dominant role of the film-vacuum interface for the magnetic properties of the film. Thus, the usual picture of a balance between the surface and volume anisotropy as the determining factor for the orientation of the easy axis of magnetization is supported. Within a phenomenological anisotropy model the observed changes in the critical thickness can be explained by a modified surface

anisotropy constant K_{f-vac} . A value for the CO covered Fe film of $K_{f-vac} = 0.63 \text{ mJ/m}^2$ was determined from the Fe thickness selective reorientation upon CO adsorption.

Thermally induced changes of the reorientation transition are found to be partly reversible and partly irreversible. The reversible contribution is attributed to a temperature dependence of the anisotropy constants and is found to increase linearly with temperature in the range below 300 K. Irreversible contributions are most likely due to thermally activated structural changes in the film. The increase of the critical thickness up to an annealing temperature of 220 K can be attributed to a surface smoothing found by variable temperature STM.

The magnetic after-effect of Fe/Cu(100) was measured with MOKE and Kerr microscopy by recording time dependent magnetization curves upon application of a constant external magnetic field smaller than the coercive field. From these experiments the Barkhausen length could be determined as a function of the temperature. It was found to increase linearly with temperature, from 80 nm at 120 K up to 234 nm at 270 K. These values are by far larger than the Fe island size at the same temperature. The susceptibility of the spin reorientation transition in LT grown Fe/Cu(100) to adsorbate coverage and thermal treatment therefore underlines the delicate balance between electronic and structural properties on one hand, and magnetic properties on the other hand.

In the future, the influence of the nature of the electron transfer between adsorbate and substrate will be studied in more detail by using alkali metal adsorbates which are known to donate electrons into the film. For a better understanding of the adsorbate induced changes on the film structure additional surface analysis techniques, such as LEED or x-ray diffraction (XRD), are needed. The combination of Kerr microscopy with STM, MOKE and MFM for magnetic and structural characterization, as demonstrated in this work, is a powerful technique to study magnetic domains, the structure and the magnetic reversal process of ultrathin films. The high sensitivity and stability of the Kerr microscope can be used to observe changes in the magnetization during the experiment without background subtraction at much higher speeds. The combination of Kerr microscope and MFM, as shown in this work, could be improved by placing the MFM tip in the field of view of the Kerr microscope to guide the tip to the region of interest on the film. The limited resolution of the optical microscope was successfully extended by the MFM to resolve domains structures in the nanometer range. However, also the spatial resolution of MFM remains restricted to some 10 nm [188]. Further improvements will be achieved by using advanced tip technologies, e.g. via focused ion beam milling [189] or electron beam induced deposition (EBID). The ultimate resolu-

tion of the microscopic technique can be achieved by a spin polarized scanning tunneling microscope (SP-STM) [190, 191]. It gives the unique ability to observe directly the interplay between atomic structure and magnetism in the subnanometer scale [192]. The extension of our existing setup by such a SP-STM expands the imaging range and the versatility considerably.

Bibliography

- [1] B. Heinrich, K. Urquhart, A. Arrott, J. Cochran, K. Myrtle, and S. Purcell, Phys. Rev. Lett. **59**, 1756 (1987).
- [2] N. Koon, B. Jonker, F. Volkening, J. Krebs, and G. Prinz, Phys. Rev. Lett. **59**, 2463 (1987).
- [3] J. Elmers, J. Magn. Magn. Mater. **185**, 274 (1998).
- [4] A. Freeman and C. Fu, J. Appl. Phys. **61**, 3356 (1987).
- [5] Y. Li, K. Baberschke, and M. Farle, J. Appl. Phys. **69**, 4992 (1991).
- [6] S. Sun and R. O'Handley, Phys. Rev. Lett. **66**, 2798 (1991).
- [7] A. Enders, D. Sander, and J. Kirschner, J. Appl. Phys. **85**, 5279 (1999).
- [8] L. Néel, J. Phys. Radium **15**, 376 (1954).
- [9] E. Fullerton, D. Kelly, J. Guimpel, I. Schuller, and Y. Bruynseraede, Phys. Rev. Lett. **68**, 859 (1992).
- [10] P. Levy, S. Zhang, and A. Fert, Phys. Rev. Lett. **65**, 1643 (1990).
- [11] P. Bruno, J. Phys. F: Met. Phys. **18**, 1291 (1988).
- [12] T. Monchesky, B. Heinrich, R. Urban, K. Myrtle, M. Klaua, and J. Kirscher, Phys. Rev. B **60**, 1999 (10242).
- [13] T. Monchesky, R. Urban, B. Heinrich, M. Klaua, and J. Kirschner, J. Appl. Phys. **87**, 5167 (2000).
- [14] C. Stamm, F. Marty, A. Vaterlaus, V. Weich, S. Egger, U. Maier, U. Ramsperger, H. Fuhrmann, and D. Pescia, Science **282**, 449 (1998).
- [15] W. Lutzke, Ph.D. thesis, Martin-Luther-Univ. Halle-Wittenberg, 1999.
- [16] P. Gambardella, A. Dallmeyer, K. Maiti, M. Malagoli, W. Eberhardt, K. Kern, and C. Carbone, Nature **416**, 301 (2002).

- [17] C. Liu, E. Moog, and S. Bader, *Phys. Rev. Lett.* **60**, 2422 (1988).
- [18] M. Freeman and B. Choi, *Science* **294**, 1484 (2001).
- [19] H. Oepen and J. Kirschner, *Scan. Microsc.* **5**, 1 (1991).
- [20] M. Scheinfein, J. Unguris, M. Kelley, D. Pierce, and R. Celotta, *Rev. Sci. Instr.* **61**, 2501 (1990).
- [21] F. Schmidt and A. Hubert, *J. Magn. Magn. Mat.* **61**, 307 (1986).
- [22] Y. Martin and H. K. Wickramasinghe, *Appl. Phys. Lett.* **50**, 1455 (1987).
- [23] J. Sáenz, N. Garcia, P. Grütter, and E. Meyer, *J. Appl. Phys.* **62**, 4293 (1987).
- [24] M. Schneider, S. Müller-Pfeiffer, and W. Zinn, *J. Appl. Phys.* **79**, 8578 (1996).
- [25] M. Dreyer, M. Kleiber, A. Wadas, and R. Wiesendanger, *Phys. Rev. B* **59**, 4273 (1999).
- [26] J. Giergiel and J. Kirschner, *Rev. Sci. Instr.* **67**, 2937 (1996).
- [27] A. Vaterlaus, U. Maier, U. Ramsperger, A. Haensch, and D. Pescia, *Rev. Sci. Instr.* **68**, 2800 (1997).
- [28] K. Besocke, *Surf. Sci.* **181**, 145 (1987).
- [29] D. Pescia, M. Stampanoni, G. Bona, A. Vaterlaus, R. Willis, and F. Meier, *Phys. Rev. Lett.* **58**, 2126 (1987).
- [30] M. Stampanoni, A. Vaterlaus, M. Aeschlimann, F. Meier, and D. Pescia, *J. Appl. Phys.* **64**, 5321 (1988).
- [31] S. Müller, P. Bayer, C. Reischl, K. Heinz, B. Feldmann, H. Zillgen, and M. Wuttig, *Phys. Rev. Lett.* **74**, 765 (1995).
- [32] B. Újfalussy, L. Szunyogh, and P. Weinberger, *Phys. Rev. B* **54**, 9883 (1996).
- [33] R. Vollmer, T. Gutjahr-Löser, J. Kirschner, S. van Dijken, and B. Poelsema, *Phys. Rev. B* **60**, 6277 (1999).
- [34] J. Shen, A. Swan, and J. Wendelken, *App. Phys. Lett.* **75**, 2987 (1999).
- [35] O. Pietzsch, A. Kubetzka, M. Bode, and R. Wiesendanger, *Science* **292**, 2053 (2001).
- [36] H. Hug, B. Stiefel, P. van Schendel, A. Moser, and S. Martin, *Rev. Sci. Instr.* **70**, 3625 (1999).

- [37] J. Lösch, U. Memmert, and U. Hartmann, *J. Magn. Magn. Mater.* **226-230**, 1597 (2001).
- [38] E. Mentz, A. Bauer, T. Gunther, and G. Kaindl, *Phys. Rev. B* **60**, 7379 (1999).
- [39] J. Thomassen, B. Feldmann, and M. Wuttig, *Surf. Sci.* **264**, 406 (1992).
- [40] J. Giergiel, J. Kirschner, J. Landgraf, J. Shen, and J. Woltersdorf, *Surf. Sci.* **310**, 1 (1994).
- [41] J. Frohn, J. F. Wolf, K. Besocke, and M. Teske, *Rev. Sci. Instr.* **60**, 1200 (1989).
- [42] Q. Dai, R. Vollmer, R. Carpick, D. Ogletree, and M. Salmeron, *Rev. Sci. Instr.* **66**, 5266 (1995).
- [43] F. Giessibl, C. Gerber, and J. Binning, *J. Vac. Sci. Tech.* **9**, 984 (1991).
- [44] A. Volodin and M. Marchevsky, *Ultramicroscopy* **42**, 757 (1992).
- [45] T. Albrecht, P. Grütter, D. Rugar, and D. Smith, *Ultramicroscopy* **42-44**, 1638 (1992).
- [46] H. Hug, A. Moser, T. Jung, O. Fritz, A. Wadas, I. Parashikov, and H.-J. Güntherodt, *Rev. Sci. Instr.* **64**, 2920 (1993).
- [47] K. Moloni, B. Moskowitz, and E. Dahlberg, *Geophysical Research Letters* **23**, 2851 (1996).
- [48] R. Euler and U. Memmert, U. Hartmann, *Rev. Sci. Instr.* **68**, 1776 (1997).
- [49] D. Pelekhov, J. B. Becker, and G. N. Nunes, *Rev. Sci. Instr.* **72**, 993 (1998).
- [50] W. Allers, A. Schwarz, U. Schwarz, and R. Wiesendanger, *Rev. Sci. Instr.* **69**, 221 (1997).
- [51] A. Volodin, K. Temst, v. C. Haesendonck, and Y. Bruynseraede, *Rev. Sci. Instr.* **71**, 4468 (2000).
- [52] D. Peterka, G. Haas, A. Enders, and K. Kern, to be published at *Rev. Sci. Instr.* (2002).
- [53] M. Tortonese, Ph.D. thesis, Stanford University, 1993.
- [54] H. Hamaker, *Physica* **4**, 1058 (1937).
- [55] J. Sanz and N. Garcia, *J. Appl. Phys.* **62**, 4293 (1987).
- [56] U. Hartmann, *Physical Letters* **137**, 475 (1989).

- [57] U. Hartmann, Phys.Rev. B **40**, 7421 (1989).
- [58] U. Hartmann, J. Vac. Sci. Technol. A **8**, 411 (1990).
- [59] A. Wadas, P. Grütter, and H. J. Güntherodt, J. Appl. Phys. **67**, 3462 (1990).
- [60] D. Rugar, H. Mamin, R. Güthner, J. E. Lambert, I. McFayen, and T. Yogi, J. Appl. Phys. **68**, 1169 (1990).
- [61] Y. Martin, C. Williams, and H. K. Wickramasinghe, J. Appl. Phys. **61**, 4723 (1987).
- [62] P. Grütter, H. Mamin, and D. Rugar, *in: Scanning Tunneling Microscopy, Vol. II, edit by Güntherodt, H. J. and Wiesendanger, R.* (Springer-Verlag, Berlin, 1992).
- [63] P. Horowitz and W. Hill, *The Art of Electronics* (Cambridge University Press, Cambridge, 1998).
- [64] H. Mamin, D. Rugar, J. E. Stern, R. E. Fontana, and J. P. Kasiraj, Appl. Phys. Lett. **55**, 318 (1989).
- [65] M. Faraday, Phil. Trans. Roy. Soc. 1 (1846).
- [66] J. Kerr, Rep. Brit. Ass. **85**, (1876).
- [67] J. Kerr, Phil. Mag. **3**, 321 (1877).
- [68] W. Voigt, Götting. Nachr. **355**, (1898).
- [69] W. Voigt, Wied. Ann. **67**, 359 (1899).
- [70] A. Cotton and H. Mouton, Compt. Rend. Acad. Sci.(Paris) **145**, 229 (1907).
- [71] C. Gerthsen, H. O. Kneser, and H. Vogel, *Physik, edit by Vogel H.* (Springer-Verlag, Berlin, 1989).
- [72] J. Kranz and W. Drechsel, Zeits. Phys. **150**, 632 (1958).
- [73] J. Kranz and A. Hubert, Zeits. Angew. Phys. **15**, 220 (1963).
- [74] A. Bauer, Far-Field and Near-Field Magneto-Optical Microscopy of Ultrathin Films, Habilitation, Freie Universität Berlin, 2000.
- [75] A. Hubert and R. Schäfer, *Magnetic Domains* (Springer-Verlag, Berlin, 2000).
- [76] B. E. Argyle, B. Petek, and J. Herman, J. Appl. Phys. **61**, 4303 (1987).
- [77] B. E. Argyl and J. McCord, J. Appl. Phys. **87**, 6487 (2000).
- [78] E. Zueco, Ph.D. thesis, Technische Universität Dresden, 1999.

- [79] S. Foss, R. Proksch, E. D. Dahlberg, B. Moskowitz, and B. Walsh, *Appl. Phys. Lett.* **69**, 3426 (1996).
- [80] C. Kittel, *Einführung in die Festkörperphysik* (R. Oldenbourg-Verlag, München, 1996).
- [81] E. Kneller, *Ferromagnetismus* (Springer-Verlag, Berlin, 1962).
- [82] H.-J. Elmers, *Magnetismus dünner Filme, in: Magnetische Schichtsysteme, Vorlesungsmanuskripte* (Forschungszentrum Jülich, Jülich, 1999).
- [83] J. Osborn, *Phys. Rev.* **67**, 351 (1945).
- [84] A. Kirilyuk, J. Giergiel, J. Shen, M. Straub, and J. Kirschner, *Phys. Rev. B* **54**, 1050 (1996).
- [85] D. Sander, A. Enders, C. Schmidhals, J. Kirschner, H. Johnston, C. Arnold, and D. Venus, *J. Appl. Phys.* **81**, 4702 (1997).
- [86] B. Jonker, K. Walker, E. Kisker, G. Prinz, and C. Carbone, *Phys. Rev. Lett.* **57**, 142 (1986).
- [87] M. Weinelt, S. Schwarz, H. Baier, S. Müller, L. Hammer, K. Heinz, and T. Fauster, *Phys. Rev. B* **63**, 205413 (2001).
- [88] J. Shen, H. Jenniches, C. Mohan, M. Barthel, J. Klaua, P. Ohresser, and J. Kirschner, *Europhys. Lett.* **43**, 349 (1998).
- [89] K. Man, L. Ling, Y. P. Silena, H. Poppa, M. S. Altman, and Z. Qiu, *Phys. Rev. B* **65**, 024409 (2001).
- [90] K. Man, M. Altman, and H. Poppa, *Surf. Sci.* **480**, 163 (2001).
- [91] M. Lin, J. Shen, J. Giergiel, W. Kuch, M. Jenniches, H. Klaua, C. Schneider, and J. Kirschner, *Thin Solid Films* **275**, 99 (1996).
- [92] J. Thomassen, B. Feldmann, and M. Wuttig, *Surf. Sci.* **264**, 406 (1991).
- [93] M. Wuttig and J. Thomassen, *Surf. Sci.* **282**, 237 (1993).
- [94] P. Schmailzl, K. Schmidt, P. Bayer, R. Döll, and K. Heinz, *Surf. Sci.* **312**, 73 (1994).
- [95] D. Schmitz, C. Charton, A. Scholl, C. Carbone, and W. Eberhardt, *Phys. Rev. B* **59**, 4327 (1999).
- [96] D. Li, M. Freitag, J. Pearson, Z. Qiu, and S. Bader, *Phys. Rev. Lett.* **72**, 3112 (1994).

- [97] D. Steigerwald, I. Jacob, and W. Egelhoff, Surf. Sci. **202**, 472 (1988).
- [98] T. Detzel, N. Memmel, and T. Fauster, Surf. Sci. **293**, 227 (1993).
- [99] S. Müller, P. Bayer, A. Kinne, C. Reischl, R. Metzler, and K. Heinz, Surf. Sci. **331-333**, 723 (1995).
- [100] P. Bayer, S. Müller, P. Schmailzl, and K. Heinz, Phys. Rev. B **48**, 17611 (1993).
- [101] M. Wuttig, B. Feldmann, F. Thomassen, J. May, H. Zillgen, A. Brodde, H. Hanemann, and H. Neddermeyer, Surf. Sci. **291**, 14 (1993).
- [102] H. Zillgen, B. Feldmann, and M. Wuttig, Surf. Sci. **321**, 32 (1994).
- [103] A. Biedermann, M. Schmid, and P. Varga, Phys. Rev. Lett. **86**, 464 (2000).
- [104] R. Vollmer, S. van Dijken, M. Schleeberger, and J. Kirschner, Phys. Rev. B **61**, 1303 (2000).
- [105] J. Thomassen, F. May, B. Feldmann, M. Wuttig, and H. Ibach, Phys. Rev. Lett. **69**, 3831 (1992).
- [106] R. Camley, J. Appl. Physics **89**, 7142 (2001).
- [107] D. Li, M. Freitag, J. Pearson, Z. Qiu, and S. Bader, J. Appl. Phys. **76**, 6426 (1994).
- [108] D. Quian, X. Jin, J. Barthel, M. Klaua, and J. Kirschner, Phys. Rev. Lett. **87**, 227204 (2001).
- [109] V. L. Morruzi, P. M. Marcus, K. Schwarz, and P. Mohn, Phys. Rev. B **34**, 1784 (1986).
- [110] J. Giergiel, J. Shen, J. Woltersdorf, A. Kirilyuk, and J. Kirschner, Phys. Rev. B **52**, 8528 (1995).
- [111] E. Mentz, D. Weiss, J. E. Ortega, A. Bauer, and G. Kaindl, J. Appl. Phys. **82**, 482 (1997).
- [112] H. Albrecht, M. Fritzsche and U. Gradmann, Surf. Sci. **294**, 1 (1993).
- [113] A. Berger, B. Feldmann, H. Zillgen, and M. Wuttig, J. Magn. Magn. Mater. **183**, 35 (1998).
- [114] M. Kief and W. Egelhoff, J. Appl. Phys. **73**, 6195 (1993).
- [115] D. Pappas, C. Brundle, and H. Hopster, Phys. Rev. B **45**, 8169 (1992).
- [116] R. Allenspach, J. Magn. Mag. Mat. **129**, 160 (1994).

- [117] S. Bader and J. Erskine, "*Magneto-Optical Effects in Ultrathin Magnetic Structures*", in *Ultrathin Magnetic Structures II*, edited by B. Heinrich and J.A.C. Bland (Springer-Verlag, Berlin, 1994).
- [118] D. Pappas, K.-P. Kämper, and H. Hopster, Phys. Rev. Lett. **64**, 3179 (1990).
- [119] E. Mentz, Ph.D. thesis, Freie Universität Berlin, 1997.
- [120] D. Pappas, J. Vac. Sci. Technol. B **14**, 3203 (1996).
- [121] Y. Yafet and E. Gyorgy, Phys. Rev. B **38**, 9145 (38).
- [122] H. Oepen, M. Speckmann, Y. Millev, and J. Kirschner, Phys. Rev. B **55**, 2752 (1997).
- [123] M. Speckmann, H. Oepen, and H. Ibach, Phys. Rev. Lett. **75**, 2035 (1995).
- [124] A. Kashuba and V. Pokrovsky, Phys. Rev. B **48**, 10335 (1993).
- [125] A. Kaplan and G. Gehring, J. Magn. Magn. Mater. **128**, 111 (1993).
- [126] A. Vaterlaus, C. Stamm, U. Maier, M. Pini, P. Politi, and D. Pescia, Phys. Rev. Lett. **84**, 2247 (2000).
- [127] J. Bansmann, M. Getzlaff, C. Westphal, and G. Schönhense, J. Mag. Mag. Mater. **117**, 38 (1992).
- [128] D. Pappas, K.-P. Kämper, B. Miller, H. Hopster, D. Fowler, A. Luntz, C. Brundle, and Z.-X. Shen, J. Appl. Phys. **69**, 5209 (1991).
- [129] S. Pick and H. Dreyssé, Phys. Rev. B **63**, 205427 (2001).
- [130] S. Pick and H. Dreyssé, Solid State Comm. **121**, 123 (2002).
- [131] P. Ferro, R. Moroni, M. Salvetti, M. Canepa, and L. Mattera, Surf. Sci. **407**, 212 (1998).
- [132] R. Moroni, F. Bisio, M. Canepa, and L. Mattera, Appl. Surf. Sci. **175-176**, 797 (2001).
- [133] P. Sewell, D. Mitchell, and M. Cohen, Surf. Sci. **33**, 535 (1973).
- [134] C. Leygraf and S. Ekelund, Surf. Sci. **40**, 609 (1973).
- [135] K. Ueda and R. Shimizu, Surf. Sci. **43**, 77 (1974).
- [136] G. Simmons and D. Dwyer, Surf. Sci. **48**, 373 (1975).
- [137] C. Brundle, T. Chuang, and K. Wandelt, Surf. Sci. **68**, 459 (1977).

- [138] Y. Sakisaka, T. Miyano, and M. Onchi, *Phys. Rev. B* **30**, 6849 (1984).
- [139] B. Sincovic, P. Johnson, N. Brookes, A. Clarke, and N. Smith, *Phys. Rev. Lett.* **65**, 1647 (1990).
- [140] G. Leibbrandt, S. Deckers, M. Wiegel, and F. Habraken, *Surf. Sci.* **244**, 1991 (L101).
- [141] G. Leibbrandt, G. Hoogers, and F. Habraken, *Phys. Rev. Lett.* **68**, 1947 (1992).
- [142] M. Salvetti, P. Ferro, R. Moroni, M. Canepa, and L. Mattera, *Surf. Sci.* **377-379**, 481 (1997).
- [143] F. Jona, K. Legg, H. Shih, D. Jepsen, and P. Marcus, *Phys. Rev. Lett.* **40**, 1466 (1978).
- [144] R. Saiki, G. Herman, M. Yamada, J. Osterwalder, and C. Fadley, *Phys. Rev. Lett.* **63**, 283 (1989).
- [145] M. Nassir, D. Dwyer, and P. Kleban, *Surf. Sci.* **356**, L429 (1996).
- [146] T. Tanabe, T. Shibahara, R. Buckmaster, T. Ishibashi, T. Wadayama, and A. Hatta, *Surf. Sci.* **466**, 1 (2000).
- [147] T. Tanabe, Y. Suzuki, T. Wadayama, and A. Hatta, *Surf. Sci.* **427-428**, 414 (1999).
- [148] J. Radnik, E. Chopovskaya, G. M., and K. Wandelt, *Surf. Sci.* **352-354**, 268 (1996).
- [149] N. Brookes, A. Clarke, and P. Johnson, *Phys. Rev. Lett.* **63**, 2764 (1989).
- [150] G. Blyholder, *J. Phys. Chem.* **68**, 2772 (1964).
- [151] S. van Dijken, R. Vollmer, B. Poelsema, and J. Kirschner, *J. Magn. Magn. Mater.* **210**, 316 (2000).
- [152] H. Elmers, J. Hauschild, and U. Gradmann, *J. Magn. Magn. Mater.* **198-199**, 222 (1999).
- [153] D. Spišak and J. Hafner, *Phys. Rev. B* **64**, 094418 (2001).
- [154] C. Egawa, E. McChash, and R. Willis, *Surf. Sci.* **215**, L271 (1989).
- [155] F. Bozso, G. Ertl, M. Grunze, and M. Weiss, *Appl. Surf. Sci.* **1**, 103 (1977).
- [156] R. Vollmer and J. Kirschner, *Phys. Rev. B* **61**, 4146 (2000).
- [157] G. Mankey, M. Kief, F. Huang, and R. Willis, *J. Vac. Sci. Technol. A* **11**, 2034 (1993).

- [158] S. Wu, G. Mankey, F. Huang, and R. Willis, *J. Appl. Phys.* **76**, 6434 (1994).
- [159] W. O'Brien and B. Tonner, *Phys. Rev. B* **49**, 15370 (1994).
- [160] M. Torija, J. Pierce, and J. Shen, *Phys. Rev. B* **63**, 092404 (2001).
- [161] W. Weber, C. Back, A. Bischof, D. Pescia, and R. Allenspach, *Nature* **374**, 788 (1995).
- [162] W. Weber, C. Back, U. Ramsperger, A. Vaterlaus, and R. Allenspach, *Phys. Rev. Lett.* **52**, R14400 (1995).
- [163] T. Beier, Ph.D. thesis, Universität Köln, 1989.
- [164] K. Kishi and M. Roberts, *Surf. Sci.* **62**, 252 (1977).
- [165] D. Shriver, P. Atkins, and C. Langford, *Anorganische Chemie* (VCH Verlagsgesellschaft, Weinheim, 1992).
- [166] H. Over, *Prog. in Surf. Sci.* **58**, 249 (1998).
- [167] M. Roberts and C. McKee, *Chemistry Of The Metal-Gas Interface* (Oxford University Press, Oxford, 1978).
- [168] K. Haas, M.-H. Tsai, and R. Kasowski, *Phys. Rev. B* **53**, 44 (1996).
- [169] P. Feibelman, *Phys. Rev. B* **B56**, 1997 (2175).
- [170] F. Jona and P. M. Marcus, *Crit. Rev. Surf. Chem.* **4**, 189 (1994).
- [171] S. Müller, P. Bayer, A. Kinne, C. Reischl, r. Metzler, and K. Heinz, *Surf. Sci.* **331-333**, 723 (1995).
- [172] T. Gutjahr-Löser, Ph.D. thesis, Martin-Luther-Univ. Halle-Wittenberg, 1999.
- [173] B. Heinrich, Z. Celinski, J. F. Cochran, A. S. Arrott, and K. Myrtle, *J. Appl. Phys.* **70**, 5769 (1991).
- [174] U. Gradmann, *in: Handbook of Magnetic Materials, edit by Buschow, K.H.J.* (Elsevier, Amsterdam, 1993), Vol. 7.
- [175] Landolt-Börnstein, *Structure Data of Elements and Intermetallic Phases*, new series ed. (Springer-Verlag, Berlin, 1971), Vol. III/6.
- [176] T. Gutjahr-Löser, D. Sander, and J. Kirschner, *J. Appl. Phys.* **87**, 5920 (2000).
- [177] Landolt-Börnstein, *Structure Data of Elements and Intermetallic Phases*, new series ed. (Springer-Verlag, Berlin, 1971), Vol. III/19a, p. 49.

- [178] A. Biedermann, R. Tscheliessnig, M. Schmid, and P. Varga, *Phys. Rev. Lett.* **87**, 086103 (2001).
- [179] A. Biedermann, private communication (unpublished).
- [180] D. Craik and R. Tebble, "*Ferromagnetism and ferromagnetic domains*", in *Selected topics in solid state physics IV*, edited by Wohlfahrt, E.P. (North-Holland Publishing Company, Amsterdam, 1965).
- [181] J. Pommier, P. Meyer, G. Pénissard, and J. Ferré, *Phys. Rev. Lett.* **65**, 2054 (1990).
- [182] S. Chikazumi, *Physics of Magnetism*, edit by Charap, S.H. (John Wiley and Sons, Inc., New York, 1966).
- [183] G. Bayreuther, P. Bruno, G. Lugert, and C. Turtur, *Phys. Rev. B* **40**, 7399 (1989).
- [184] P. Bruno, G. Bayreuther, P. Beauvillain, C. Chappert, G. Luget, D. Renard, J. Renard, and J. Seiden, *J. Appl. Phys.* **68**, 5759 (1990).
- [185] E. Fatuzzo, *Phys. Rev.* **127**, 1999 (1962).
- [186] A. Kirilyuk, J. Giergiel, J. Shen, and J. Kirschner, *J. Magn. Magn. Mater.* **159**, L27 (1996).
- [187] A. Kirilyuk, J. Ferré, and D. Renard, *IEEE Trans. Magn.* **29**, 2518 (1993).
- [188] P. Grütter, E. Meyer, H. Heinzelmann, L. Rodenthaler, , H.-R. Hidber, and H.-J. Güntherodt, *J. Vac. Sci. Technol.* **A 6**, 279 (1988).
- [189] L. Folks, M. Best, P. Rice, B. Terris, and J. N. Weller, D. Chapmann, *Appl. Phys. Lett.* **76**, 909 (2000).
- [190] R. Wiesendanger, I. Shvets, D. Burgler, G. Tarrach, and H.-J. Güntherodt, *Ultra-microscopy* **42-44**, 338 (1992).
- [191] W. Wulfhekel and J. Kirschner, *J. Appl. Phys.* **75**, 1944 (1999).
- [192] M. Pratzer, H. Elmers, M. Bode, O. Pietzsch, A. Kubetzka, and R. Wiesendanger, *Phys. Rev. Lett.* **87**, 127201 (2001).

Abbreviations and common symbols

AF	Antiferromagnetic
AFM	Atomic Force Microscopy
CO	Carbon Monoxide
EBID	Electron Beam Induced Deposition
LEED	Low Energy Electron Diffraction
LT	Low Temperature
MAE	Magnetic Anisotropy Energy
MBE	Molecular Beam Epitaxy
MFM	Magnetic Force Microscopy
MMF	Multimode Fiber
MO	Molecule Orbital
MOKE	Magneto-Optical Kerr Effect
NA	Numerical Aperture
NC-AFM	Non-Contact Atomic Force Microscopy
NO	Nitric Oxide
PSEE	Polarized Secondary Electron Emission
ROT	Reorientation Transition
RT	Room Temperature
SEM	Scanning Electron Microscopy
SEMPA	Scanning Electron Microscopy with Spin Analysis
SPSEES	Spin-Polarized Secondary Electron Emission Spectroscopy
SP-STM	Spin Polarized-Scanning Tunneling Microscopy
STM	Scanning Tunneling Microscopy
TDS	Thermal Desorption Spectroscopy
UHV	Ultra-High Vacuum
UPS	Ultraviolet Photoemission Spectroscopy
XRD	X-Ray Diffraction

a	lattice constant
bcc	body centered cubic
E_F	Fermi energy
eV	electron volt $1eV = 1.602 \cdot 10^{-19}$ J
ε	strain
fcc	face centered cubic
fct	face centered tetragonal
f_{MC}	magneto-crystalline anisotropy energy
f_{ME}	magneto-elastic anisotropy energy
f_{shape}	shape anisotropy energy
f_{surf}	surface anisotropy energy
f_{tot}	total anisotropy energy
H_c	coercive field
H_{sat}	saturation field
H_{rev}	reversal field
H_{pre}	pre-magnetization field
K_S	surface anisotropy constant
l_B	Barkhausen length
L	Langmuir $1L = 1 \cdot 10^{-6}$ torr \cdot s
T_a	annealing temperature
t_{crit}	critical thickness of spin reorientation transition
t	film thickness

Merci

Merci beaucoup à tous ceux qui ont contribué à la réalisation de cette thèse:

au Professeur Klaus Kern, mon directeur de thèse, pour m'avoir donné l'opportunité de réaliser ce travail dans deux laboratoires de haut niveau et pour son soutien pendant ces 4 ans;

à Günter Haas, le meilleur post-doc et guide de haute montagne du monde. Les heures passées ensemble, au labo et en montagne, resteront un de mes meilleurs souvenirs de Lausanne. Grâce à son aide j'ai gravi aussi ce sommet: das Matterhorn! Un jour inoubliable.

à Axel Enders pour son engagement énorme, pour m'avoir poussé dans mon travail, pour les discussions motivantes et pour la relecture du manuscrit. Son optimisme était indestructible;

aux membres du jury: Professeur W. Benoit, Professeur D. Pescia et Professeur B. Hillebrands pour avoir jugé cette thèse;

à mes collègues doctorants, particulièrement: Jens Weckesser, Nikolaus Knorr, Samuel Sarbach, Christian Klinke et Diego Repetto pour une très bonne atmosphère à l'institut et les activités hors de l'institut;

à tous les membres des ateliers de mécanique et d'électronique à Lausanne et Stuttgart pour leur précieuse collaboration;

à Katja Starke pour les milles petits details et le tuyau: "regarde en bas à gauche" et finalement à mes parents, mes soeurs Dorothee et Bettina et mes amis qui ont dit bon courage et qui m'ont accompagné pendant mes études avec intérêt et soutien.

Curriculum vitae

Name:	Dietrich Peterka
Date of Birth:	July 12, 1970
Nationality:	German
1977–1987	Polytechnical school in Quedlinburg
1987–1989	Extended polytechnical school in Quedlinburg
1991–1998	Study of physics at the University of Hannover Diploma thesis at the Institut für Festkörperphysik, Prof. H. Pfnür: “Vibronische und elektronische Struktur von MgO-Schichten – eine hochauflösende EELS Analyse”
1998–2000	Research and teaching assistant in the group of Prof. K. Kern at the Institute of Experimental Physics at the École Polytech- nique Fédérale de Lausanne, Switzerland
2000–2002	Continuation of scientific work at the Max-Planck-Institut für Festkörperforschung in Stuttgart, Germany
2002	PhD thesis: “Adsorbate and thermally induced spin reorien- tation transition in thin Fe films on Cu(100)”

Publications

Defects in epitaxial insulating thin films

C. Tegenkamp, H. Pfnür, W. Ernst, U. Malaske, J. Wollschläger,
D. Peterka, K.M. Schröder, V. Zielasek, and M. Henzler
J. Phys.: Condensed Matter **11**, 9943 (1999).

*Oxygen surplus and oxygen vacancies on the surface of epitaxial
MgO layers grown on Ag (100)*

D. Peterka, C. Tegenkamp, K.-M. Schröder, W. Ernst, and H. Pfnür
Surface Science **431**, 146 (1999).

*Adsorbate and thermally induced spin reorientation transition
in LT grown Fe/Cu (001) studied by in-situ Kerr microscopy*

D. Peterka, A. Enders, G. Haas and K. Kern
Phys. Rev. B, in press (2002).

*A combined Kerr Microscope and Magnetic Force Microscope
for variable temperature UHV investigations*

D. Peterka, A. Enders, G. Haas, and K. Kern
submitted to Rev. Sci. Inst.

